# Lawrence Berkeley National Laboratory
## Recent Work

**Title**
DIFFERENTIAL DISTRIBUTIONS OF NEUTRONS IN INELASTIC N-p INTERACTIONS AT 374, 4l7, AND 454 MeV

**Permalink**
https://escholarship.org/uc/item/14j986mm

**Author**
Kurz, Richard J.

**Publication Date**
1962-11-15

# University of California

# Ernest O. Lawrence Radiation Laboratory

# DIFFERENTIAL DISTRIBUTIONS OF NEUTRONS IN INELASTIC $\pi^-$p INTERACTIONS AT 374, 417, AND 454 MeV

Berkeley, California

## DISCLAIMER

UNIVERSITY OF CALIFORNIA

Lawrence Radiation Laboratory
Berkeley, California

# DIFFERENTIAL DISTRIBUTIONS OF NEUTRONS
## IN INELASTIC π⁻p INTERACTIONS AT 374, 417, AND 454 MeV

Richard J. Kurz

(Ph. D. Thesis)

November 15, 1962

# DIFFERENTIAL DISTRIBUTIONS OF NEUTRONS
# IN INELASTIC $\pi^-$p INTERACTIONS AT 374, 417, AND 454 MeV

## Contents

-iv-

# DIFFERENTIAL DISTRIBUTIONS OF NEUTRONS
## IN INELASTIC π⁻p INTERACTIONS AT 374, 417, AND 454 MeV

Richard J. Kurz

Lawrence Radiation Laboratory
University of California
Berkeley, California

November 15, 1962

## ABSTRACT

The inelastic interactions of negative $\pi$ mesons with protons at 374, 417, and 454 MeV incident $\pi$ kinetic energy were studied by measuring the differential distributions of final-state neutrons. The $\pi$ source was an internal target of the Berkeley 184-inch synchrocyclotron. A magnetic beam-transport system momentum-analyzed and focused the $\pi$ beam at a liquid hydrogen target located in an adjacent shielded experimental area. The time-of-flight distribution of neutral particles was measured at various laboratory-system angles between 10 and 65 deg. Neutral particles were detected by observing the charged products of their interactions in plastic scintillator. The time-of-flight information was determined electronically by time-to-height conversion and pulse-height analysis. The time resolution of the total system was 1.0 nsec. Detected neutral particles accompanied by charged particles were separated by the electronic system from those not accompanied by charged particles.

Analysis presuming the principal inelastic reactions to be $\pi^- p \rightarrow \pi^+ \pi^- n$ and $\pi^- p \rightarrow \pi^0 \pi^0 n$ separated the time-of-flight spectra into gamma rays, neutrons from the reaction $\pi^- p \rightarrow \pi^0 n$, and inelastic neutrons. Calculated values of the neutron-detection efficiency were used in the conversion of the neutron time-of-flight distribution to neutron differential distributions as a function of energy. A description of the neutron efficiency calculation is included. A definite deviation from the behavior expected on the basis of a statistical

distribution or a simple peripheral collision model was observed in the distributions of the inelastic neutrons. The inelastic neutron differential distributions showed a strong preference for neutrons of low c. m. momentum.

By integrating the differential distributions, the total cross sections for the two inelastic reactions listed above were obtained. The cross section for the $\pi^+\pi^-n$ channel was a rapidly rising function of incident $\pi$ energy, whereas the cross section for the $\pi^0\pi^0n$ channel was essentially constant as a function of energy. In addition, the total cross section for the processes $\pi^-p \rightarrow$ neutrals was obtained along with tentative data on the angular distribution of the reaction $\pi^-p \rightarrow \pi^0n$.

The first experiment of the program utilized the uniqueness of the $\pi^+$ in (3) as a signature.[4] This reaction was investigated in the energy region from 260 to 430 MeV. The results of this experiment indicated that the cross section for this reaction increased much more rapidly as a function of energy than the existing theoretical predictions. These predictions were the result of attempts to extend the static model to pion-production processes.[5] This observation coincided with the growing recognition of the importance of the $\pi\pi$ system. Rodberg proposed the $\pi\pi$ interaction as an explanation of the unexpectedly large cross section.[6] His calculation added enough $\pi\pi$ interaction to a static-model description to fit the energy dependence of the cross section. An alternative explanation of the cross section involved the $\pi N$ (3, 3) resonance (so-called isobar) as the mechanism of enhancement.[7]

Further studies of (3) in the 400-MeV region were performed in the second experiment of the program.[8] The objectives were to obtain accurate differential distributions of the $\pi^+$ and to ascertain the importance of the isobar. The results of this experiment reaffirmed the value of the cross section previously obtained, but indicated that the angular distribution of the $\pi^+$ was more isotropic than previously indicated. In addition the energy distribution showed a definite influence of the isobar.

At that time more detailed calculations by Goebel and Schnitzer on the model proposed by Rodberg became available.[9] These results were later revised to correspond to the more accurate data of the second experiment.[10] The various charge states of the two pions in the pion-production reactions correspond to different combinations of $\pi\pi$ isotopic spin eigenstates. The I = 0, 1, and 2 states are available in (3), the I = 1 and 2 in (4), and I = 0 and 2 in (5). Schnitzer used as parameters the $\pi\pi$ interaction strengths in the three isospin states. When these strengths were adjusted to fit the available data for (3) as well as a measurement of the $\pi^+$p inelastic processes,[11] predictions were made for all the pion-production channels. The analysis indicated the dominant interaction to be in the I = 0 state.

To check these predictions the next measurement of the pro-
gram investigated (4) in the same energy region.[12] The experiment
measured the differential distribution of the proton. The cross section
agreed with the predictions by Schnitzer. The results can be inter-
preted as confirming the absence of a strong I = 1 or I = 2 $\pi\pi$ interaction
for $\pi\pi$ system energies between 275 and 417 MeV.

Information from other measurements also supported the same
conclusions. The data of Abashian et al.[13] on pion production in pd
collisions indicate an anomalous low energy $\pi\pi$ system behavior which
was interpreted as the effect of a strong I = 0 $\pi\pi$ interaction. The
data of Kirz et al.[14] on the reaction $\pi^+ + p \rightarrow \pi^+ + \pi^+ + n$ at 357 MeV
in which the $\pi\pi$ system is in a pure I = 2 state indicate no appreciable
interaction in that state.

These developments indicated the desirability of more meas-
urements on the I = 0 $\pi\pi$ system. The most direct method of exam-
ining this system was to measure the differential distributions of the
neutrons in reactions (3) and (5). In addition, the cross section for
(5) could be compared with Schnitzer's predictions.

The measurement of neutrons encountered two difficulties--
detection efficiency and energy determination. The time-of-flight
method was chosen to determine the neutron energy. The available
pion flux, detector efficiency, cross section, and background limited
the flight path that could be used. Current scintillation-counter time
resolutions provided an acceptable energy resolution at this flight
path.

Detector efficiencies of the order of 10% were possible for a
reasonable scintillator size. This efficiency was not accurately known
in the neutron energy range of interest. Therefore, the experiment
was designed to yield as much information as possible independent of
the neutron-detection efficiency. If the neutron differential distributions
in (3) and (5) were similar, the ratio of the cross sections would be
such a quantity. The $\pi\pi$ interaction could also be investigated as a
function of the $\pi\pi$ system total energy, $\omega_{\pi\pi}$, in an efficiency-independent

way. The laboratory-system kinematics of the inelastic neutrons are shown in Fig. 1. Contours of constant $\omega_{\pi\pi}$ (constant neutron c. m. monentum) and constant neutron c. m. angle are also indicated in the figure. Measurement of the neutron differential distribution as a function of angle at a constant neutron lab energy would examine the $\pi\pi$ system as a function of $\omega_{\pi\pi}$ while the detector efficiency was held fixed and the neutron c. m. angle was held approximately constant.

Fig. 1. Laboratory-system neutron kinematics for the processes $\pi^- p \rightarrow \pi\pi n$ (region inside curve A) and $\pi^- p \rightarrow \pi^0 n$ (curve B) at 374 MeV.

MU-28829

## II. EXPERIMENTAL METHOD

### A. Experimental System

This experiment was performed in the meson cave of the 184-inch synchrocyclotron. Figure 2 is a plan view of the cyclotron, showing the shielding and the magnet arrangement. Inside the normal walls of the meson cave a shielded area was used which had 2 feet of wood overhead and 1 ft of wood on the floor. The meson beam entered this area through a 7-in.-diameter circular aperture in the front wall and exited through a 1×1-ft opening in the rear wall, and was stopped in the back wall of the meson cave.

#### 1. Background

The background neutral-particle flux inside this shielded enclosure is given in Table I. These measurements were made with the neutron-detection system described in Sec. II. A. 3. If the cyclotron was operating but the beam was not entering the shielded area the rates were reduced by approximately 25%.

Table I. Neutral background flux.

| Detection threshold (energy of electron producing equivalent light) (MeV) | Counting rate (number per $cm^3$ of scintillator per second) |
|---|---|
| 0.5 | 68 |
| 1.0 | 41 |
| 1.5 | 23 |
| 2.0 | 13 |
| 2.8 | 11 |
| 4.0 | 7.5 |

#### 2. Negative Pion Beam

The beam system was designed for pions of 380-MeV kinetic energy. The negative pions were produced by intercepting the 732-MeV internal proton beam of the cyclotron with a Be target which had a 1/2-in. radial by 2-in. vertical cross section and was 2-in. thick in

-7-



Fig. 2. Plan view of 184-inch cyclotron meson cave experimental
area, showing the experimental arrangement.

the beam direction. The pions were deflected outward by the magnetic field of the cyclotron, and left the vacuum tank through a thin aluminum window.

The primary negative-pion production reaction is $p + n \rightarrow \pi^- + p + p$. The phase-space distribution for this reaction for incident proton energy of 732 MeV is shown in Fig. 3. To produce pions of kinetic energies 375 to 450 MeV it is evidently necessary to rely upon the internal momentum of the neutrons bound inside the Be nuclei of the target; also, one is limited to production at angles close to 0 deg.

     a. <u>Beam design.</u>

There is little flexibility available in the design of the negative pion beam at these energies. Experience on previous experiments in this program has shown that maximum flux of the peak-energy internal proton beam occurs at orbits of radius between 81 and 83 in. The target radius was set at 82 in. and the trajectory of the negative pions up to the element Q1 was determined by the cyclotron magnetic field. This trajectory was calculated by the IBM 709-7090 FORTRAN cyclotron or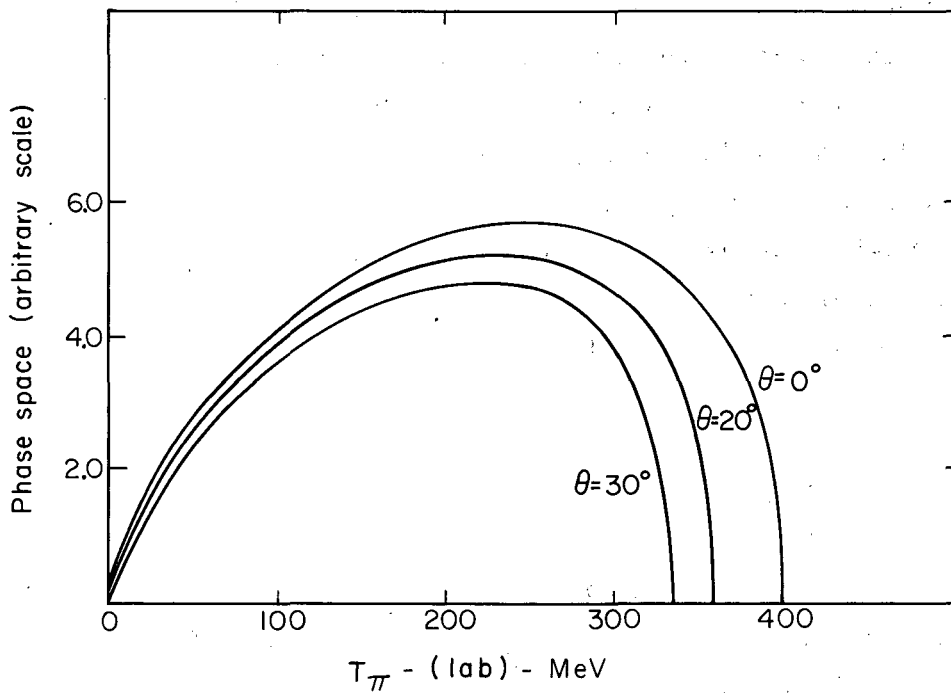bits program of H. Goldberg, J. Good, and M. Pripstein, which uses measured values of the cyclotron magnetic field to integrate the equations of motion of the particle. The azimuthal location of the target was determined by the requirement that this trajectory pass through the center of the meson wheel (see Fig. 2).

Calculations of the beam system were performed with the IBM 709-7090 FORTRAN program OPTIK,[15] in which the beam is described by a vector with five components $(x, x', y, y', \Delta p/p_0)$, where $x$ is the horizontal displacement from the beam line, $x'$ is the horizontal direction with respect to the beam line in radians, $y$ and $y'$ are the corresponding quantities in the vertical direction, and $\Delta p/p_0$ is the fractional deviation of the beam momentum from that for which the system is tuned, $p_0$. In this representation the action of any element of the system (bending magnet, quadrupole magnet, etc.) can be represented by a matrix and the effect of the whole system is represented by the product of the matrices for each successive element.

MU-28392

Fig. 3. Phase space for the reaction $p + n \rightarrow \pi^- + p + p$ at 732 MeV.

It was assumed that the magnetic field of the cyclotron could be simulated by three elements: a field-free region, a bending magnet, and a field-free region. There are six independent parameters in this combination of elements: the length of the first field-free region, the angle of entrance into the bending magnet, the angle of bend, the radius of curvature of the bend, the angle of exit from the bending magnet, and the length of the second field-free region. By use of the cyclotron orbits program the effect of the cyclotron field on selected vectors in the horizontal plane was calculated in order to determine these six parameters. These results were then used to calculate the elements of the matrix describing the vertical plane. The matrix representing the effect of the cyclotron field on 380-MeV negative pions originating at 82-in. radius and in a direction tangent to the internal beam orbit is as follows:

$$\begin{pmatrix} -0.7718 & 34.75 & 0 & 0 & 37.40 \\ -0.3492 & 0.2652 & 0 & 0 & 0.7139 \\ 0 & 0 & 1.767 & 72.87 & 0 \\ 0' & 0 & 0.01731 & 1.280 & 0 \\ 0 & 0 & 0 & 0 & 1 \end{pmatrix}$$

This matrix was used as the initial element in the calculations of the 380-MeV beam system using the program OPTIK.

The maximum field gradient of element Q1 could produce a parallel beam in both the horizontal and vertical planes. This beam must be focused at the final image by the element Q2. There were four factors to be decided in the beam design: (a) the sequence of polarities in elements Q1 and Q2, (b) the relative order of elements Q2 and M, (c) the angle and direction of the bend in M, and (d) the location of the final image. The criteria on which the choices were based were maximum solid angle of acceptance at the source by the system, matching of the momentum dispersion introduced by the cyclotron field by the external bending magnet, and minimum magnification of the source at the final image. Calculations using OPTIK were performed by varying the four factors above, and the optimum system
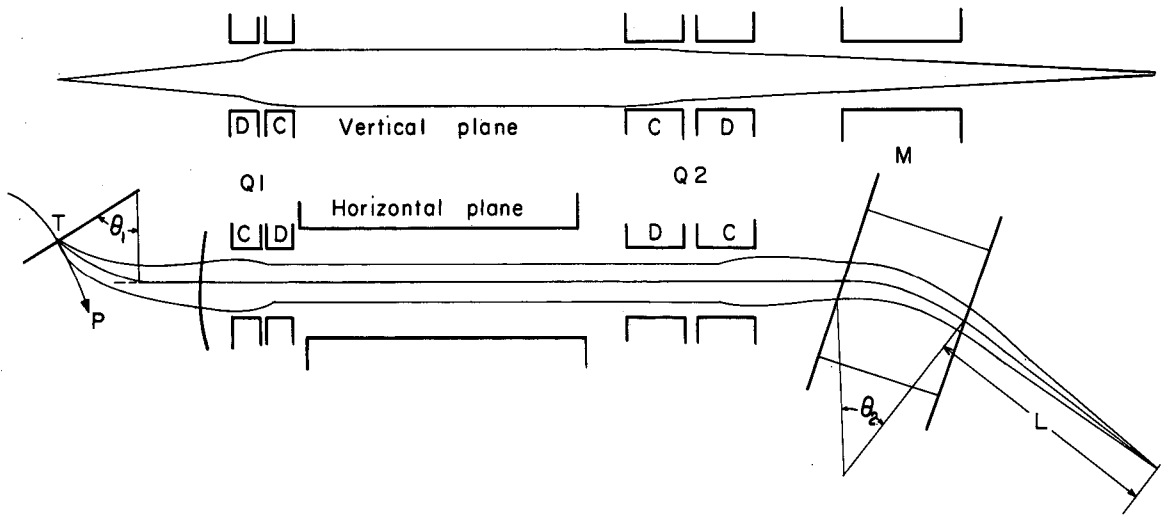
is shown schematically in Fig. 4. The horizontal magnification of the system is -4.83, the vertical magnification is -1.83, the half width at half maximum of the acceptance as a function of momentum is 0.03 $p_0$, and the displacement of the final image for noncentral momenta is -1.39 $(\Delta p/p_0)$ in.

        b.  <u>Measured properties</u>.

The current required to produce the desired angle of bend in the bending magnet M was determined experimentally by the suspended-wire technique. The quadrupole magnet currents were varied about those calculated by OPTIK and set at values that produced the best beam profiles at the final image. The final settings agreed well with those calculated by OPTIK. The beam profiles in both planes could be represented by a Gaussian function. The horizontal variance was 0.63 in. and the vertical variance was 0.40 in. In order to reduce the multiple Coulomb scattering of the pions the beam path was in an atmosphere of helium gas from the entrance of Q1 to the exit of M. In first order the rms projected displacement for this 21-ft path was calculated to be 0.63 in. for air and 0.17 in. for helium.

The average energy and the energy spread of the beam were determined by the integral range method. Transmission was measured as a function of copper absorber thickness. Figure 5 is the integral range curve and a numerical differentiation of the integral range curve. The mean energy was 374 MeV (223 g/cm$^2$ of Cu), and the energy spread was ± 14 MeV after correction for the range straggling of the pions in Cu.[16] In terms of momentum this was $\Delta p/p_0$ = 14/494 = 0.028, in good agreement with the calculations on the beam system. The difference of 6 MeV between the suspended-wire measurements and the range curve measurements was due to energy losses in the beam monitor counters. The calculated energy loss was 4.6 MeV.

The energies of the two higher-energy beams were determined by suspended-wire measurements and adjusted by 6 MeV in accordance with the 374-MeV range measurements. The mean energies were 417 MeV and 454 MeV. The energy spread was presumed to be consistent

Fig. 4.  Beam optics diagram.
C = convergent quadrupole element
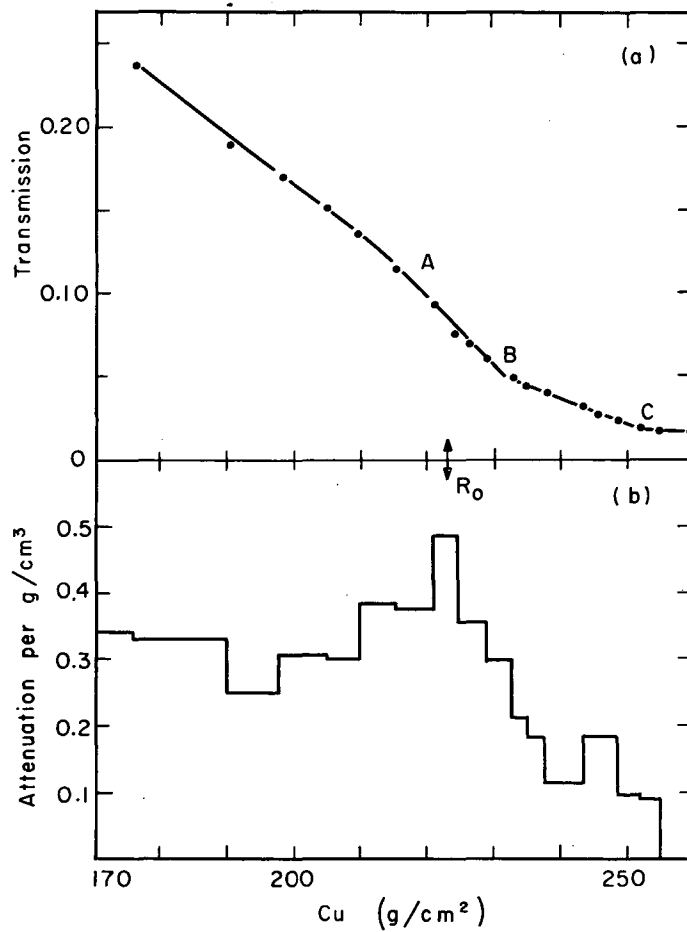D = divergent quadrupole element
T = internal Be target
P = internal proton beam
$\theta_1$ = 59 deg
$\theta_2$ = 38 deg
L = 84.5 in.

MU-28832

Fig. 5. (a) Integral range curve.
(b) Numerical differentiation of integral range curve.

with $\Delta p/p_0 = 0.03$. The currents in Q1 and Q2 were scaled up from the solutions obtained for the 380-MeV system. The internal target position was determined by maximizing the beam intensity at the final image with the magnets set at the proper currents.

The composition of the beam included muons and electrons as well as pions. For absorber thickness greater than 234 g/cm$^2$ (point B, Fig. 5) only muons and electrons are left. The muons occurring from decays of pions before the bending magnet are momentum-analyzed and therefore included in the range curve beyond point B. The pions decaying after the bending magnet give a spectrum of muon momenta. Only a fraction of these are included in the range measurement. The contamination due to decays after the magnet was calculated and combined with the range curve information to give a total muon contamination of 5%. The electron contamination was estimated to have been 0.3% on the basis of previous measurements using a gas Cerenkov counter performed on similar pion beams.[17] The properties of the beams used in this experiment are listed in Table II. The intensities listed are through a 6-in.$^2$ cross-sectional area at the final image, on long-spill cyclotron operation, and do not include the beam located in the initial spike (see Sec. II. A. 4).

Table II. Beam parameters.

| Energy (MeV) | Momentum (MeV/c) | $\Delta T$ (MeV) | Intensity (sec$^{-1}$) |
|---|---|---|---|
| 374 | 494 | $\pm 14$ | $1.7 \times 10^5$ |
| 417 | 539 | $\pm 16$ | $8.0 \times 10^4$ |
| 454 | 577 | $\pm 17$ | $1.3 \times 10^4$ |

3. Liquid Hydrogen Target

The liquid hydrogen target was located at the final focus of the beam system. The vacuum chamber and hydrogen flask are shown in Fig. 6. The flask and vacuum chamber were designed with three objectives in mind: (a) to be able to surround the target as completely as possible by counters, (b) to minimize the amount of material other than liquid hydrogen in the beam, and (c) to minimize the amount of material

To liquid hydrogen
reservoir

Liquid hydrogen

flask

Al

5

3

4

MU-28833

Fig. 6.  Liquid hydrogen target and surrounding scintillation
counters.

that could act as converter for gamma rays and scatterer for neutrons leaving the target. The vacuum chamber consisted of a 6-in.-diameter Al cylinder with 0.040-in. walls and a 0.020-in. spun Al end dome. The front window of the vacuum chamber was 0.030-in. Mylar.

The liquid hydrogen flask was a 3-in.-diameter 8-in.-long horizontal cylinder with walls of 0.015-in. Mylar. The end windows were 0.015-in. Mylar. The flask was supported in the vacuum chamber by styrofoam braces. Because the ends of the hydrogen flask were slightly curved, the mean value of the target length was obtained by averaging the target length weighted by the beam profile over the cross-sectional area of the target. This value was 7.79 in. and was computed by using 0.069 g/cm$^3$ as the difference between the density of liquid hydrogen and the density of hydrogen gas at liquid nitrogen temperature.[18]

4. Electronics

Figure 7 is a schematic diagram of the electronic system. As indicated in the diagram, it may be subdivided into three major sections--(a) the pion beam monitor section, (b) the neutron-detection and time-of-flight analysis section, and (c) the event-routing section. Some of the boxes in the diagram are simplified representations of several circuits which together performed the indicated function. References to special circuits are by LRL Engineering Drawing Number. Descriptions of all other circuits may be found in the LRL Counting Handbook.[19]

a. Beam monitor section

Three counters were located in the beam to monitor the incident pion flux (see Fig. 2). Counter 2 also served as the source of zero-time signals for the time-of-flight analysis. Counter 3 defined the area of the beam accepted by the monitor system. A fourth counter, located after the hydrogen target, rejected the incident pions that were not scattered by an angle greater than 10 deg in the hydrogen. The configuration of counters 3 and 4 with respect to the liquid hydrogen target is shown in Fig. 6.
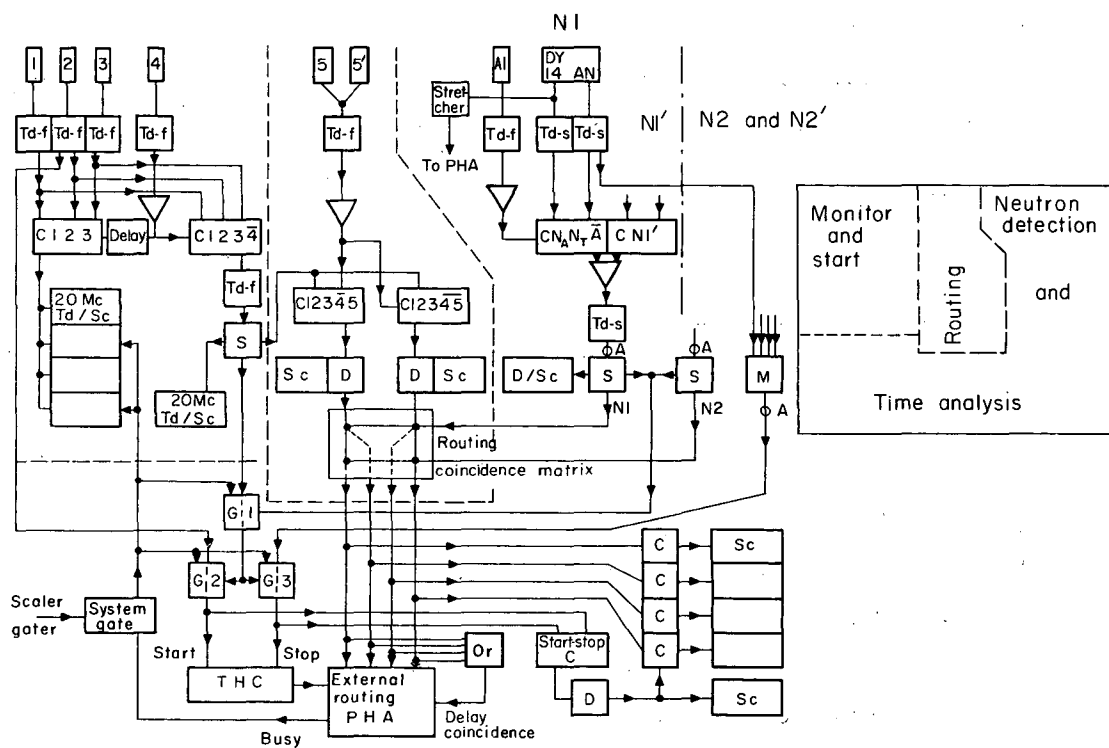
- 17 -



MUB-1491

Fig. 7.  Electronic system.
C = coincidence
D = 10-Mc discriminator
Sc = 5-Mc scaler
Td = tunnel diode discriminator
Td-f = (4X-6381-18-fast)
Td-s = (4X-6381-18-slow)
G = gate
S = splitter
M = mixer

Each of these counters was made of a circular piece of plastic scintillator optically connected by a lucite light pipe to a photomultiplier tube. Their dimensions and phototube types are listed in Table III. The phototube type for the zero-time counter was chosen for its better timing characteristics.[19] The beam-defining counter was thin, so as to reduce the number of non-hydrogen-scattered pions accepted by the system. The zero-time signal was not derived from this counter because the timing resolution would have been deteriorated by the statistical fluctuations in the small number of photoelectrons produced at the photocathode by a beam pion passing through the thin scintillator.

Table III. Counter description.

| Counter | Dimensions | | Phototube |
| --- | --- | --- | --- |
| | thickness (in.) | diameter (in.) | type |
| 1 | 1/4 | 7 | RCA 6810A |
| 2 | 1/4 | 5 | RCA 7264 |
| 3 | 1/32 | 2-3/4 | RCA 6810A |
| 4 | 1/2 | 7 | RCA 6810A |

The monitor system was required to be 100% efficient in scaling two pulses with separations $\geq 50$ nsec. The cyclotron beam possesses a fine structure in time. Beam is produced only in 13-nsec bunches with a frequency of one bunch per 54 nsec (the frequency of the cyclotron accelerating voltage). The monitor counters could not resolve two particles within one bunch, so there was no need to require the associated electronics to be able to resolve particles separated by less than 54 nsec.

At the beam intensities available for this experiment there was a nonzero probability of more than one pion's being in the same bunch. The system would not resolve these particles and the monitor had to be corrected. The auxiliary dee facility of the 184-inch cyclotron was used throughout this experiment. The advantage of the cyclotron auxiliary dee operation was that this probability was limited to 2% at the highest fluxes listed in Table II because the same total flux was

distributed over more time (i. e. more bunches). Just before the
beam reaches full radius, control of the internal beam is transferred
from the main rf accelerating dee to the auxiliary dee (see Fig. 2).
The frequency modulation of this electrode is programmed in such a
way as to spill beam onto the Be target over a period of 6 to 10 msec
instead of the normal maximum duration of 400 $\mu$sec. The duty cycle
of the accelerator is thus potentially improved by a factor of approxi-
mately 20. However, total flux is lost in the transition process and
the average intensity was reduced by a factor of about three to five
for high-energy pion beams in the meson cave. About 10 to 20% of
the beam was located in the first 200 $\mu$sec of the spill and corresponded
to very high instantaneous intensity. The electronics system of the
experiment was gated off during this so-called "spike."

The measurement of the probability of more than one pion's
being in one bunch was based on the assumption that the probability
of two particles' being in two specified bunches is independent of which
two bunches are specified. In other words, the number of times two
pions are in one bunch equals the number of times one pion is in one
bunch and another pion is in the next bunch 54 nsec later.

The phototube pulses from all the counters in the system
triggered tunnel-diode discriminators (4X-6381-18) whose outputs were
uniform in amplitude and time duration. The zero-time or start signal
was clipping-line-differentiated at the input to the tunnel-diode dis-
criminator to provide better timing information. The direct tunnel-
diode output of the discriminator was used as the start signal in the
time-analysis sytem. The signals that were used in anticoincidence
were amplified to 2 volts in order to comfortably satisfy the amplitude
requirements of the anticoincidence input of the coincidence circuits.
A beam pion gave a 123 coincidence, and a 123$\bar{4}$ response ($\bar{\phantom{x}}$ denotes
anticoincidence) indicated that the pion had interacted in the target.
The resolving time of the coincidence circuits was 10 nsec.

Bunching measurements were made by inserting 54 nsec in any
of the signals 1, 2, or 3. The relative probability of more than one

pion in a fine-structure pulse was 1.9% for all beam pions (123) and < 0.1% for interacting pions (123$\bar{4}$). The 4 signal was also placed in anticoincidence in the 123 circuit after a 54-nsec delay to compensate the monitor for cases in which two pions were in one bunch and one interacted but the other passed through counter 4 and killed the event. The 20-Mc discriminator-scaler consisted of a 20-Mc tunnel-diode discriminator—octal scaler circuit (4X-6383-16) whose output triggered a 10-Mc transistor discriminator which drove a 5-Mc transistor decade scaler.

As stated above, the electronic system was gated off during the beam spike. All scalers in the system were controlled by this gate signal. In addition the system was gated off during the time the pulse-height analyzer was busy. One of the monitor scalers was also controlled by this gating signal. This dead-time correction was always less than 0.1%. The monitor 20-Mc discriminator-scaler system was doubled for reliability.

The tunnel-diode discriminator thresholds were set at 100 mV. Phototube high-voltage plateaus and delay curves were determined for each counter. The counting rates as a function of threshold of the discriminator following each coincidence circuit were measured. All the corresponding settings were such that the system was insensitive to any reasonable fluctuation. If the two coincidence circuits were both set to measure the same quantity (123 or 123$\bar{4}$) the circuits agreed to within 0.1% at all beam intensities.

b. Routing section

A cylindrical scintillator viewed by two RCA 6810A phototubes surrounded the target vacuum chamber. A cross section of this counter, 5, is shown in Fig. 6. This counter determined whether or not the neutron had been accompanied by charged particles. The two photo-tubes 5 and 5' were calibrated for equal gain settings. Their outputs were mixed and then triggered a tunnel-diode discriminator whose output was placed in both coincidence and anticoincidence with the output of the 123$\bar{4}$ circuit. A 123$\bar{4}$5 response indicated an interacting incident pion with charged reaction products. A 123$\bar{4}\bar{5}$ response indicated

an interacting incident pion with all neutral reaction products. The outputs of the discriminators following these coincidence circuits were the inputs to one side of a two-by-two diode coincidence matrix (4X-6381-12). The other two inputs were signals indicating the detection of a neutral particle in either the N1, N1' pair or the N2, N2' pair of neutron counters. The four possible outputs each triggered a fixed-level discriminator (4X-6382-15) which produced an output pulse of the proper polarity and duration to supply the external routing inputs of a 400-channel pulse-height analyzer (PHA). The analyzer was used in the external routing-four quadrant mode of operation. For example, data stored in locations 000-099 corresponded to N1, N1' accompanied by charged particles, locations 100 to 199 to N1, N1' accompanied by no charged particles, etc.

The OR circuit (4X-6381-17) prevented ambiguous combinations of routing and signal inputs from reaching the PHA. If one and only one of the outputs of the coincidence matrix were present the OR circuit produced an output of proper amplitude and polarity to trigger the delayed coincidence input in the analyzer. Thus each input signal that was analyzed was accompanied by one and only one routing pulse. The frequency of arrival of signals for analysis at the PHA was low enough to exclude any problems involving loss of efficiency due to this circuit.

c. Neutron-detection and time-analysis section.

Neutrons were detected by the light produced by the charged products of interactions between the incident neutrons and the hydrogen and carbon nuclei of the scintillator. The efficiency of this detection method is a function of the lowest light output the system can detect. In order to set this threshold it was necessary to maintain a reasonable pulse-height resolution. The scintillator size and geometry were limited by this requirement and by the allowable spread in angle subtended at the target by the detector. On the other hand, a lower limit was placed on the total area of detector by counting-rate considerations. These factors determined the number of neutron counters used to be

four. However, the number of PHA memory quandrants available
required that the outputs be combined into the two pairs.

Figure 8 is a photograph of a disassembled neutron counter and
the anticoincidence counter that surrounded it. The detector was a
4-in. -thick piece of plastic scintillator with 40-in.$^2$ cross-sectional
area. The front face of the anticoincidence counter was 3/8 in. thick
and the molded side walls 1/4 in. thick. The scintillator was viewed
by an RCA 6810A phototube through a lucite light pipe. The anti-
coincidence counters were voltage-plateaued and timed in the pion
beam. Each was determined to be > 99.5% efficient in anticoincidencing
the beam pions.

A phototube with a 5-1/4-in. -diameter photocathode was used
in order to obtain efficient light collection from a large piece of scin-
tillator. The Amperex 58AVP phototube was selected because it had
the best timing characteristics of the tubes with a large photocathode.
The pulse rise time was slightly better, and the cathode transit time
differences considerably better, than with any other phototube available.

The design specifications for the neutron time-of-flight system
were (a) time resolution less than 1.0 nsec over a range of input pulse
amplitudes corresponding to 100 to 10,000 photoelectrons, and (b) a
linear dynamic range of 100 nsec. The basis for the first requirement
was a desire that the system have no systematic time shift for pulse
amplitudes falling between the extremes expected in the detection of
neutrons in this experiment. The lower limit corresponds to the
lowest scintillation light threshold expected, 1.0 MeV equivalent elec-
tron energy. The upper limit corresponds to the scintillation light
produced by a recoil proton with a range equal to the thickness of the
counter. This energy was 120 MeV and the equivalent light output was
100 MeV (see Appendix B). The second specification allowed measure-
ment of neutron energies down to 5 MeV at the expected flight path.
The critical components in the system were the phototube, the photo-
tube base, the discriminator triggered by the phototube, and the time-
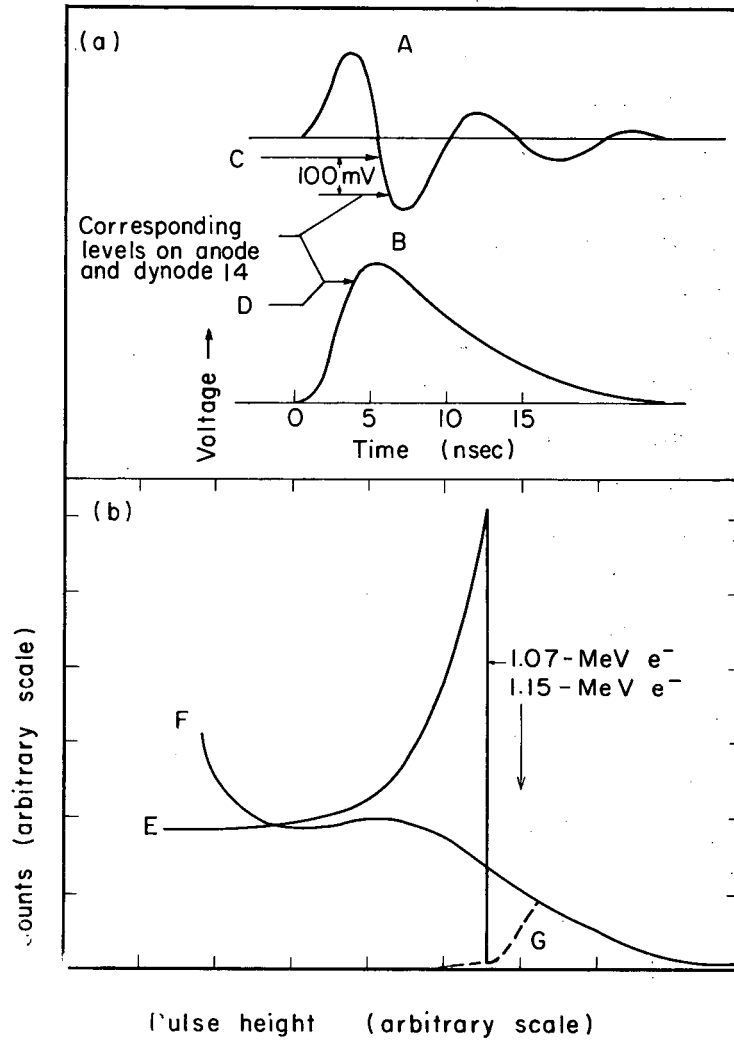to-height converter (THC). The final combination adopted had a time

ZN-3409

Fig. 8.  Disassembled neutron counter.

resolution of 0.5 nsec (full-width-half-maximum) in light pulser tests.[20]
The method of obtaining the timing information from the phototube signal
was pulse differentiation by an overdamped LC-tuned circuit to produce
a zero-crossing signal whose zero-crossing point was detected by a
tunnel-diode discriminator.[21]

In order to prevent pulse saturation, which would spoil the
timing information of the differentiated pulse, the photomultiplier base
was a graded voltage divider chain. A normal signal was taken from
dynode 14 and the anode signal was differentiated by the LC-tuned cir-
cuit located in the base (4X-6382-20). Typical signals are shown in
Fig. 9. The dynode pulse was used for amplitude information and the
anode pulse for timing information.

The threshold for detection was controlled by the discriminator
triggered by the dynode output. This threshold was set with the Compton
edge of the 1.28-MeV $\gamma$ of $Na^{22}$. The maximum Compton electron en-
ergy is 1.07 MeV. The dynode signal was split and stretched for input
to the PHA. The pulse-height spectrum of the $Na^{22}$ source was dis-
played and the threshold of the dynode discriminator set at the location
of the Compton edge. An example is shown in Fig. 9. The pulse-
height resolution of the counters under these conditions of uniform
illumination by gamma rays could be estimated from the shape of the
Compton spectrum and was 30% to 50% for the four counters used.
Attenuators were used in front of the dynode discriminator to set the
threshold at levels higher than 1.07 MeV. The experiment was per-
formed at a threshold of 2.3 MeV equivalent electron energy.

For good timing resolution it was desirable to set the zero-
crossing detector discriminator threshold as close to zero as possible.
It was also necessary that the input pulse exceed this threshold by
approximately 100 mV in order for the delay time to the discriminator
output to be constant to within 1 nsec. To avoid this region near
threshold the amplitude of the zero-crossing signal corresponding to
the threshold of acceptance set by the dynode discriminator must be
at least 100 mV above the threshold of the timing discriminator.

Fig. 9. (a) 58 AVP waveforms.
   A: anode after LC zero crossing;
   B: Dynode 14;
   C: timing discriminator threshold;
   D: amplitude discriminator threshold.
(b) Compton spectrum of 1.28-MeV $\gamma$ from $Na^{22}$, observed
   by neutron detector.
   E: calculated spectrum;
   F: measured spectrum;
   G: measured spectrum cut off by amplitude discriminator.

Satisfaction of this requirement determined the voltage at which the phototube was operated. The direct tunnel-diode output of the timing discriminator was used as the stop pulse in the time-analysis system.

A coincidence $N_A N_T \bar{A}$ (see Fig. 7) indicated the detection of a neutral particle producing enough light to exceed the amplitude discriminator threshold. The summed output of the four coincidence circuits controlled the gate G1(4X-1112-6D). When one of the neutron counters detected a neutral particle within 90 nsec of the arrival of an interacting beam pion the $123\bar{4}$ signal passed through the gate and in turn opened the gates for the start and stop pulses. These gates could be disabled by an external pulse. This was the point at which the system was gated off during the beam spike or a PHA busy condition.

The start and stop signals proceeded to the THC, which actually consisted of two tunnel-diode discriminators (4X-1112-18) to shape the start and stop pulses, the THC (4X-6422A), and an LRL Model V linear amplifier. The THC output provided the PHA with an input pulse whose amplitude was proportional to the separation between the time of arrival of the start and stop signals.

A check was provided on the THC and PHA systems by coincidence circuit START-STOP which sampled a fixed time interval in the spectrum. The output of the coincidence was routed by diode coincidences with the routing pulses. A check on the routing network was provided by determining whether the lower scaler equaled the sum of the four scalers above it.

d. System test routine

Each counter in the system had a light pulser attached. The electrical signals that triggered these lamps passed through a relay matrix which was programmed to produce a sequence of pulses in the various counters that would simulate real events. This test system provided considerable convenience in the system setup and a fast means of checking the operation of the system throughout the experiment. The test routine also included a series of fixed delays to the neutron detectors; these delays gave the time scale calibration for the system.

## B. Experimental Procedures

The time-of-flight system was essentially a double coincidence with 90 nsec resolving time. Random accidental coincidences occurred in the system at a definitely nonnegligible rate. These accidentals were measured by inserting 108 nsec of delay at the points A in Fig. 7. This delayed the entire stop side, including routing, by two fine-structure pulses. Two fine-structure pulses were used to ensure that no real events were included in the accidental measurements. A time of flight of 108 nsec corresponded to a neutron energy that was below the detection threshold, whereas 54 nsec would not have. Relative accidental rates at 374 MeV and 1.4-meter flight path averaged 5%, at 374 MeV and 2.0-meter flight path averaged 10%, and at 417 MeV and 454 MeV averaged 2%.

The measurements were performed in cycles of liquid hydrogen target-full—real, target-full—accidental, target-empty—accidental, target-empty—real. In order to minimize the statistical error in the yield for the available running time the respective amounts of incident pion flux for each type of measurement were proportional to the square root of the ratio of counting rates in each condition.

The members of each pair of neutron counters were operated at the same angle with respect to the beam direction since their outputs were combined in the PHA. The angle of measurement was changed frequently and all angles run by both pairs of counters. Most of the measurements were made with the members of a pair on opposite sides of the beam, but measurements were also made with the counters stacked vertically on one side of the beam.

At the beginning of the experiment it was believed that the time scales of the members of a pair could be aligned with the light pulser system, but it was soon evident that the timing of the lamps had short-term fluctuations of the order of 1 nsec. Subsequently the time scales were equalized by adjusting the relative timing to produce coincidence between the gamma peaks in an individually measured time-of-flight spectrum of each counter. The relative timing was stable to within the order of 1/4 nsec for 12-hour periods.

The neutron-detector threshold were checked every few hours by a rate count with a $Na^{22}$ source. Short-term fluctuations in gain of the phototubes, of the order of 5%, were observed but never understood. If the fluctuation was larger than 5% the threshold of the counter was reset.

The hydrogen target was not defined by the neutron detectors. Presumably the target full-target empty subtraction would eliminate non-target-derived background. To check the validity of the measurement, a large amount of data, particularly at 374 MeV, was taken at a 2.0-meter separation between the hydrogen target and the neutron counters. This decreased the solid angle subtended at the target by a factor of two, and a corresponding decrease in yield should have occurred for target-derived neutrons. This also changes the coefficient for converting time of flight to energy (see Sec. III. F. 3) and might reveal systematic errors in the time-analysis system. The results of this test are discussed in Sec. IV. Table IV. is a list of the measurements made.

## III. DATA ANALYSIS

The memory of the PHA was read out in the form of punched paper tape after each run. For preliminary analysis the information on the punched tape was immediately printed in page form. Later the paper tapes were converted to magnetic tape on the IBM 1401 system. These magnetic tapes were the starting point for subsequent data analysis using the IBM 709-7090 system. All computer programs were coded in FORTRAN for this system.

The first step was to compute the yield per incident pion per PHA channel for hydrogen, $Y_i$, and its statistical error, $\delta_i$. The data from the four quadrants of the PHA memory were separately combined channel by channel for each cycle of runs according to

$$Y_i = \left( \frac{F_i}{M_F} - \frac{FA_i}{M_{FA}} \right) - \left( \frac{MT_i}{M_{MT}} - \frac{MTA_i}{M_{MTA}} \right) ,$$

$$\delta_i = \left( \frac{F_i}{M_F^2} + \frac{FA_i}{M_{FA}^2} + \frac{MT_i}{M_{MT}^2} + \frac{MTA_i}{M_{MTA}^2} \right)^{1/2} ,$$

(6)

where $F_i$, $FA_i$, $MT_i$, $MTA_i$ are the yields in channel i with the experimental system under the conditions, respectively, of hydrogen target full, electronics normal; target full, electronics accidental; target empty, electronics normal; and target empty, electronics accidental. $M_F$, $M_{FA}$, $M_{MT}$, $M_{MTA}$ are the numbers of pions incident on the target in the respective conditions.

The yield as a function of channel number was on a scale proportional to the time of flight from the target to the detector. The objective of the data analysis was to extract the yield of neutrons from the inelastic reactions and to transform it to the differential cross section as a function of neutron energy and direction, $d^2\sigma/dTd\Omega$.

## A. Gamma Peak Analysis

The neutron detectors had a sizable probability (approx 15%) of detecting gammas by the processes of Compton scattering or pair production in the scintillator. Because of their single velocity all gammas from the target were located in one peak in the time-of-flight spectrum. The location of this peak gave an absolute time-scale calibration, and the width of the peak provided a measurement of the time resolution of the system. The principal source of gammas was the two-gamma decay of neutral pions from the charge-exchange reaction. Therefore most of the gammas appeared in the neutral-quadrant data. Gammas from the reactions $\pi^- + p \rightarrow \pi^- + \pi^0 + p$ and $\pi^- + p \rightarrow \pi^- + \gamma + p$ were located in the charged-quadrant data.

To quantitatively determine the location and width of the gamma peak the neutral-quadrant hydrogen yield in the region of the peak was fitted with a function of the form

$$f(N, \sigma, t_0) = \frac{N}{\sqrt{2\pi}\,\sigma} \exp\left(-1/2\left(\frac{t-t_0}{\sigma}\right)^2\right), \qquad (7)$$

where $N$, $\sigma$, and $t_0$ were the parameters varied to minimize the function

$$\chi^2 = \sum_i \left[\left(\int_{t_i^-}^{t_i^+} dt\, f(N, \sigma, t_0) - Y_i\right) / \delta_i\right]^2, \qquad (8)$$

where $t_i^-$ and $t_i^+$ are the times of the lower and upper limits of channel i and the sum extended from approximately 10 nsec before the peak to 3 nsec after the peak. Figure 10 is a typical fit. The values of $t_0$ and $\sigma$ were held constant and the gamma peak in the charged quadrant was fitted with $N$ as a parameter. The $\chi^2$ test of statistical significance[22] was applied to these fits in order to determine the validity of the hypothesis that the gamma peaks were Gaussian in shape. The values of $\chi^2$ obtained in the fits were systematically too

Fig. 10. Neutral-mode time-of-flight spectra (0.5 nsec/channel).
(a) 374 MeV, 2.0 meters, 50 deg;
   A: gamma peak, $\sigma$ = 1.6 channels; B: charge-exchange
neutron peak, $\sigma$ = 2.5 channels; C: inelastic neutrons.
(b) 374 MeV, 2.0 meters, 10 deg;
   A: gamma peak, $\sigma$ = 1.9 channels; B: charge-exchange
neutrons, $\sigma$ = 2.25 channels; C: inelastic neutrons.

MU-28835

high for the degrees of freedom of the fit. Fits were attempted with a function of the form

$$f(N, t_0, \sigma) = \frac{N\sigma}{\pi \left[ (t - t_0)^2 + \sigma^2 \right]} \qquad (9)$$

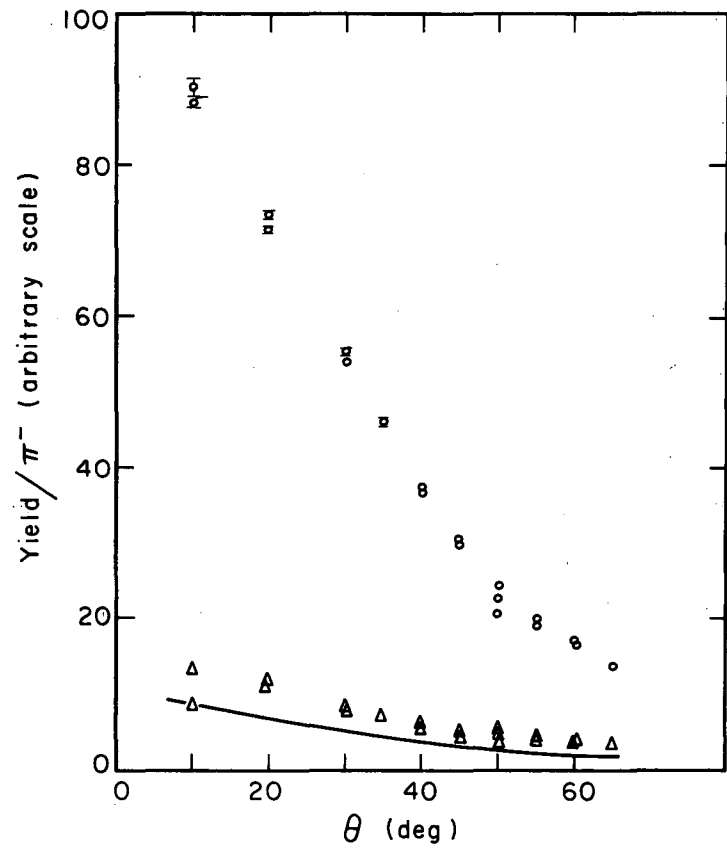The $\chi^2$ values obtained were much worse than for the Gaussian function (Eq. 7). Equation (7) fell off too rapidly and Eq. (9) fell off too slowly. The discrepancies between the observed peaks and the functional forms were understandable. The data were the superposition of the spectra of two counters of the pair, and fluctuations in the relative alignment would change the shape of the peak.

The best-fit yield was subtracted from the hydrogen yield after the error had been increased by the square root of the ratio of $\chi^2$ to the degrees of freedom of the fit. Figure 11 shows the gamma yield (area of the gamma peak) in the neutral and charged modes as a function of laboratory-system angle at 374 MeV. The average value of $\sigma$ obtained in fitting all the runs corresponded to 0.90 nsec for the N1 pair of neutron detectors and 0.75 nsec for the N2 pair. The time scale for each counter pair in each cycle of runs was set by the value of $t_0$ obtained in the fitting procedure.

## B. Time-of-Flight System Resolution

The measured width of the gamma peaks is the resultant of fluctuations in the flight path due to the finite size of the target and the detector and the resolution of the time-of-flight system. The variation in flight path for finite target and counter geometry was computed as a function of laboratory-system angle. Figure 12, a and b, gives the half-width at half-maximum as a function of angle and an example of the relative probability of a given value of flight path at a mean value of 2.0 meters. The fluctuation of flight path was a negligible contribution to the gamma peak width, but was taken into consideration for the slower neutrons ($\beta < 1$). The light-amplitude range produced by the gammas should be equal to that produced by neutrons and therefore the
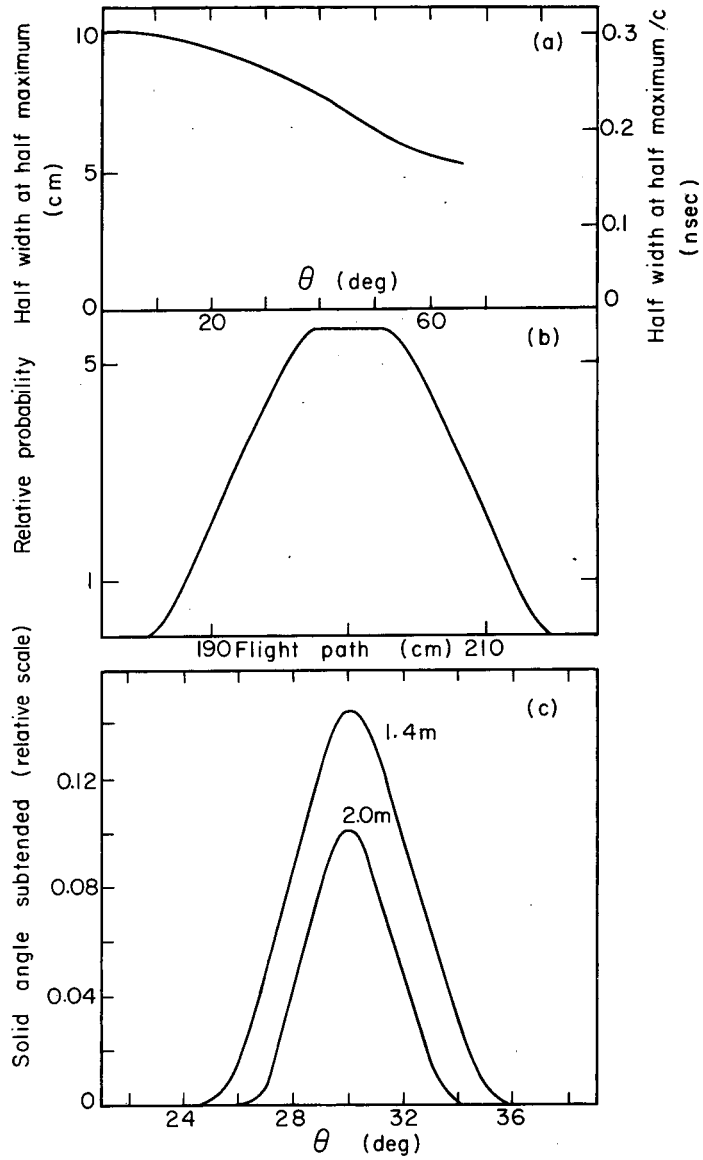
Fig. 11. Gamma yield at 374 MeV.
O: neutral mode
△: charged mode
— : calculated charged-mode yield

MU-28836

Fig. 12. Calculated resolutions.
(a) Flight path resolution function: 1/2 width at 1/2 maximum.
(b) Flight path resolution function for 30 deg, 2.0 meters.
(c) Angular resolution.

width of the gamma peak was a valid measure of the resolution of the time-of-flight system for neutrons.

## C. Charge-Exchange Neutron Analysis

The separation of the neutrons from the charge-exchange and inelastic reactions was much more ambiguous than the gamma situation. At forward angles the separation in time between the charge-exchange neutrons and the maximum-energy inelastic neutrons was of the order of or less than the time resolution of the system. At angles greater than 40 deg the charge-exchange neutrons stood out clearly but the inelastics were less obvious in the tail of the charge-exchange neutron peak in the time-of-flight spectrum.

The overall resolution in measurements of the neutron spectra was more complicated than the problem in the gamma case. The time-of-flight system resolution was only one factor in the total resolution. In addition, the following contributions had to be considered: (a) the finite angular resolution of the neutron detectors; (b) the flight-path uncertainty; and (c) the energy spread of the incident pions. The solid angle subtended by a neutron counter as a function of angle about the mean angle, $\theta$, with respect to the beam direction was computed for the finite target and counter geometry. Integration was performed over the counter volume and the target volume weighted by the beam profiles. Figure 12c is the result for $\theta = 30$ deg at flight paths of 1.4 and 2.0 meters. The spread of charge-exchange neutron energy and the inelastic kinematic limit resulting from the finite angular resolution can be visualized by considering the kinematics diagram (Fig. 1). The kinematics diagram is for a unique incident energy. The energy spread of the beam produced further smearing of the energy spectrum of the neutrons incident upon a counter located at any mean angle, $\theta$. The angular resolution was transformed to resolution in both neutron energy and time of flight. The variation of neutron energy due to spread of incident beam energy was also transformed to neutron time of flight. The effect of uncertainty in the flight path has been mentioned
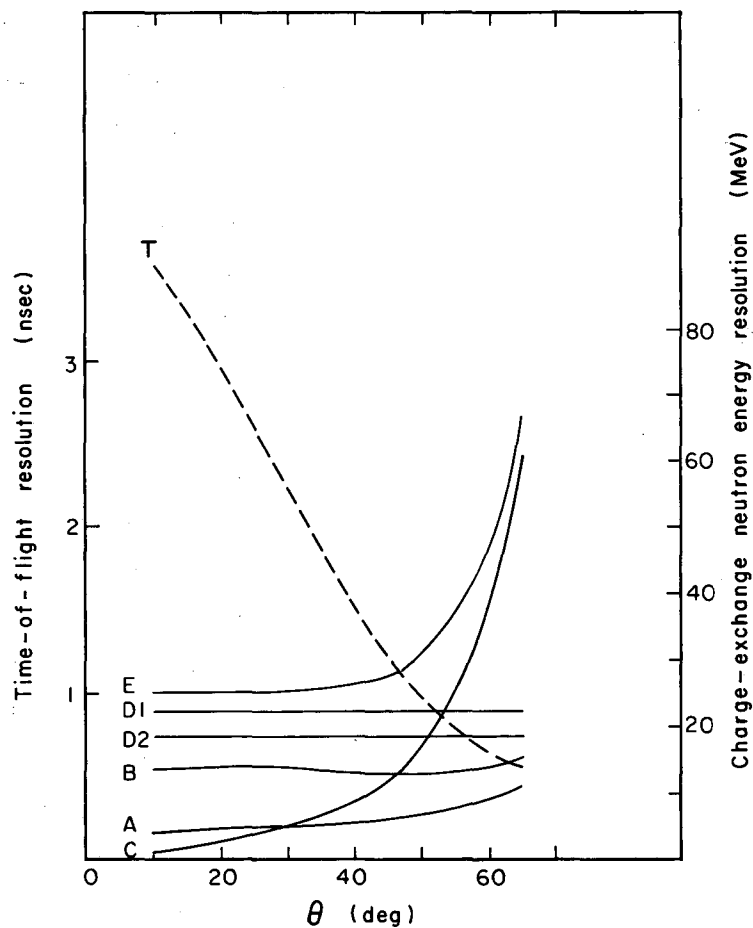
but becomes important for neutrons because

$$\Delta t = \Delta \ell / \beta c \, , \tag{10}$$

where $\Delta \ell$ is the flight path uncertainty, $\beta c$ is the velocity of the neutron, and $\Delta t$ is the resultant uncertainty in time of flight. For the neutron energies under consideration, $0.1 < \beta < 0.7$. The fluctuations in time of flight from these sources were assumed to have a Gaussian distribution and were combined with the time resolution of the time-of-flight system accordingly to give the total resolution. The contributions of each source as a function of $\theta$ are shown in Fig. 13 for charge-exchange neutrons at 374 MeV incident energy and 1.4 meters flight path.

Presumably the existing measurements of the angular distribution for the charge-exchange reaction could have been used to subtract the contribution of the charge-exchange neutrons from the time-of-flight spectra once the resolution discussed above had been determined. However, the best estimate of the charge-exchange angular distribution available in the data of this experiment differs significantly from the measurements by Caris et al.[23] These differences are discussed in more detail in Sec. IV.

For data at angles $\geqslant 45$ deg the charge-exchange neutrons dominated the time-of-flight spectra and were unambiguously subtracted from the spectra. The shape of the charge-exchange peak agreed in all cases with the calculated resolution. An example for 50 deg, 2.0 meters flight path, and 374 MeV incident energy is shown in Fig. 10a. At angles forward of 45 deg the charge-exchange contribution was subtracted by normalizing the area of the calculated resolution function to twice the observed yield between the center of the charge-exchange peak and a point two standard deviations from the center in the direction away from the inelastic portion of the spectrum. Figure 10b is an illustration for 10 deg, 2.0 meters flight path, and 374 MeV.

MU-28838

Fig. 13.  Charge-exchange neutron resolution at 374 MeV,
   1.4-meter flight path.
      A: beam energy spread contribution
      B: flight-path resolution
      C: angular resolution
      D: time-of-flight system resolution:
         1 - N1,N1' pair,
         2 - N2,N2' pair.
      E: total time resolution
      T: Corresponding charge-exchange neutron energy resolution.

## D. Data Combination and Consistency Tests

Each cycle of runs was treated separately to this point in the data analysis. The data in most of the conditions listed in Table IV were taken in at least two different cycles. Normally the time scales of the several cycles were displaced relative to one another and therefore were aligned to the nearest channel before combination. Before the data from these several cycles were combined the results were checked for statistical consistency. The $\chi^2$ test of statistical significance was used to make the check.[22]

The average yield per channel was computed according to

$$\bar{Y_i} = \sum_j Y_{ij}\ \delta_{ij}^{-2} / \sum_j \delta_{ij}^{-2} , \qquad (11)$$

where $j$ denotes the cycle of runs in which the data were taken. By using these $\bar{Y_i}$ the quantities

$$\chi_j^2 = \sum_i \left[ \left( Y_{ij} - \bar{Y_i} \right) / \delta_{ij} \right]^2 \qquad (12)$$

were evaluated. The probability that $\chi_j^2$ would have the calculated value was computed. If one or more cycles had a probability of less than 0.05, the cycle with lowest probability was deleted and the procedure starting with Eq. (11) repeated. In order to catch gross single-channel errors, any cases in which an individual $\left| \left( Y_{ij} - \bar{Y}_i \right) / \delta_{ij} \right| \geq 3$ were also noted. All cycles of runs performed were included in this analysis regardless of a prior knowledge that mistakes had been made in some portion of the experimental procedure for some cycles. The consistency test was successful in identifying and deleting these cases. It was not necessary to delete data for which there was no known instrumental or procedural error.

## E. CORRECTIONS

The corrections discussed in this section are divided into four categories:.

1: those applied to the beam monitor;

2: the effects of rescattering of the products of elastic and charge-exchange interactions of the incident pions;

3: the effects of conversion of gammas leaving the hydrogen target; and

4: the absorption losses and rescattering of inelastic neutrons. The first correction was a straightforward adjustment of the normalization. The other processes affected the data in a more complicated way. Normally the particles from elastic processes could be distinguished by their energy. However, the energy lost in a rescattering process could result in a final neutron whose energy was in the kinematically allowed range for an inelastic reaction. These contributions were subtracted from the total neutron yields. Any charged particles produced by gamma interactions in the target could cause the incorrect determination by the electronic system of the reaction identity. The relative numbers of events in the charged (reaction 3) and neutral (reaction 5) modes were corrected for these effects. Finally, the observed inelastic differential distributions contain distortions introduced by the interactions of the inelastic neutrons in the target. An estimate was made of the magnitude of these distortions.

1. Beam Monitor Corrections

The determination of the muon and electron contaminations in the beam was discussed in Sec. II. A. 1. Since these particles did not interact strongly with the target protons, the incident flux was corrected to correspond to the fraction of pions in the beam.

Another correction was applied specifically to the flux used in analysis of data for the charged mode. A correction was necessary to compensate for the fraction of interactions in which one of the charged pions accompanying the neutron registered in Counter 4 and "anticoincidenced" the event. This fraction was calculated by using the

previously measured $\pi^+$ angular distribution.[8] The $\pi^-$ angular distribution was assumed to be identical. This calculation computed the average loss to be 5%. Actually the correction would be a function of the neutron energy and angle, but insufficient knowledge of the dynamics of the reaction exists to enable a more detailed correction to be calculated.

## 2. Charge-Exchange Neutron Rescattering

The following four double-scattering processes were considered:

| Direct | Rescattering |
|---|---|
| | $n + p \rightarrow n + p$ |
| $\pi^- + p \rightarrow \pi^0 + n$ | $n + C \rightarrow n' + X$ |
| | $n + Al \rightarrow n' + X$ |
| $\pi^- + p \rightarrow \pi^- + p$ | $\pi^- + p \rightarrow n + \pi^0$ |

$$(13)$$

The effects of rescattering in an experiment using a target surrounded by a small amount of material are usually small in comparison with the direct process. In comparison with another reaction with smaller cross section these effects may be significant. The cross sections for the direct processes in this experiment were an order of magnitude larger than those expected for the inelastic modes. The cross sections for the rescattering processes were two to three orders of magnitude larger.

An initial estimate of the relative importance of four reaction combinations was made by computing the total rescattering cross section,

$$\sigma_T^r = \int d\Omega_1 \ \frac{d\sigma_1}{d\Omega} (\theta_1) \ nt(\theta_1) \ \sigma_2^T (T_1(\theta_1)) , \qquad (14)$$

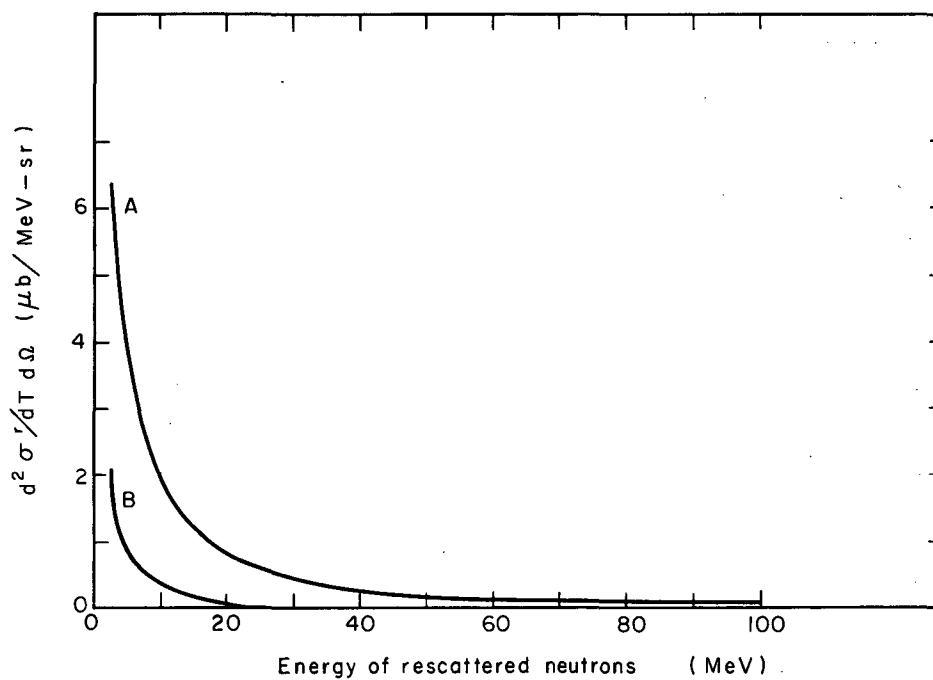for each process. Here $d\sigma_1/d\Omega$ is the differential cross section for the primary process, $nt$ is the number of scatterers per $cm^2$ for the rescattering reaction, $\sigma_2^T$ is the total cross section for the rescattering reaction at incident energy $T_1$. As indicated, $d\sigma_1/d\Omega$, $nt$, and $T_1$ are functions of $\theta_1$, the angle of emission in the direct process.

The limit of integration for the first three processes of (13) was $0 \leq \theta_1 \leq$ (a value such that $T_1(\theta_1) = 10$ MeV). This limit was chosen to estimate the contribution for rescattered neutron energies greater than 10 MeV, which was the lower energy limit of the data analysis. For the second and third of Reactions (13), $\sigma_2^T$ actually used in the calculation was the total cross section minus the estimated elastic scattering for angles less than the first diffraction minimum (see Appendix B for more details of this estimate). For $T_1 \geq 20$ MeV almost all the elastic scattering is in this category. The energy and direction of the neutrons scattered into the first diffraction peak were changed very little. Therefore these neutrons would not fall into the kinematically allowed region for inelastic neutrons. The values of $\sigma_T^r$ at 374 MeV incident pion energy were 0.38 mb, 0.18 mb, 0.09 mb, and 0.05 mb, respectively, for the four Reactions (13).

These results indicated that the first reaction was most important. Fortunately this reaction was the most amenable to a detailed treatment. This calculation is described in Appendix A. The result of the calculation is $d^2\sigma^r/dTd\Omega$ for the final neutrons from the double scattering process as a function of neutron angle and energy. Figure 14 shows $d^2\sigma^r/dTd\Omega$ for 50 deg. The strong rise at low energies is a property of the results at all angles. The calculated charged-mode yield was consistently much smaller than the neutral-mode yield.

In the absence of detailed computations the neutron distributions from the last three of Reactions (13) were assumed to be identical to those calculated for the first reaction. The correction applied to the data was the sum of the distributions weighted by the respective values of $\sigma_T^r$. The magnitude of this correction may best be seen by comparing Fig. 14 with the $d^2\sigma/dTd\Omega$ for the inelastic reactions (shown in Fig. 16).

An approximate hand calculation of the effects discussed here was performed prior to the experiment. The result indicated that the effect might have been sizable in comparison to the inelastic yields at angles greater than 40 deg. To test this conclusion in the charged

MU-28839

Fig. 14. Differential energy distribution of double-scattered
   neutrons at 374 MeV, 50 deg.
      A: neutral mode
      B: charged mode

mode a second cylindrical counter, designated 5', was placed around Counter 5 (see Fig. 6) and 1/8 in. of Cu placed between them. Routing to the charged-mode quadrants of the PHA was made to require a $123\overline{4}55'$ coincidence, which should eliminate few of the inelastic neutrons that are accompanied by at least one fast pion. However, the rescattered charge-exchange neutron would be accompanied by a relatively short-range proton and hence be routed to the neutral-mode quadrant if the proton did not traverse both cylindrical counters and the Cu. No statistically significant change was observed in the charged-mode distributions. This agreed with the results of the calculation for the charged mode.

### 3. Gamma Conversion

A fraction of the all-neutral final-state reactions did not appear in the neutral mode data because: (a) a gamma in the final state interacted with material in the target or surrounding counters and produced an $e^+, e^-$ pair, or (b) a neutral pion decayed in the $\pi^0 \to \gamma + e^- + e^+$ mode. If one of the resulting charged particles passed through Counter 4 the event was lost. If one passed through Counter 5 the event was routed to the charged quadrants of the PHA.

In order to make the necessary correction the average conversion probability for gammas originating in the charge-exchange reaction and of those originating from an inelastic neutral pion must be known. The calculation of this quantity is described in Appendix C. The average probability of conversion, $\epsilon$, is given in Table V. The branching ratio for the internal-conversion mode of $\pi^0$ decay, $\epsilon_d$, equals 0.012.[24] The neutral-quadrant data were multiplied by the factor $1/(1 - \epsilon_d - 2(\epsilon_4 + \epsilon_5)_{cx})$ for the charge-exchange neutrons and by the factor $1/(1 - 2\epsilon_d - 4(\epsilon_4 + \epsilon_5)_{in})$ in the inelastic portions of the time-of-flight spectrum. The corresponding fractions of the neutral-mode yield were subtracted from the charged-mode data.

To check this calculation some data were taken with 0.020 in. of Cu between the target vacuum jacket and Counter 5 to increase the conversion of gammas by a calculable amount. Table V gives the

calculated conversion probabilities and a comparison of the observed
and predicted results of the Cu measurements.

Table V. Gamma conversion probability and results with 0.020 in. Cu

| Charged product in counter | Conversion probability per $\gamma$ | |
|---|---|---|
| | Charge exchange | Inelastic |
| 4 | 0.002 | 0.0005 |
| 5 | 0.027 | 0.020 |
| 5 with 0.020 in. Cu | 0.060 | 0.045 |

| Type of particle | Angle (deg) | Ratio: $\dfrac{\text{Yield with 0.020 in. Cu}}{\text{Yield without Cu}}$ | |
|---|---|---|---|
| | | Observed | Calculated |
| Gamma | 10 | 0.96 ± .03 | 0.93 |
| Charge-exchange neutron | 60 | 0.97 ± .03 | 0.93 |
| Inelastic neutron | 10 | 0.90 ± .06 | 0.89 |

The gamma conversion also contributed to the gamma peak in
the charged-mode spectra (see Sec. III. A). A comparison of the pre-
dicted charged-mode yield and the actual measurements constituted
another check on this calculation. The line in Fig. 11 is the predicted
yield from gamma conversion and the $\pi^0 \pi^- p$ mode. There are three
possible explanations for the remainder of the charged-mode gamma
yield:

(a) the reaction $\pi^- p \to \gamma \pi^- . p$, measured to be $\approx 0.1$ mb at 340 MeV,[25]

(b) the fourth of the rescattering reactions (13), and

(c) elastic $\pi^-$ ($\beta \approx 1$) rejection inefficiency in the anticoincidence
counters.

A 1.3% inefficiency would account for the entire discrepancy in Fig. 11
(in Sec. II. A. 3 the measured inefficiency was < 0.5%). Taken together,
these factors restore consistency between the predicted and observed
results.

## 4. Inelastic Neutron Rescattering and Absorption

The effectiveness of hydrogen, relative to carbon and aluminum, as a neutron scatterer increases with decreasing energy.[26] The lower average energy of inelastic neutrons caused interactions with hydrogen to be more predominant than in the case of charge-exchange neutrons (see Sec. III. E. 2). No neutrons were lost in the interactions with hydrogen because all the scattering was elastic. However, the differential distribution in energy and angle was distorted. The details of this distortion were not calculated; however, the magnitude of the effect was estimated. The fraction of inelastic neutrons that rescattered in hydrogen, $f_r$, was calculated for a statistical differential distribution in energy and angle, $d^2\rho/dTd\Omega$,

$$f_r = \int d\Omega \left( \int dT \; \frac{d^2\rho}{dTd\Omega} \; \sigma_{np}(T) \right) nt(\theta),  \tag{15}$$

where notation is analogous to that in Eq. (14). At 374 MeV incident pion energy $f_r$ was 0.046, which indicated that the total average effect was not large in comparison with the statistical weight of the data. However, the rapid rise of $\sigma_{np}(T)$ as T decreased would cause the effect to be strongly energy-dependent.

No correction was applied to the data to compensate for this distortion. The qualitative behavior would be to shift the neutrons down in energy. The smearing of the angular distribution would be greatest at low energies because, in addition to the rise of $\sigma_{np}$, the angular distribution of np scattering becomes more isotropic as the energy decreases. Therefore, the differential distributions for neutron energies below 50 MeV should be regarded with increasing reservation as the energy decreases.

The data were corrected for losses of neutrons due to reactions with carbon and aluminum in which no neutron existed in the final state $[C^{12}(n, a)Be^9, Al^{27}(n, p)Mg^{27}, \text{etc.}].$[26] The total magnitude of this correction was approximately 1%.

## F. Transformation to Differential Cross Section

The double differential cross section $d^2\sigma/dTd\Omega$ as a function of neutron energy and angle for inelastic neutrons was calculated from the formula

$$\overline{Y}_i = \frac{d^2\sigma}{dTd\Omega} (T_i, \theta) \, \epsilon (T_i) \, \Delta\Omega \, nd \left|\frac{dT}{dt}\right|_i \Delta t, \tag{16}$$

where $\overline{Y}_i$ is the yield defined in Sec. II. B corrected as described in Sec. III. E. Here $T_i$ is the energy corresponding to channel i, $t_i$ is the time of flight corresponding to channel i, $\left|\frac{dT}{dt}\right|_i$ is the Jacobian of the transformation from time to energy in channel i, $\Delta t$ is the time width per PHA channel, $\epsilon (T_i)$ is the neutron detection efficiency at energy $T_i$, $\Delta\Omega$ is the solid angle subtended by the neutron detector, n is the number of target protons per cm, and d is the mean length of the hydrogen target (see Sec. II. A. 3). The evaluation of these quantities is described in this section.

### 1. Solid Angle

The solid angle subtended by a neutron detector at the hydrogen target, averaged over the finite detector and target geometry, was computed by the program that calculated the flight path fluctuations (see Sec. III. B). If $P(\ell)$ is the relative probability of flight path $\ell$ computed by the program, then

$$\Delta\Omega = A / \left[\int P(\ell)\ell^2 d\ell \Big/ \int P(\ell)d\ell\right] , \tag{17}$$

where A is the cross sectional area of the counter. For a mean $\ell$ of 1.4 meters, $\Delta\Omega$ was 0.01312, and for a mean $\ell$ of 2.0 meters, $\Delta\Omega$ was 0.00642.

### 2. Detection Efficiency

The neutron-detection efficiency of plastic scintillator is a function of the neutron energy, the threshold for detection of scintillation light, and the detector geometry. Appendix B describes a program that computes the efficiency as a function of these variables. The calculated detection efficiency as a function of neutron energy for the

detector used in this experiment is shown in Fig. B-3 (in Appendix B). The uncertainty estimated for the calculated value of the efficiency was ± 10%. This uncertainty was not included in the errors quoted for the results of the measurement because it was impossible to make a reliable estimate of it. The magnitude of the uncertainty quoted is regarded as an upper limit.

3. Conversion to Energy Scale

The conversion from channel number to time of flight may be expressed as

$$t_i = i \, \Delta t + C. \tag{18}$$

The $\Delta t$ was determined by the fixed delays of the electronic system test routine (Sec. II.A.4) to be $0.505 \pm .010$ nsec/channel. C was obtained from the gamma peak fits (Sec. III.A) by

$$C = \ell/c - t_0 \, \Delta t, \tag{19}$$

where $t_0$ is the channel location of the gamma peak and $\ell$ is the flight path.

The relationships

$$\beta_i = \ell/t_i c, \quad \gamma_i = 1/(1-\beta_i^2)^{1/2}, \text{ and } T_i = M(\gamma_i - 1), \tag{20}$$

where M is the neutron mass, were used to transform time of flight to neutron energy. The Jacobian of this transformation is given by

$$\left| \frac{dT}{dt} \right|_i = Mc (\beta_i \gamma_i)^3/\ell. \tag{21}$$

## G.  Integrated Cross Sections

The integral of the double differential cross section over energy was evaluated by the summation

$$\frac{d\sigma}{d\Omega}(\theta) = \int_{10\,MeV}^{T^+} dT \; d^2\sigma/dTd\Omega = \sum_{i}^{N} \frac{d^2\sigma(T_i,\theta)}{dTd\Omega} \; \Delta T_i \;,$$

(22)

where $\Delta T_i = \left|\frac{dT}{dt}\right|_i \Delta t$.

The lower limit of 10 MeV corresponds to the longest time of flight measured. The upper limit, $T^+$, was the inelastic kinematic limit at the angle $\theta$. In the sum over channels, the $N$ that corresponds to $T^+$ was taken as the channel which included the point on the time scale two half-widths of the total resolution (see Sec. III. C) past the kinematic limit. At values of $\theta$ such that inelastic neutrons were not kinematically allowed, $N$ was taken as the channel that included the point on the time scale three half-widths of the total resolution from the location of the charge-exchange neutrons.

The integral of $d\sigma/d\Omega$ over $d\Omega$ (i.e., the total cross section) was also evaluated by a summation,

$$\sigma_T = \int d\Omega \; \frac{d\sigma(\theta)}{d\Omega} = 2\pi \sum_{j} \frac{d\sigma}{d\Omega}(\theta_j) \; \Delta \cos\theta_j,$$
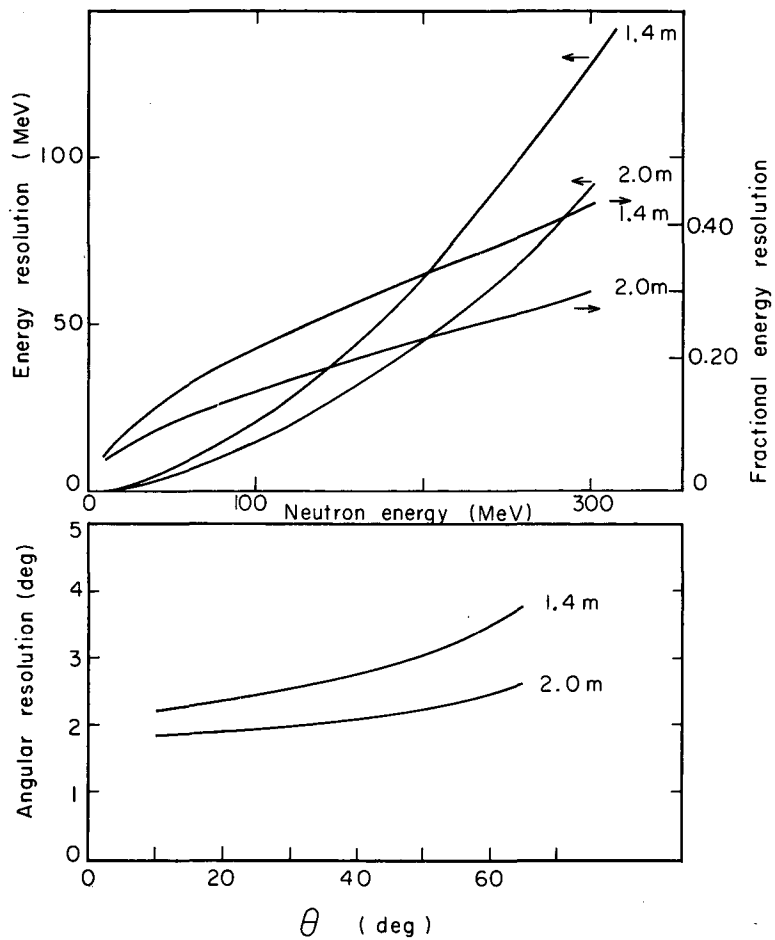
(23)

where $\Delta \cos\theta_j$ for each $j$ was taken to extend one-half the distance between the adjacent measured points. Use of this value for $\Delta \cos\theta_j$ assumed that $d\sigma(\theta_j)/d\Omega$ was an average over this region. Since for almost all values of $\theta_j$ the angular resolution (see Sec. III. C) was greater than or equal to $\Delta \cos\theta_j$, this assumption was valid. The total cross sections at 454 MeV incident pion energy were estimated from the measurements at $10$ deg $\leqslant \theta_j \leqslant 25$ deg by normalizing to the sums obtained for the same interval at 374 MeV and 417 MeV.

## IV. RESULTS

### A. Summary of Resolution and Errors

Before the results of the data analysis described above are
presented a summary of the energy resolution, angular resolution,
and errors is given. The charge-exchange neutron energy resolution
was discussed in Sec. III. C. Since inelastic neutron energy was not
a unique function of direction, the energy and angular resolutions
become essentially independent. The energy resolution was deter-
mined by all the factors considered in Sec. III. C except the angular
resolution. The energy resolution (half-width at half-maximum) as
a function of neutron energy is shown in Fig. 15 along with the angular
resolution (HWHM) as a function of neutron direction. Note that the
resolution with which the experimental system defined the inelastic
neutron kinematic limits corresponded to the charge-exchange neutron
case.

The errors quoted are solely statistical. The uncertainty in-
volved in the subtraction of the accidental background (see Sec. II. B)
is included in this error. The major possible systematic error is the
neutron-detection efficiency (see Appendix B. 3. c). Systematic errors
introduced by inaccuracies in the corrections discussed in Sec. III. E
are negligible compared with the efficiency uncertainty. The sub-
traction of the charge-exchange neutrons described in Sec. III. C does
introduce a much larger uncertainty than indicated by the statistical
errors. The shape of charge-exchange peaks was taken to be Gaussian.
This assumption is poor in the tails of the distribution. Consequently,
the systematic error may exceed the quoted error for neutral-mode
inelastic data separated by less than three half-widths of the charge-
exchange neutron resolution function (Fig. 13) from the charge-exchange
energy. This is particularly true at angles $\geq 45$ deg, since the charge
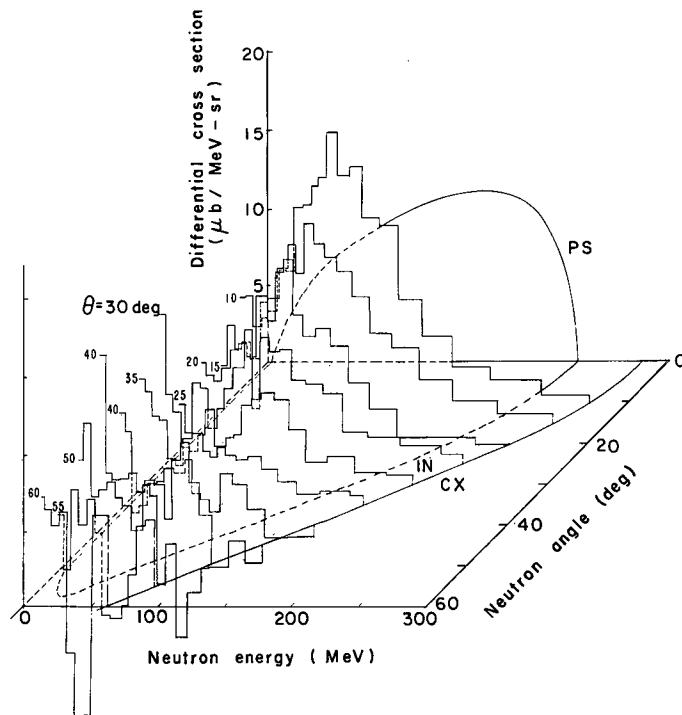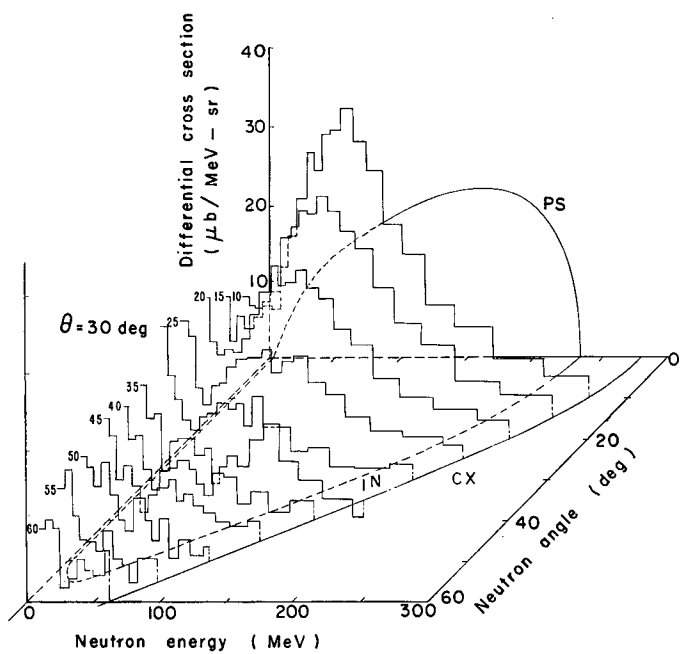exchange neutrons dominate the neutral-mode spectra (see Fig. 10).

Fig. 15. Energy resolution and angular resolution.

MU-28840

## B. Inelastic Neutron Distributions

The differential distributions $d^2\sigma/dTd\Omega$, as a function of neutron energy and direction, are shown in Fig. 16 for 417 MeV incident energy and 1.4 meters flight path. The energy spectra extend from 10 MeV to the charge-exchange neutron energy. The distributions with statistical errors for all the running conditions listed in Table IV are tabulated as a function of neutron energy in Appendix D. The 1.4- and 2.0-meter measurements are statistically consistent except for the low-energy portion of the distributions as discussed below. The distributions presented in Fig. 16 are representative of the data at all three incident energies in both the charged and neutral modes.

Two features are notable: (a) the peaking in the region corresponding to the highest available values of the $\pi\pi$ system energy, $\omega_{\pi\pi}$ (see Fig. 1), and (b) the peaking at low energy, particularly noticeable at angles > 40 deg in the charged mode. Because the first effect also corresponds to an increasing yield as the neutron detector moves towards the beam, the anticoincidence counter efficiencies were rechecked (see Sec. II. A. 4). The 2.0-meter measurements were primarily motivated by a desire to check this high $\omega_{\pi\pi}$ enhancement. All evidence indicated that the effect was real.

On the other hand, it is questionable whether the low-energy peaking was associated with the $\pi\pi N$ final states. It did not fall off at the kinematic limits for these processes. In Sec. III. E. 4 it was pointed out that this region of the energy spectrum should be regarded with reservations. In addition, two spurious sources could produce the observed energy behavior--the double scattering of charge-exchange neutrons (see Fig. 15) and a non-time-correlated background. Correction has been made for the first effect. The second possibility arises because a time-independent background (yield per unit time) transforms to a $1/(momentum)^3$ dependence in the energy spectrum (Eq. 21). The second Counter 5 test (Sec. III. E. 2) also provided a check on the second possibility. The Cu introduced should have attenuated low-energy neutrons. The results of this measurement,

MUB-1492

Fig. 16. Inelastic neutron differential distributions for
(a) charged mode, (b) neutral mode.
Incident $\pi^-$ kinetic energy = 417 MeV; flight path = 1.4 meters.
    CX: charge-exchange energy
    IN: neutron kinematic limits for $\pi N \rightarrow \pi \pi N$
    PS: 0-deg invariant phase-space distribution normalized to
        the total inelastic cross section.

and the comparison of 1.4-meter data with 2.0-meter data, for neutrons in the range 10 to 20 MeV are presented in Table VI. These results were averaged over the measurement angles. The conclusion was that the data in this energy region represented a mixture of hydrogen and background effects.
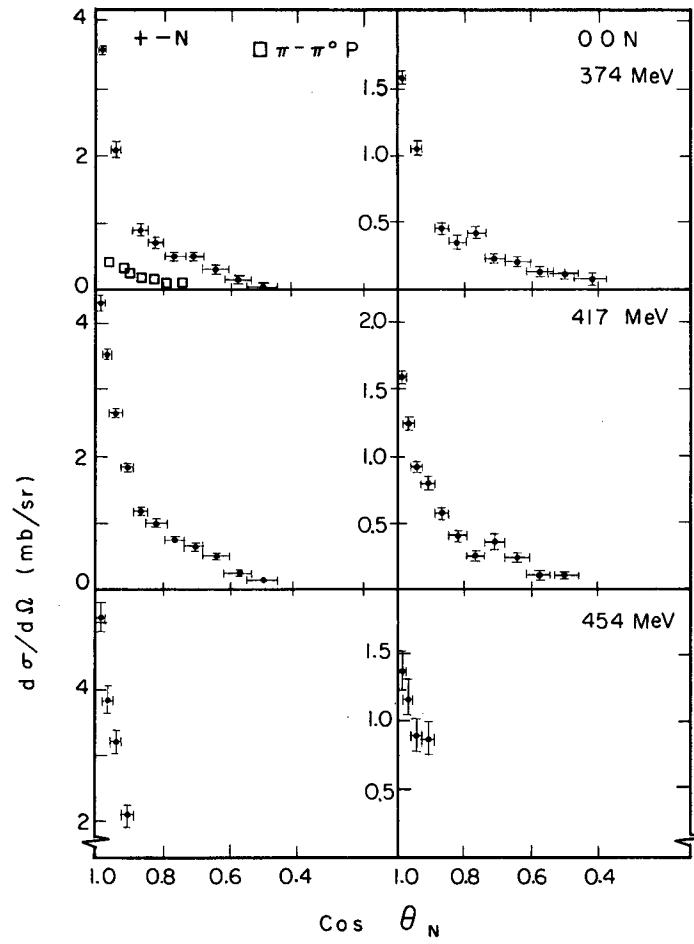
The results for the integrated cross section, $d\sigma/d\Omega$, are presented in Fig. 17. The previous results for the proton in the $\pi^-\pi^0 p$ mode are included for comparison. The total cross sections derived from integration of the angular distributions are presented in Table VII. If the low-energy peaking discussed above was regarded as completely spurious and subtracted, the cross sections were decreased by approx 0.3 mb. A summary of the total-cross-section measurements in inelastic $\pi^- p$ interactions for the energy region of 250 to 500 MeV is contained in Fig. 18. The errors indicated for the measurements of this experiment reflect the uncertainty in the low-energy neutron distribution.

Table VI. Tests on neutrons in the range 10 to 20 MeV.

| Test | (Test-run cross section) / (Normal-run cross section) | | Measured |
|---|---|---|---|
| | Expected | | |
| | Not LH$_2$-derived | Real | |
| 1.4 to 2.0 m | 2.0 | 1.0 | 1.4 ± .1 |
| Counter 5' | 1.0 | 0.86 | 0.93± .1 |

Table VII. Total cross sections for inelastic reactions.
(Indicated errors for cross sections are statistical only; see Sec. IV. A. )

| Energy (MeV) | $\pi^+\pi^- n$ (mb) | $\pi^0\pi^0 n$ (mb) | $\left(\dfrac{\pi^+\pi^- n}{\pi^0\pi^0 n}\right)$ |
|---|---|---|---|
| 374 | 2.77 ± .07 | 1.45± .04 | 1.91± .07 |
| 417 | 3.59± .04 | 1.48± .04 | 2.43± .07 |
| 454 | 4.16± .11 | 1.14± .10 | 3.65± .34 |

Fig. 17. Integrated inelastic neutron angular distributions.

MU-28842

Fig. 18. $\pi^-$p inelastic cross sections.
  1: Reference 4       5: Reference 28
  2: Reference 27      6: Reference 25
  3: Reference 8       7: This experiment
  4: Reference 12      8: Reference 29
  curves represent predictions by Schnitzer (reference 10).
  O: $\pi^+\pi^-$n                    □: $\pi^0\pi^0$n
  △: $\pi^-\pi^0$p                    ▽: $\pi^-\gamma$p

## C. Charge-Exchange Neutrons
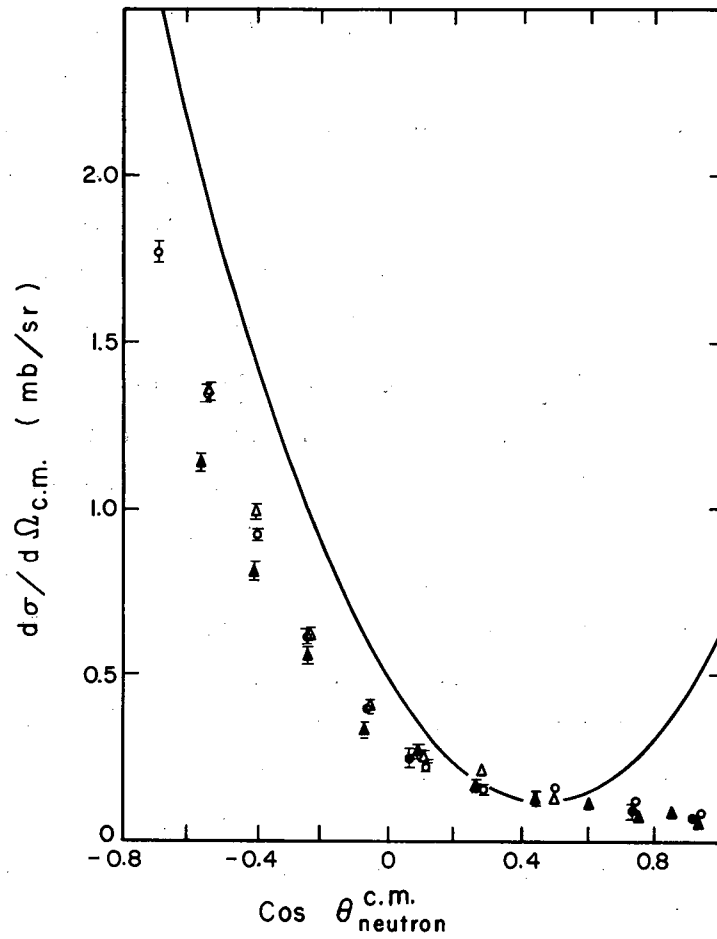
Although the results obtained at angles < 40 deg can be regarded only as an approximation, the results differ from those of Caris[23] sufficiently to be significant. The measured yield was transformed to the c.m. system after correction had been made for gamma conversion and target-rescattering losses. Figure 19 shows the 374- and 417-MeV charge-exchange differential distributions as a function of c.m. scattering angle along with Caris's distribution at 371 MeV. The differences at forward neutron angles (backward $\pi^0$ direction) between the distributions could be a consequence of inelastic $\pi^0$ contamination in the gamma measurements by Caris. This contamination would be maximum in the backward hemisphere (see Fig. C-1).

## D. Total Neutral Cross Section

After correction for gamma conversion (Sec. III.E.3), the $123\overline{45}$ (Sec. II.A.4) yield provided a determination of the total cross section for $\pi^- p \rightarrow$ neutrals. The statistical error of this measurement was completely negligible ( < 0.1%). An estimate of the uncertainty was obtained from the consistency of data taken at different times throughout the experiment. A short run was performed at 391 MeV incident energy to measure the total neutral cross section. The 0.020-in.-Cu measurements (Sec. III.E.3) gave a check on the conversion corrections. The results are listed in Table VIII and shown in Fig. 20 along with other measurements in this energy region.[23, 28, 30]

Fig. 19. Charge-exchange c.m. angular distribution. Curve
represents the data of Caris et al. (reference 23) at
371 MeV.
O: 374 MeV, 2.0 m     ●: 417 MeV, 2.0 m
△: 374 MeV, 1.4 m     ▲: 417 MeV, 1.4 m

MU-28843

Table VIII.  Total neutral cross section.

| Energy (MeV) | Run | Cross Section (mb) | |
|---|---|---|---|
| 374 | 1 | 12.11 | |
| | 2 | 12.27 | |
| | 3 | 12.20 | |
| | 4 | 12.07 | |
| | 5 | 12.15 | |
| | 6 | 12.30 | |
| | 0.020 in. Cu | 12.23 | |
| | Average | | 12.2 ± .1 |
| 391 | 1 | | 12.0 ± .1 |
| 417 | 1 | 11.23 | |
| | 2 | 11.27 | |
| | Average | | 11.25 ± .1 |
| 454 | 1 | | 10.7 ± .1 |

Fig. 20. Total cross section for $\pi^- + p \rightarrow$ neutrals.
  O: Reference 23          ▲: Reference 30
  △: Reference 28        ◐: This experiment

MU-28844

## V. DISCUSSION OF RESULTS

It should be noted that the inelastic neutrons are <u>assumed</u> to be from the $\pi\pi N$ reactions. Only the charge--not the number or identity-- of the particles accompanying the neutron was observed. In terms of these final states there are three interesting features in the data:

(a) the branching ratio $\pi^+\pi^- n/\pi^0\pi^0 n$ compared to Schnitzer's predictions;[10]

(b) the absence of observable effects of the very strong $I = 0$, low-energy $\pi\pi$ interaction corresponding to the results of Abashian, Booth, and Crowe[13] (ABC); and
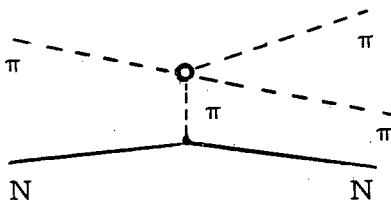
(c) the enhancement of the distributions at high values of the $\pi\pi$ system energy.

The parameters of Schnitzer's calculation were chosen to fit the $\pi^+$ angular distribution in the $\pi^+\pi^- n$ reaction at 430 MeV and the magnitude of the $\pi^+ p$ inelastic interaction at 470 MeV.[11] Therefore, a test of his model comes in its ability to correctly predict the behavior of the other channels. The solid lines in Fig. 18 represent the cross-section predictions of this model. The observed $\pi^0\pi^0 n$ cross section is about two to three times the predicted value, or in terms of the $\pi^+\pi^- n/\pi^0\pi^0 n$ ratio, the prediction is higher than the observation by a factor of two or three. However, the energy dependence of the branching ratio is consistent with the qualitative behavior expected on the basis of a model involving a $\pi\pi$ interaction. Both modes in which the $I = 0$ s-wave $\pi\pi$ state is available rise rapidly from threshold, whereas the $\pi^-\pi^0 p$ mode remains low. As the $I = 1$ p-wave $\pi\pi$ interaction becomes significant the $\pi^-\pi^0 p$ channel begins to rise and the $\pi^+\pi^- n$ mode continues to increase. The $\pi^0\pi^0 n$ channel, without access to the $I = 1$ $\pi\pi$ state, levels off as the s-wave $\pi\pi$ interaction levels off.

The absolute magnitudes of the $\pi^+\pi^- n$ and $\pi^0\pi^0 n$ cross sections in the above interpretation require that the s-wave $\pi\pi$ interaction be appreciable. If it were of the magnitude required to fit the results of ABC the simplest expectation would be a strong enhancement of the regions of the neutron distribution corresponding to the lowest values

of $\omega_{\pi\pi}$. This behavior was not observed. Unfortunately this exactly corresponds to the regions of greatest uncertainty in the measured neutron distributions, i. e., closest to the charge-exchange neutrons or at low neutron energies (see Fig. 1). Because of this uncertainty, together with the fact that the distributions are dominated by a strong enhancement at the opposite extreme of the available $\pi\pi$ energy range, it becomes impossible to make quantitative statements about the ABC effect in $\pi\pi N$ final states. The absence of a strong manifestation of the ABC effect observed here is consistent with the results of Kirz, Schwartz, and Tripp[29] obtained by measurements on the $\pi^+$ and $\pi^-$ of the $\pi^+\pi^- n$ final state. It is not probable that the effect appears solely in the $\pi^0\pi^0 n$ channel, since the results of the ABC measurement are consistent with a ratio of charge states that corresponds to the $I = 0$ $\pi\pi$ state and disfavor possible interpretations as a particle with solely neutral decay modes.

The observed peaking of the neutron distributions at the lowest neutron c. m. momentum (i. e., highest $\omega_{\pi\pi}$ available) has also been observed by Kirz et al.[29] for incident energies between 350 and 450 MeV in their studies of the $\pi^+\pi^- n$ channel. The presence of the effect in the $\pi^0\pi^0 n$ state in this experiment and its apparent absence in the $\pi^-\pi^0 p$ reaction at 377 MeV[12] indicate that it is an $I = 0$ state effect if the $\pi\pi$ interaction is responsible for the enhancement. The simplest assumption would be that a diagram of the type below dominates the $\pi N \rightarrow \pi\pi N$ reactions.

In order to deal more quantitatively with the behavior of the neutron distributions as a function of the $\pi\pi$ system parameters, it is convenient to transform to the Chew and Low variables, $\omega^2$ and $p^2$.[31] The $\omega^2$ is the square of the total energy of all the outgoing particles, excluding the neutron, in their barycentric system. It is specified by the energy and direction of the recoiling neutron. If the neutron-proton mass difference is neglected, $p^2$ is the invariant square of the difference of four-momenta for the target proton and the final-state neutron. The $p^2$ is linearly related to the neutron energy (lab). For fixed $p^2$, $\omega^2$ is proportional to the cosine of the lab angle of the neutron, $\theta$. The Jacobian for the transformation is specified by

$$\frac{d^2\sigma}{dp^2 d\omega^2} = \frac{\pi}{2Mpq_1} \frac{d^2\sigma}{dTd\Omega} , \qquad (24)$$
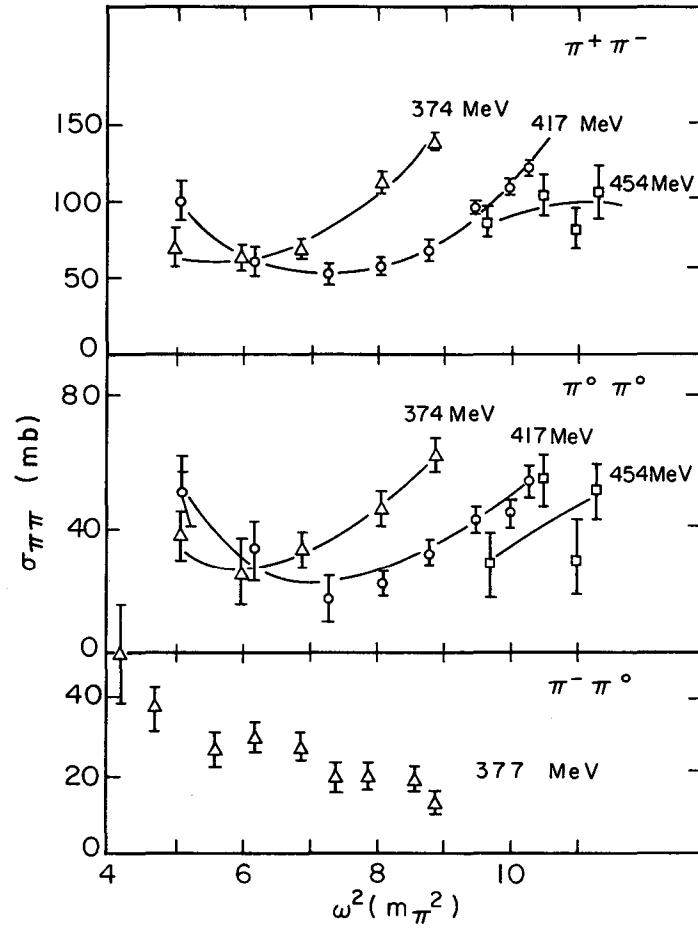
where $q_1$ is the incident $\pi$ momentum and $p$ is the neutron lab momentum. For a diagram of the type under consideration, the quantity $d^2\sigma/dp^2 d\omega^2$ is related to the cross section of the process $\pi\pi \rightarrow \pi\pi$ by

$$\frac{d^2\sigma}{dp^2 d\omega^2} \xrightarrow[p^2 \rightarrow -1]{} C \frac{p^2}{(p^2 + 1)^2} \frac{\omega(\omega^2/4 - 1)^{1/2}}{q_1^2} \sigma_{\pi\pi}(\omega^2), \qquad (25)$$

where $m_{\pi\pi}$ has been taken as unity. If the relationship is assumed to be an equality for physical values of $p^2 > p^2_{min} > 0$, $\sigma_{\pi\pi}(\omega^2)$ can be related to $d^2\sigma/dTd\Omega$. Specifically, for fixed $p^2$ (i.e., fixed T),

$$\sigma_{\pi\pi}(\omega^2) \propto \frac{q_1}{\omega(\omega^2/4 - 1)^{1/2}} \frac{d^2\sigma}{dTd\Omega} . \qquad (26)$$

To investigate the $\pi\pi$ system in the region corresponding to the observed enhancement it was necessary to use a value of $p^2$ quite far from that specified as the limit in Eq. (25). The results of this analysis with $5 < p^2 < 7$ are presented in Fig. 21. The behavior of

Fig. 21. Consistency check of peripheral model.

MU-28845

$\sigma_{\pi\pi}$ as a function of incident momentum indicates that the assumptions of this simple treatment are not valid. Evidence from the second experiment in this program[8] and the studies by Kirz et al. indicate that there are strong effects of the nucleon isobar in the $\pi^+ \pi^- n$ final state[29] to compete with the one-pion exchange diagram considered here. Finally, an interpretation solely in terms of a simple enhanced I = 0 $\pi\pi$ interaction would be inconsistent with the energy dependence of the $\pi^+ \pi^- n / \pi^0 \pi^0 n$ branching ratio.

Suggestions have been advanced of a more complex mechanism associated with the presence of several thresholds in this energy range. In particular, the threshold for the process $\pi N \to \pi N^*_{3,3}$ is located at 395 MeV. The thresholds for the various charge states of the process $\pi N \to 3\pi N$ are located around 360 MeV. Takeda has proposed a model in which the enhancement in the neutron distributions arises from the interference between a process of the type $\pi N \to \pi N^*$ (s-wave final state) and a peripheral process involving a strong I = 0 s-wave $\pi\pi$ interaction.[32] Detailed calculations are in process.

To summarize, a definite deviation from the behavior expected on the basis of a statistical (phase-space) distribution or a simple peripheral collision model has been observed in the distributions of neutrons in inelastic $\pi^- p$ interactions at energies between 350 and 450 MeV. The inelastic neutron differential distributions show a strong preference for low neutron c. m. momenta. The measurements by Kirz et al. indicate that this behavior disappears at energies above 450 MeV.[29] The region below 350 MeV has not been investigated. If it is assumed that the anomaly also disappears below 350 MeV, the energy dependence is suggestive of a mechanism involving a nucleon isobar threshold effect rather than a I = 0, $\pi\pi$ resonance phenomenon.

## ACKNOWLEDGMENTS

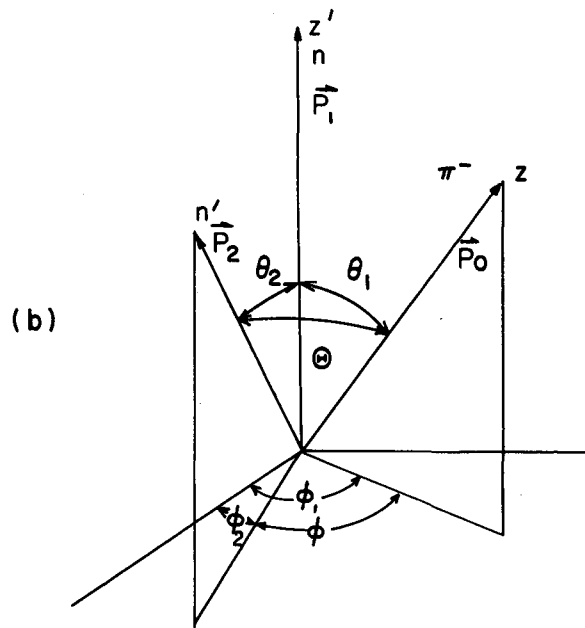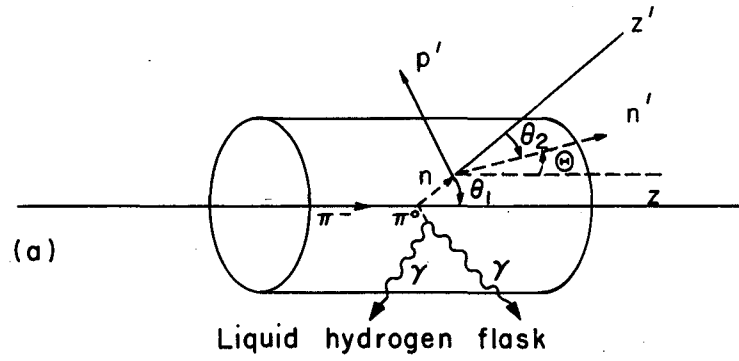## APPENDICES

### A. Charge-Exchange Neutron Double Scattering

The type of double scattering event considered here is sketched in Fig. A-1a. The first neutron, n, has an energy that is a function of the angle $\theta_1$ and the incident pion energy. The rescattered neutron, n', has an energy that is a function of the angle $\theta_2$ and of the energy of n. The direction of n' with respect to the original beam direction, $\Theta$, is also a function of $\theta_1$ and $\theta_2$. For a fixed final direction, $\Theta$, the energy of n' varies as a function of the combination of $\theta_1$ and $\theta_2$ that produces the resultant direction $\Theta$. The differential distribution of n' as a function of energy and direction is computed by the program DBLSCT by use of the known dynamics of the successive processes in the double scattering. The primary charge-exchange scattering is treated as an elastic reaction to facilitate the kinematical calculations. For the same reason the masses in the second scattering are assumed to be equal. Geometrical simplification is introduced by restricting both interactions to the central axis of the cylindrical hydrogen target. Both these approximations are justifiable. The first amounts to neglect of the mass differences between the charged and neutral pion and between the neutron and proton. Since the distance to the detector that fixes the final direction, $\Theta$, is fifty times the radius of the hydrogen target, the second approximation is valid.

The coordinate system and some quantities used in the calculation are shown in Fig. A-1b. Additional definitions are listed in Table A-I.

The starting point for the calculation is

$$dN = n^2 dz \, \frac{d\sigma_1}{d\omega_1} \, (p_0, \theta_1) \, d\omega_1 \, t(z, \theta_1) \, \frac{d\sigma_2}{d\omega_2} \, (p_1, \theta_2) \, d\omega_2, \tag{A-1}$$

which represents the differential number of neutrons arising from a first scattering in the element of target dz into $d\omega_1$, at $\theta_1$, followed by a second scattering into $d\omega_2$ at $\theta_2$. The calculation consists of transforming this quantity to $d^2\sigma(T_{n'}, \Theta)/dT_{n'} d\Omega$.

(a)

(b)

MU-28846

Fig. A-1.  Double-scattering coordinate system.

Table A-I. Symbols used in Appendix A.

| | |
|---|---|
| $x_i$ | $= \cos \theta_i$, for $i = 1, 2$ |
| $X$ | $= \cos \Theta$ |
| $\phi$ | $= \phi_1 - \phi_2$ |
| $y$ | $= \cos \phi$ |
| $p_0, E_0$ | = laboratory-system momentum and total energy of the incident pion |
| $p_1, E_1$ | = laboratory-system momentum and total energy of n |
| $p_2, E_2$ | = laboratory-system momentum and total energy of n' |
| $p_3, E_3$ | = laboratory-system momentum and total energy of p' |
| $z$ | = distance in the beam direction |
| $\ell, r$ | = hydrogen target length and radius |
| $\beta_1$ | = velocity of the center-of-mass system of the first scattering |
| $\beta_2$ | = velocity of the center-of-mass system of the second scattering |
| $M$ | = rest mass of the nucleon |
| $t(z, \theta_1)$ | = distance to escape the cylindrical liquid hydrogen flask for a scattering at z into direction $\theta_1$ |
| $d\sigma_i/d\omega_i$ | = differential cross section of scattering i as a function of $\theta_i$ |

Two equations are critical in the problem,

$$X = x_1 x_2 + \left[ (1 - x_1^2)(1 - x_2^2) \right]^{1/2} y \qquad \text{(A-2)}$$

and

$$P_2 = 2 x_1 x_2 \beta_1 M / (1 - x_1^2 x_2^2 \beta_1^2). \qquad \text{(A-3)}$$

Equation (A-2) is the expression for the cosine of the angle between two vectors. Equation (A-3) is derived by successive use of the Lorentz-invariant relationship for elastic collisions,

$$\Delta P_i \cdot P = 0, \qquad \text{(A-4)}$$

where P is the total four-momentum of the system and $\Delta P_i$ is the four-momentum transfer of particle i in the collision. Applying Eq. (A-4) to the neutron in the first scattering, one has

$$- P_0 P_1 x_1 + E_1 (E_0 + M) - M(E_0 + M) = 0,$$

$$E_1 = P_0 P_1 x_1 / (E_0 + M) + M,$$

$$E_1 = \beta_1 P_1 x_1 + M,$$

$$P_1^2 + M^2 = \beta_1^2 P_1^2 x_1^2 + 2M\beta_1 P_1 x_1 + M^2,$$

$$P_1 = 2\beta_1 M x_1 / (1 - \beta_1^2 x_1^2). \qquad \text{(A-5)}$$

If the masses are considered equal, the same relationship holds for the neutron in the second scattering, i.e.,

$$P_2 = 2\beta_2 M x_2 / (1 - \beta_2^2 x_2^2). \qquad \text{(A-6)}$$

But,

$$\beta_2 = p_1/(E_1 + M),$$

and if Eq. (A-5) is substituted for $p_1$,

$$\beta_2 = x_1\beta_1,$$ (A-7)

so that one has

$$p_2 = 2\beta_1 M x_1 x_2/(1 - \beta_1^2 x_1^2 x_2^2),$$

which is Eq. (A-3).

The desired transformation of Eq. (A-1) can now be performed. First let

$$(\phi_1, \phi_2) \rightarrow (\phi, \phi_1),$$

and integrate over $\phi_1$, which simply gives a factor of $2\pi$. Then let

$$(x_1, x_2, \phi) \rightarrow (p_2, X, \phi),$$

with the result

$$dN = 2\pi n^2 dz \frac{d\sigma}{d\omega_1} \cdot \frac{d\sigma}{d\omega_2} t(z, x_1) J(x_1, x_2, y) \cdot d\phi dp_2 dX,$$ (A-8)

where $J(x_1, x_2, y)$ is the Jacobian of the transformation and is calculated from Eqs. (A-2) and (A-3). This result is related to the differential distribution of n' by

$$d^2\sigma/dp_2 d\Omega = \frac{1}{\ell \pi n} \int_0^\ell \int_0^\pi \frac{dN}{dp_2 dX},$$ (A-9)

where the integrations are over z and $\phi$.

Equation (A-9) is evaluated as a function of $p_2$ and $\Theta$ in the program DBLSCT in the following way. Equations (A-2) and (A-3) are inverted to give two relationships,

$$x_2 = f_1(x_1, \phi, X) \qquad (A-10)$$

and

$$x_2 = f_2(x_1, p_2).$$

The values of X and $p_2$ for which $d^2\sigma/dp_2 d\Omega$ is to be computed are fixed. The integration over $\phi$ is performed by setting $\phi$ and searching for a pair of values of $x_1$ and $x_2$ that simultaneously satisfy both parts of Eq. (A-10). These values are used to calculate $J(x_1, x_2, y)$, $d\sigma(x_1)d\omega_1$, and $d\sigma(x_2, p_1(x_1))/d\omega_2$. The measurements of the charge-exchange angular distributions of Caris et al. [23] were used for $d\sigma_1/d\omega_1$ and the neutron-proton angular distribution data listed in the compilation by Hess [33] were used for $d\sigma_2/d\omega_2$. At this point the integration over z is performed. At each value of z the escape distance $t(x_1, z)$ is computed. In addition the momentum and direction of p' are calculated and the events are classified into four categories. These events in the four categories are:

(a) p' stops in the target,

(b) p' escapes the target and passes through Counter 4 (Fig. 6),

(c) p' escapes the target and passes through Counter 5, and

(d) p' escapes the target and misses Counters 4 and 5.

The value of $\phi$ is increased by a fixed increment and the process is repeated until the integrations are completed. The differential distribution in neutron energy is obtained by the transformation

$$d^2\sigma/dT_{n'} d\Omega = \beta_{n'}^{-1} d^2\sigma/dp_2 d\Omega, \qquad (A-11)$$

where $\beta_{n'}$ is the velocity of n'.

Finally, it should be noted that the tractability of this calculation depends upon applicability to both scatterings of a relationship of the type in Eq. (A-5). This equation is valid for the recoiling target particle in all elastic collisions, and for both particles in elastic collisions

of equal-mass particles. The program DBLSCT can be utilized in any case of double scattering in which both interactions are of either of these two types.

## B. Neutron Detector Efficiency

### 1. Introduction

In scintillator, neutrons are detected by the scintillation light produced by the charged products of interactions between the incident neutrons and the nuclei of the scintillator. One of the main problems involved in the use of a scintillation counter for neutron detection is the determination of its detection efficiency. A computer program to calculate this efficiency in plastic scintillator (composition CH, density 1.05 $g/cm^3$) for neutron energies from 1 MeV to 300 MeV is described here.

For neutron energies below 10 MeV only neutron-hydrogen (np) interactions contribute to the efficiency, and it may be calculated reliably.[34] Above this energy interactions with the carbon nuclei become significant. Although there is considerable information for the np interactions in the energy range under consideration, almost no systematics, other than the total cross section and elastic cross section, are available for neutron-carbon (nC) interactions. The nC reactions that are considered are listed in Table B-I.

Table B-I. Neutron-carbon reactions.

| Reaction | Q (MeV) | Threshold (MeV) |
|---|---|---|
| $C(n, n)C$ | 0 | 0 |
| $C(n, n' \gamma)C_{4.43}$ | -4.43 | 4.7 |
| $C(n, a)Be$ | -5.71 | 6.2 |
| $C(n, n' 3a)$ | -7.26 | 7.9 |
| $C(n, p)B$ | -12.59 | 13.6 |

For detectors that have dimensions of the order of magnitude
of the mean free path for neutron interactions, contributions to the
efficiency from successive scatterings is significant. Rescattering
of the final-state neutrons from np interactions and the (n, n' 3α)
reaction is included in this calculation.

Before the calculation is described, a summary of the cross
section data used is presented.

2. Cross Section Data

Figure B-1 presents the total cross sections for np and nC
interactions as a function of neutron energy. The values below 100
MeV are taken from the compilation by Hughes and Schwartz.[26] Above
100 MeV the existing measurements are indicated.[33,35] Also shown
are the total nC nonelastic cross section and the nC total cross section
minus the elastic scattering inside the first diffraction minimum. This
cross section is used in the calculation and was estimated by using both
nC and pC elastic scattering data, since nC and pC elastic scattering
are essentially identical above 14 MeV incident energy.[36]

Figure B-2 shows the breakdown, according to reaction, of
the nC nonelastic cross section used in the calculation. These values
were arrived at in the following manner. First, the (n, n' γ) cross
section was estimated by using both nC data and pC data above 14 MeV.
This cross section was subtracted from the total nonelastic cross
section. Next the (n, n' 3α) reaction cross section was estimated from
the measurements between 10 and 20 MeV[37] and data at 90 MeV.[38]
The data at 90 MeV were taken in a cloud chamber and indicate a high
multiplicity of reactions that were grouped as two-prong and more-
than-two-prong reactions. The data for more-than-two-prong reactions
were used as the 90-MeV value of the (n, n' 3α) reaction cross section.
At this incident energy the details of the reaction are not critical to
the calculation. The principal information is that all nC nonelastic
interactions produce charged secondaries. This estimate of the
(n, n' 3α) cross section was subtracted and the remaining cross section
was treated as that for (n, α) and (n, p) in a manner suggested by the

MU-28847

Fig. B-1. Neutron cross-section data.
O: np total cross section
⊛: nC total cross section
△: nC total less nC diffraction elastic cross section
▲: nC nonelastic cross section

MU-28848

Fig. B-2. Breakdown of nC nonelastic cross section.
Below 8 MeV all nonelastic taken as (n, n' γ)
A: (n, a) threshold          C: (n, p) threshold
B: (n, n' 3a) threshold      D: (n, d) threshold

O: nonelastic          □: n, n' 3a
▲: n, n' γ             ◉: n, a
△: p, p' γ             ■: Ref. 37, > 3-prong

shape of the curve and the location of the thresholds for these reactions. Actually the C(n, d)B reaction has a threshold at 14.9 MeV, so that the treatment of what will be called the (n, p) reaction includes both. The two-prong category of the 90-MeV data was used as the value of the (n, p) cross section at that energy.

The np angular distribution data used in the computation were from the parameterization by Clements and Winsberg.[39]

3. Efficiency Calculation

The efficiency program TOTEFF calculates for a specified series of neutron energies, E, the total efficiency, $\epsilon(E)$. This quantity is the result of a folding integration over the detection threshold, T, of the type

$$\epsilon(E) = \int_0^\infty dT\, e^{-((T-T_0)/\tau T_0)^2} \epsilon(E, T), \qquad (B-1)$$

where $T_0$ is the mean threshold, $\tau$ is the fractional resolution, and $\epsilon(E, T)$ is the efficiency at energy E and threshold T. This function $\epsilon(E, T)$, is in turn computed in two portions: $\epsilon_H(E, T)$, the efficiency for an initial interaction with hydrogen, and $\epsilon_C(E, T)$, the efficiency for an initial interaction with a carbon nucleus. The essential elements of the program used to compute these quantities are two subroutines. One, HYD(E, T), computes the single-scattering efficiency for np collisions and the other, CARB(E, T), computes the single-scattering efficiency for nC collisions from the (n, a), (n, n' 3a), and (n, p) reactions. Since they contribute only through rescattering, the (n, n) and (n, n' γ) reactions are treated separately.

Multiple-scattering effects are calculated by integrating over the neutrons in the final state of primary reactions that did not produce sufficient light to be detected. This integration involves the successive use of HYD(E', T') and CARB(E', T'), where E' is the scattered neutron energy and T' is the light threshold reduced by the light produced in the primary reaction. This integration involves weighting these efficiencies by the differential distributions of the first reaction and the mean escape distance at the angle of the primary scattering.

The use of an escape distance averaged over the counter geometry is an approximation that is reasonable as long as the dimensions of the counter are not large compared with the mean free path of the incident neutrons. It is necessary to include a subroutine that computes this mean distance for escaping the detector as a function of the angle of scattering.

In terms of particle energy the detection threshold is a function of the type of particle. Because of saturation effects in the scintillation process, heavily ionizing particles are less efficient in producing scintillation light. These saturation effects must be taken into account when considering the light output of the various interactions in the detector. The response of plastic scintillator calculated and measured by Gooding and Pugh[40] is used in this calculation. Their data were parameterized in two ways. First, the light output of a particle as a function of its energy in units of the energy of an electron required to produce the same light output is given by

$$L_p(E_p) = -0.118 + 0.297 E_p + 0.022 E_p^2$$

for protons in the range

$$1 \text{ MeV} \leq E_p \leq 10 \text{ MeV}, \qquad (B-2)$$

and

$$L_\alpha(E_\alpha) = 0.046 E_\alpha + 0.007 E_\alpha^2$$

for alphas in the range

$$0 \leq E_\alpha \leq 25 \text{ MeV}.$$

Second, the inverse relationships that give the particle energy as a function of its light output, T, are

$$E_p(T) = 0.474 + 2.66 T - 0.153 T^2 \qquad (B-3)$$

for protons, and

$$E_\alpha(T) = 2.13 + 6.36\ T - 0.368\ T^2$$

for alphas, both in the range

$$0.2\ \text{MeV} \leq T \leq 5\ \text{MeV}.$$

The details of the calculation of $\epsilon_H(E, T)$ and $\epsilon_C(E, T)$ are presented in the next two sections. Table B-II lists and defines symbols used in these sections. The results of the calculation are presented in a third section.

Table B-II. Symbols used in Appendix B.
(Prime refers to c. m. system)

| | |
|---|---|
| $E$ | = incident neutron energy |
| $T$ | = scintillation light detection threshold in units of equivalent electron energy |
| $\theta, \theta'$ | = angle with respect to the incident neutron direction |
| $X, X'$ | = $\cos \theta, \cos \theta'$ |
| $E_i, E'_i$ | = energy of particle i, |
| $\bar{\beta}$ | = velocity of the center-of-mass system with respect to the laboratory system |
| $\bar{\gamma}$ | = $(1 - \bar{\beta}^2)^{-1/2}$ |
| $p'$ | = momentum (c. m. ) |
| $M_i$ | = rest mass of particle i |
| $\bar{\sigma}$ | = sum of the neutron-proton and neutron-carbon total cross sections |
| $E^*$ | = total energy (c. m. ) |
| $d\sigma_i/d\Omega'$ | = differential cross section as a function of $X'$ |
| $n$ | = number of hydrogen or carbon nuclei per $\text{cm}^3$ in the scintillator |
| $d(\theta)$ | = mean escape distance at angle $\theta$ |
| $Z$ | = distance along the incident neutron direction |
| $W(E, z)$ | = $2\pi\,[\,1 - \exp(-n\,\bar{\sigma}\,(E)z)]\,/\bar{\sigma}\,(E)$ |

## a. Hydrogen interactions

The hydrogen single-scattering efficiency for a length $\ell$ scintillator is given by

$$\epsilon_H^1(E, T) = 2\pi n \int_0^\ell e^{-n\bar{\sigma}(E)Z} F_1(E, T)dZ \qquad \text{(B-4)}$$

$$= W(E, \ell) F_1(E, T),$$

where $F_1(E, T)$ is the portion of the np cross section that produces detectable recoil protons. HYD(E, T) computes $F_1(E, T)$ according to the relation

$$F_1(E, T) = \int_{-1}^{X'_{max}} d\sigma_{np}(E, X')/d\Omega' \, dX', \qquad \text{(B-5)}$$

where $X'_{max}$ is the value of $X'$ such that the recoil proton produces a light output in the scintillator equal to T. In other words,

$$E_p = \bar{\gamma}(E'_p + M_p - \bar{\beta} p' X'_{max}) - M_p = E_p(T),$$

where $E_p(T)$ is given by Eq. (B-3), and $\bar{\gamma}$, $\bar{\beta}$, $E_p'$, and $p'$ are functions of E. Then

$$X'_{max} = (\bar{\gamma}(E_p' + M_p') - (E_p(T) + M_p))/\bar{\beta}\,\bar{\gamma}p' . \qquad \text{(B-6)}$$

Rescattering of the neutrons leaving the primary interaction with hydrogen is included by calculating

$$F_2(E, T) = \int_{X'_{max}}^1 d\sigma_{np}/d\Omega' \, \epsilon^1(X')dX', \qquad \text{(B-7)}$$

where $\epsilon^1(X')$ is the total single-scattering efficiency from hydrogen and carbon for a thickness of scintillator equal to the mean escape distance in a direction $\theta$ corresponding to $X'$, and where

$$\epsilon^1 = \epsilon_H^1\left[E_n(X'), \; T - L_p(E_p(X'))\right] + \epsilon_C^1\left[E_n, \; T - L_p\right], \quad \text{(B-8)}$$

and $\epsilon_H^1$ is given by Eq. (B-4) with $\ell$ replaced by $d(X)$,

$$X = \left[(X' + 1)/2\right]^{1/2},$$

$$E_n(X') = 2M_n \bar{\beta}^2 X^2/(1 - \bar{\beta}^2 X^2),$$

$$E_p(X') = M_p\bar{\beta}^2(1 - X')/(1 - \bar{\beta}^2(1 - X')/2).$$

The quantity $\epsilon_C^1$ is a function for carbon interactions analogous to $\epsilon_H^1$, and is discussed in the next section.

Finally,

$$\epsilon_H(E, T) = W(E, \ell)\left[F_1(E, T) + F_2(E, T)\right]. \quad \text{(B-9)}$$

b.  Carbon interactions

The treatments of the kinematics for the three nC interactions are different.  It is assumed that there is no c.m. angular dependence in any of the reactions.

The (n, $\alpha$) reaction is treated as a two-body reaction.  Be$^{*9}$ excited states are not considered because the assumed cross section has become negligible before energies sufficient to allow much excitation have been reached.  To determine the fraction of (n, $\alpha$) interactions detected it is necessary to use the quantity

$$d\sigma/dE_\alpha = d\sigma/d\Omega' \cdot d\Omega'/dE_\alpha \quad \text{(B-10)}$$

$$= \sigma_T/2\,\bar{\beta}\,\bar{\gamma}\,p'\,.$$

For this reaction, CARB(E, T) computes

$$g_\alpha(E, T) = \int_{E_\alpha^{min}}^{E_\alpha^{max}} dE_\alpha / \bar\beta \, \bar\gamma \, p' = (E_\alpha^{max} - E_\alpha^{min} / \bar\beta \, \bar\gamma \, p' , \quad \text{(B-11)}$$

where

$$E_\alpha^{max} = \bar\gamma \, E_\alpha' + \bar\beta \, \bar\gamma \, p' + M_\alpha (\bar\gamma - 1),$$

and

$$E_\alpha^{min} = E_\alpha(T),$$

where $E_\alpha(T)$ is as defined in Eq. (B-3).

The selection of the method of calculation of the (n, n' 3α) reaction was based on the available experimental data.[37] Although the reaction appears to proceed through intermediate states, the essential features needed here are adequately described by assuming a four-body phase-space distribution of the final-state energies. This permits calculation of the average light produced by the three alphas.

The calculation of the fraction of (n, n' 3α) reactions detected proceeds in two steps. The four-body phase-space distribution is given by[37]

$$N(\delta)d\delta = C\delta^{1/2}(1 - \delta)^2 \, d\delta, \quad \text{(B-12)}$$

where $\delta$ is the ratio of the kinetic energy of any particle to its maximum possible kinetic energy, in the overall c.m. system. The excitation energy of the recoiling carbon nucleus available to the three alphas, $Q(E, \delta_n)$, is derived from

$$\delta_n = \frac{E_n'}{E_{n\,max}'} = \frac{(E^* - M_n)^2 - (M_C 12 + 7.26 + Q)^2}{(E^* - M_n)^2 - (M_C 12 + 7.26)^2}, \quad \text{(B-13)}$$

where $E^*$ is a function of E, or

$$Q = -(M_C 12 + 7.26) + \left[ \delta_n (M_C 12 + 7.26)^2 + (1 - \delta_n)(E^* - M_n) \right]^{1/2}.$$

Using Eq. (B-2), one finds the light produced by the three alphas:

$$L_{3\alpha} = 0.046 \sum_{i=1}^{3} E_{\alpha i} + 0.007 \sum_{i=1}^{3} (E_{\alpha i}^{2}) \qquad \text{(B-14)}$$

$$= 0.046 \, Q + 0.007 \sum_{i} (E_{\alpha i}^{2}).$$

For a phase-space distribution of the $E_{\alpha i}$' s, the average fraction of events detected for threshold T is

$$f_{3\alpha}(Q, T) = 3 \, [\, 1 - 2/0.007Q \, (T/Q - 0.046)] \qquad \text{(B-15)}$$

with the additional restriction that for $f_{3\alpha}(Q, T) \leq 0$, $f_{3\alpha}(Q, T) = 0$, and for $f_{3\alpha}(Q, T) \geq 1$, $f_{3\alpha}(Q, T) = 1$.

For the (n, n' 3α) reaction, CARB(E, T) computes the average total fraction detected,

$$g_{3\alpha}(E, T) = \int_{0}^{1} d\delta_{n} \, N(\delta_{n}) f_{3\alpha} \, [\, Q(\delta_{n}), T]. \qquad \text{(B-16)}$$

The (n, p) reaction was not considered as a two-body reaction. The $B^{12}$ system has a high density of low-lying excited states[41] and the interaction must be of a direct charge-exchange type rather than optical in nature. In the absence of any data the final-state proton was assumed to have the same energy distribution as the neutron in the (n, n' 3α) case. A distribution calculated on the basis of a direct-interaction model might be more accurate, but the added sophistication was not deemed appropriate here in consideration of the speculative nature of the estimate of the (n, p) reaction cross section. The calculation is similar to the (n, α) reaction treatment except that the variable excitation energy of the $B^{*12}$ must be considered. The detected fraction is calculated by integrating the differential distribution in energy and angle,

$$f_p(E, T, \delta_p) = 2\pi \int_{-1}^{X'_{p\,max}} d^2\sigma/d\delta_p d\Omega' \, d\delta_p dX'$$

$$= C \, \delta_p^{1/2}(1-\delta_p)^2 \, (X'_{p\,max} + 1), \qquad \text{(B-17)}$$

where $X'_{max}(E, T, \delta_p)$ is determined by

$$X'_{p\,max} = \frac{M_p + E_p(T) - \bar{\gamma}(\delta_p E'_{p\,max} + M_p)}{\bar{\beta}\,\bar{\gamma}(\delta_p E'_{p\,max}(\delta_p E'_{p\,max} + 2M_p))^{1/2}}, \qquad \text{(B-18)}$$

with the restriction

$$-1 \leqslant X'_{p\,max} \leqslant 1.$$

CARB(E, T) calculates the total fraction of (n, p) reactions detected:

$$g_p(E, T) = \int_0^1 d\,\delta_p \, f_p \, (E, T, \delta_p). \qquad \text{(B-19)}$$

The single-scattering efficiency for nC interactions is given by

$$\epsilon_C^1 \, (E, T) = W(E, \ell) G_1(E, T), \qquad \text{(B-20)}$$

where

$$G_1(E, T) = \sum_k \sigma_k(E) \, g_k(E, T),$$

with the summation performed over the three reactions.

The efficiency derived from the rescattering of the final-state neutrons in (n, n' 3α) reactions is calculated according to the expression

$$G_2(E, T) = \int_0^1 d\delta_n N(\delta_n) \int_0^1 dX' \; \epsilon^1(X', \delta_n), \qquad (B-21)$$

where $\epsilon^1(X', \delta_n)$ is the single-scattering efficiency for np and nC interactions at the energy of the scattered neutron in the average escape distance in the laboratory system corresponding to $X'$. Explicitly,

$$\epsilon^1(X', \delta_n) = W(E_n, d(X')) \, [\, F_1(E_n, T') + G_1(E_n, T') \,], \qquad (B-22)$$

where

$$E_n(E, \delta_n, X')$$

$$= \bar{\gamma}(\delta_n E'_{n\,max} + M_n) + \bar{\beta}\,\bar{\gamma}\,(\delta_n E'_{n\,max} + 2M_n))^{1/2} - M_n,$$

and $T'$ is the threshold adjusted for the average amount of light produced by the three alphas in the primary $(n, n'\,3\alpha)$ reaction. The alpha light is a function of $Q$, which is in turn a function of $\delta_n$ (Eq. B-13). The rescattering calculation is divided into three categories. For

$$T \leqslant L_{3\alpha}\,min = 0.046\,Q + 0.007/3\,Q^2, \qquad (B-23)$$

all first scatterings are detected and no rescattering effects are present. For

$$T \geqslant L_{3\alpha}\,max = 0.046\,Q + 0.007/2\,Q^2, \qquad (B-24)$$

no first scatterings are detected and the average threshold for the rescattering calculation is

$$T' = T - (0.046\,Q + 0.035\,Q^2/12).$$

Finally, for

$$L_{3a_{max}} \geq T \geq L_{3a_{min}} \, ,$$

(B-25)

$$T' = [T - (0.046 \, Q + 0.007 \, Q^2/3)]/2.$$

The total efficiency derived from inelastic nC reactions with charged products is

$$\epsilon_C(E, T) = W(E, \ell) [G_1(E, T) + G_2(E, T)] \, .$$

(B-26)

The calculation of the contributions to the detection efficiency of the rescattering effects in (n, n) and (n,n' $\gamma$) reactions is not performed by the program. At neutron energies greater than 20 MeV the extreme forward peaking of the (n, n) angular distribution allows a great simplification in the treatment. Since the energy and direction of the scattered neutron differ from those of the incident neutron by small amounts, it is reasonable to neglect this contribution to the nC total cross section used in the evaluation of $\bar{\sigma}(E)$ in the expressions above. In order to estimate the contribution below 20 MeV a hand calculation was performed at 14 MeV based on the data available for $d\sigma(n, n)/d\Omega$. [36] The contribution is given by the expression

$$\epsilon_{e\ell} = W(E, \ell) \int_{-1}^{1} dX \, \frac{d\sigma_{(n, n)}}{d\Omega} \, \epsilon[E_n(X), T] \, \frac{d(X)}{\ell} \, ,$$

(B-27)

where $\epsilon[E_n(X), T]$ is the total efficiency computed by the program.

Both the final-state neutron and the gamma may be detected in the (n,n' $\gamma$) reaction. The detection of the 4.43-MeV gamma is principally by Compton scattering. The angular distributions of both the gamma and the neutron have been measured at 14 MeV. [36] The gamma efficiency is given by

$$\epsilon_\gamma = W(E, \ell) \, f(t) \, \rho \, \mu_{eff} \int_{-1}^{1} dX \, \frac{d\sigma_{(n, n' \gamma)}}{d\Omega} \, d(X), \qquad (B-28)$$

where

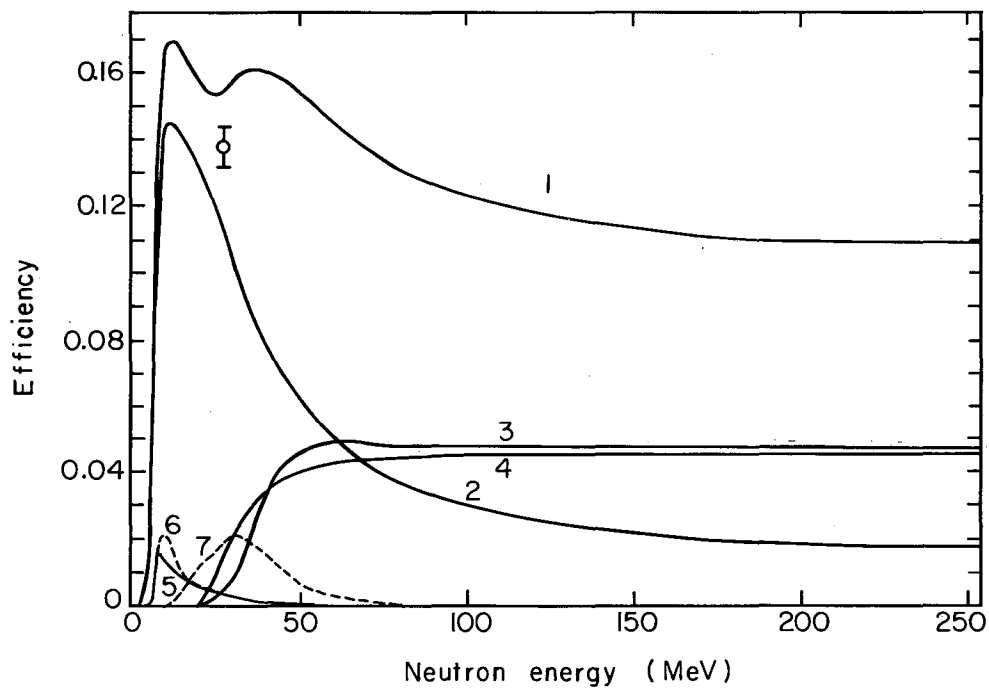$$\mu_{eff} = 7 \, \mu_{Comp}^{H}/13 \, ,$$

and $\mu_{Comp}^{H}$ is the total Compton attenuation coefficient for hydrogen,[42]
f(t) is the fraction of the Compton electron spectrum of the 4.43-MeV
gamma above T, and $\rho$ is the density of the scintillator. Here $\epsilon_\gamma$
as a function E was calculated by assuming the gamma angular
distribution was independent of energy and normalizing to the total
cross section as a function of energy. The contribution of the final-
state neutron was calculated by using Eq. (B-27) with $d\sigma^{n'}(n, n' \gamma)/d\Omega$
substituted for $d\sigma(n, n)/d\Omega$.

c. Results and discussion

The results of the calculation of the detection efficiency of the
counters used in this experiment are shown in Fig. B-3. The thresh-
old was 2.3 MeV with a 30% resolution. The detector geometry was
approximated as a right cylinder with the axis along the incident-
neutron direction. The average escape distance was computed for
uniform neutron illumination of the cross-sectional area by a separate
program. The results of this program were fitted with a power series
in $\cos\theta$. This power series was used as the basis for the required
subroutine in the main program. The contributions of the individual
processes are also indicated in Fig. B-3.

The maximum uncertainty exists in the region in which the
efficiency due to the (n, n' 3$\alpha$) and (n, p) reactions rises from zero to
maximum, i.e., 20 to 75 MeV. At 90 MeV the measurements by
Kellogg indicate that essentially all the nonelastic nC interactions
produce charged particles with sufficient light production to exceed
the 2.3-MeV threshold.[38]
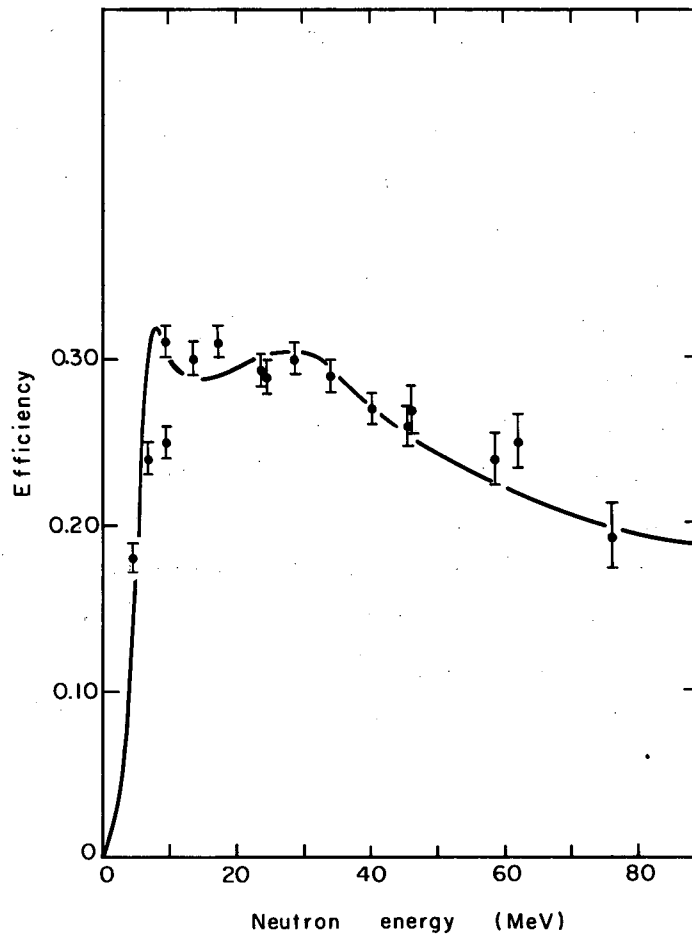
MU-28849

Fig. B-3. Neutron detection efficiency.
10.16 cm thick, 9.0 cm radius, cylindrical plastic
scintillator 2.3±.7 MeV threshold (equivalent electron
energy)
1: total efficiency
2: np scattering contribution
3: (n, n' 3α) contribution
4: (n, p) contribution
5: (n, n' γ) contribution
6: np rescattering contribution
7: n, n' 3α rescattering contribution
O: data from reference 44.

The efficiency of a similar type of neutron counter has been measured in the energy region 4 to 76 MeV.[43] The program computations and hand calculations described here were performed for this counter. The threshold was taken to be 1.1 MeV with a 50% resolution, and the geometry approximated by a 15-cm thick cylinder with 10-cm radius. The results of the calculation and the measured points are shown in Fig. B-4. A measurement at 27 MeV neutron energy of the efficiency of a neutron detector with all parameters equal to those of the detectors used in this experiment[44] is shown in Fig. B-3. This measurement was not corrected for rescattering and absorption losses in the target that served as the neutron source, and therefore would be expected to be slightly low in comparison with the calculated value.

The uncertainty in the calculated value of the efficiency was estimated to be ± 10%. This number was selected because it is the order of uncertainty in the total nonelastic nC cross section. The application of a $\chi^2$ test of statistical significance[22] to the comparison with the measurements by Wiegand et al.[43] yielded a result of $\chi^2$/(degrees of freedom) ≈ 1, indicating the calculation to be compatible with the uncertainty quoted for the measured efficiency.

Fig. B-4. Comparison of calculation with efficiency measured by Wiegand et al. (reference 43).

MU-28850

## C.   Gamma Conversion

In order to compute the probability that a gamma, produced in the decay of a neutral pion, would interact in the target or surrounding counters (Fig. 6) and produce a charged secondary, it is necessary to know the differential distribution of the gammas as a function of gamma energy and direction in the laboratory system. This distribution is derived by Squire[45] for a neutral pion with energy $T'$ and angular distribution,

$$d\sigma/d\Omega' = \sum_n a_n P_n(x'),$$

in the c.m. system, and is

$$\frac{d^2\sigma}{dkd\Omega} = \frac{2}{\beta'\gamma'\mu\gamma(1-\beta x)} \sum_n a_n P_n\left[\frac{x-\beta}{1-\beta x}\right] P_n\left[\frac{1}{\beta'}\left(1 - \frac{\mu}{2\gamma\gamma' k(1-\beta x)}\right)\right], \quad (C-1)$$

where

$\mu = \pi^0$ rest mass,

$\beta' =$ c.m. $\pi^0$ velocity,

$\gamma' = (1 - \beta'^2)^{-1/2}$,

$\beta =$ velocity of the c.m. system,

$x' =$ cosine of $\pi^0$ c.m. angle,

$x =$ cosine of gamma lab angle,

$d\Omega =$ observer's solid angle (lab).

For a fixed incident pion energy, $\beta'$ and $\gamma'$ of a charge-exchange $\pi^0$ are constant,

$$\gamma' = (E^{*2} + \mu^2 - M^2)/2E^*\mu, \qquad (C-2)$$

where

$E^* = $ c. m. total energy,

$M$ = nucleon mass.

For a given set of $a_n$'s, the program GAMCON calculates the distribution of gammas resulting from charge-exchange $\pi^0$ decays, $d^2\sigma_{cx}/dkd\Omega$, for specified values of x, between the limits of k obtained by setting the argument of the second Legendre polynomial in Eq. (C-1) equal to + 1 or - 1. The data of Caris et al.[23] at 371 MeV incident pion energy were used for the $\pi^0$ c. m. angular distribution in this calculation.

The $\beta'$ and $\gamma'$ of neutral pions in inelastic reactions are not constant. Before the resultant gamma distribution can be calculated, the distribution of $\gamma'$ must be specified. The angular distribution of the inelastic pions is assumed to be isotropic in the c. m. system, and the energy distribution is assumed to be given by the invariant three-body phase-space distribution,

$$\frac{d\rho}{d\gamma'} = 8\pi^2 \left\{ (\gamma'^2 - 1) \left[ 1 + \frac{(M^2 - \mu^2)^2}{(E^{*2} - 2E^*\gamma'\mu + \mu^2)^2} - \frac{2(M^2 + \mu^2)}{(E^{*2} - 2E^*\gamma'\mu + \mu^2)} \right] \right\}^{1/2}.$$

$$(C-3)$$

GAMCON computes the gamma distribution resulting from inelastic $\pi^0$ decay by use of

$$\frac{d^2\sigma_{in}}{dkd\Omega} = \int_1^{\gamma'_{max}} d\gamma' \, \frac{d\rho}{d\gamma'} \cdot \frac{d^2\sigma}{dkd\Omega} \, , \qquad (C-4)$$

where

$$\gamma'_{max} = [E^{*2} + \mu^2 - (M + \mu)^2]/2E^*\mu,$$

and $d^2\sigma/dkd\Omega$ is given by Eq. (C-1). This result is normalized to unit total cross section.

The probability of the production of a Compton electron or an electron-positron pair by a gamma in a thickness $z(g/cm^2)$ of material is

$$\epsilon(k) = 1 - e^{-z\mu(k)}, \qquad (C-5)$$

where $\mu(k)$ is the mass attenuation coefficient of the material at gamma energy $k$. [46] In order to calculate the probability of gamma conversions in which a charged product is detected in Counter 4 or 5 (Fig. 6), the argument of the exponential in Eq. (C-5) is replaced by a sum over the various materials encountered in escaping the target. One-half the thickness of Counters 4 and 5 is included as converting material. The thicknesses of the converting materials are functions of the direction of escape.

Finally, GAMCON calculates, as a function of the direction x, the probability averaged over gamma energy of conversion of gammas resulting from charge-exchange and inelastic $\pi^0$ decays according to

$$\epsilon(x) = 1 - \frac{\int dk \, \frac{d^2\sigma}{dkd\Omega} \exp\left[-\sum_i \mu_i(k)z_i(x)\right]}{\int dk \, \frac{d^2\sigma}{dkd\Omega}}, \qquad (C-6)$$

where the summation is over the various materials surrounding the target in the direction x. Figure C-1 shows $\epsilon(x)$ and $dk \, \frac{d^2\sigma}{dkd\Omega}$ for the charge-exchange and inelastic $\pi^0$ decay gammas at 374 MeV incident $\pi^-$ energy as a function of x.
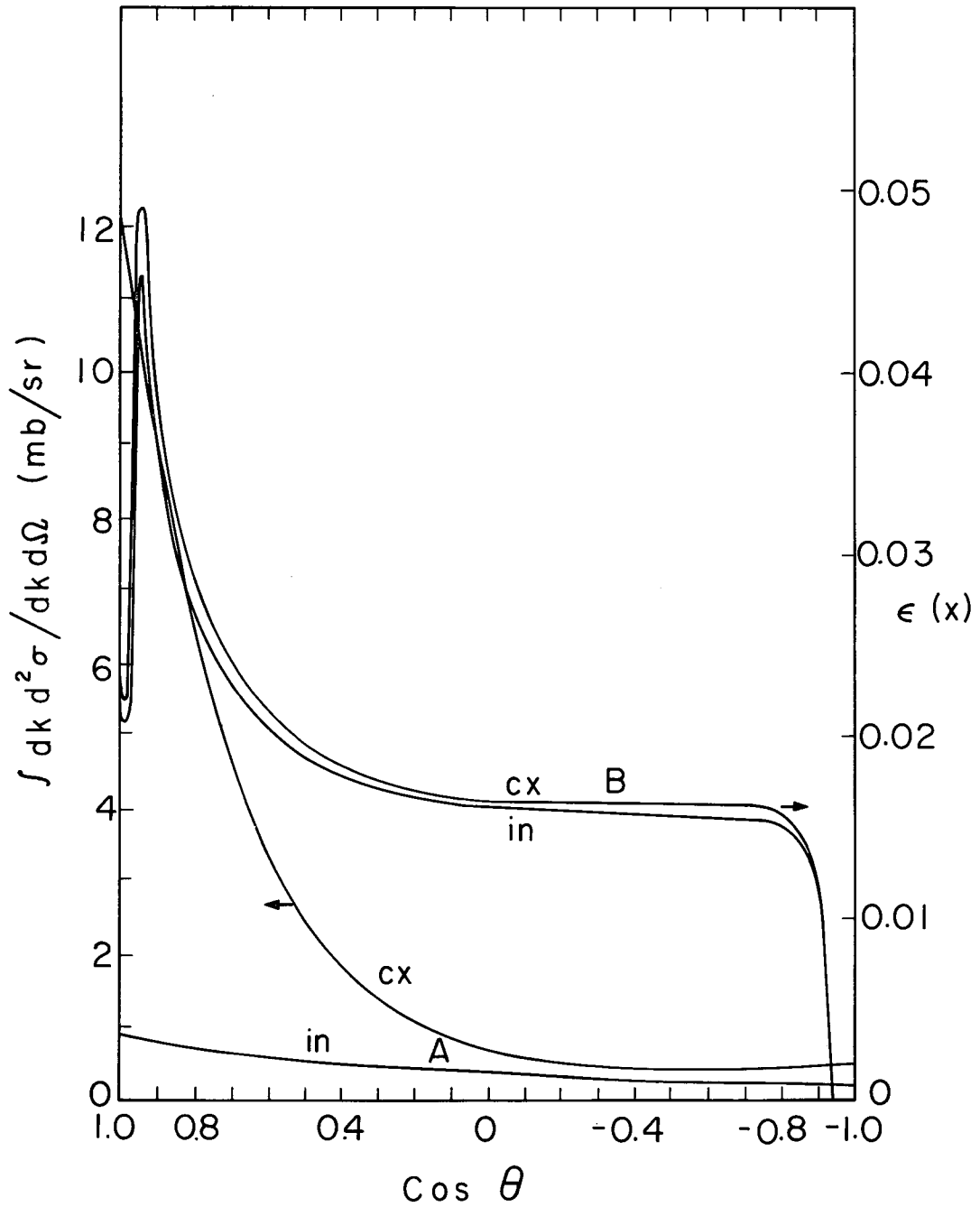
The total conversion probability for each type of gamma is divided into two classes according to whether charged secondaries are detected in Counter 4 or Counter 5. These probabilities are given by

$$\epsilon_4 = \int_{x_4}^{1} dx \, \epsilon(x)$$

and

$$\epsilon_5 = \int_{x_5}^{x_4} dx \, \epsilon(x), \qquad (C-7)$$

where $x_4$ is the cosine of the maximum angle subtended by Counter 4 and $x_5$ is the cosine of the maximum angle subtended by Counter 5.

Fig. C-1. Gamma conversion, 374 MeV.
cx: charge-exchange $\pi^0$, $\sigma_{cx}$ = 13.6 mb
in: inelastic $\pi^0$, $\sigma_{in}$ = 1.4 mb

A: Energy-integrated angular distribution.
B: Energy-averaged conversion probability.

MUB-1490

## D. Differential Distribution Data

On the following pages are photographic records of results as displayed on the IBM 7090 cathode-ray tube (presented in the order listed in Table IV).

INCIDENT PION ENERGY = 374 MEV
THETA = 10.0 DEG     FLIGHT PATH = 1.4 METERS
CHARGE EXCHANGE ENERGY = 237.9 MEV
INELASTIC KINEMATIC LIMIT = 189.0 MEV



INCIDENT PION ENERGY = 374 MEV
THETA = 10.0 DEG     FLIGHT PATH = 1.4 METERS
CHARGE EXCHANGE ENERGY = 237.9 MEV
INELASTIC KINEMATIC LIMIT = 193.4 MEV

DIFFERENTIAL CROSS SECTION (MICROBARNS/MEV-SR)

NEUTRON KINETIC ENERGY (MEV)

+ - N FINAL STATE

INCIDENT PION ENERGY = 374 MEV
THETA = 10.0 DEG        FLIGHT PATH = 2.0 METERS
CHARGE EXCHANGE ENERGY = 237.9 MEV
INELASTIC KINEMATIC LIMIT = 189.0 MEV



DIFFERENTIAL CROSS SECTION (MICROBARNS/MEV-SR)

NEUTRON KINETIC ENERGY (MEV)

O O N FINAL STATE

INCIDENT PION ENERGY = 374 MEV
THETA = 10.0 DEG        FLIGHT PATH = 2.0 METERS
CHARGE EXCHANGE ENERGY = 237.9 MEV
INELASTIC KINEMATIC LIMIT = 193.4 MEV

DIFFERENTIAL CROSS SECTION (MICROGRAMS/MEV-SR)

• — N FINAL STATE

NEUTRON KINETIC ENERGY (MEV)

INCIDENT PION ENERGY = 374 MEV
THETA = 20.0 DEG        FLIGHT PATH = 1.4 METERS
CHARGE EXCHANGE ENERGY = 214.2 MEV
INELASTIC KINEMATIC LIMIT = 165.5 MEV



DIFFERENTIAL CROSS SECTION (MICROGRAMS/MEV-SR)

O O N FINAL STATE

NEUTRON KINETIC ENERGY (MEV)

INCIDENT PION ENERGY = 374 MEV
THETA = 20.0 DEG        FLIGHT PATH = 1.4 METERS
CHARGE EXCHANGE ENERGY = 214.2 MEV
INELASTIC KINEMATIC LIMIT = 169.9 MEV

INCIDENT PION ENERGY = 374 MEV
THETA = 20.0 DEG        FLIGHT PATH = 2.0 METERS
CHARGE EXCHANGE ENERGY = 214.2 MEV
INELASTIC KINEMATIC LIMIT = 166.5 MEV



INCIDENT PION ENERGY = 374 MEV
THETA = 20.0 DEG        FLIGHT PATH = 2.0 METERS
CHARGE EXCHANGE ENERGY = 214.2 MEV
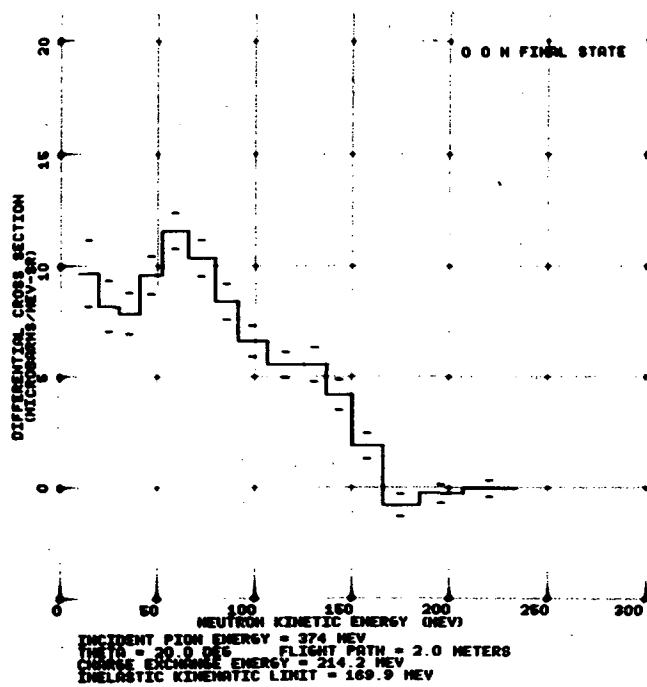INELASTIC KINEMATIC LIMIT = 169.9 MEV

INCIDENT PION ENERGY = 374 MEV
THETA = 30.0 DEG    FLIGHT PATH = 1.4 METERS
CHARGE EXCHANGE ENERGY = 178.9 MEV
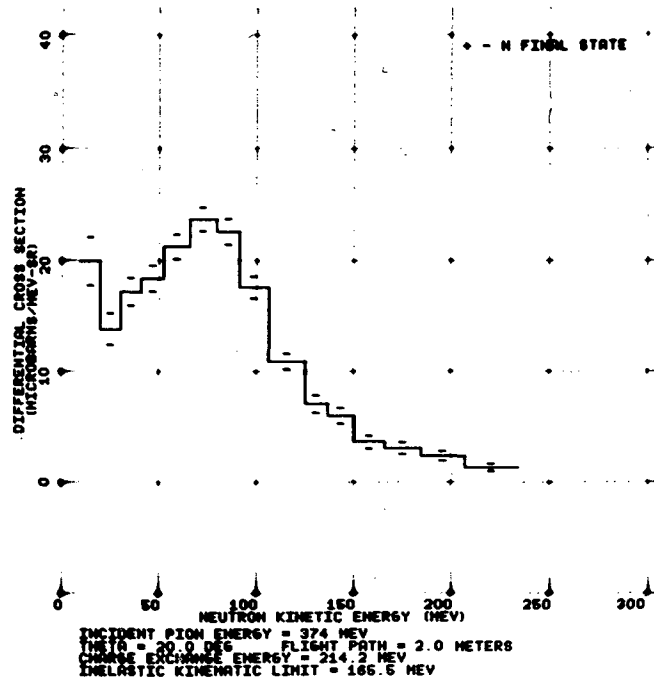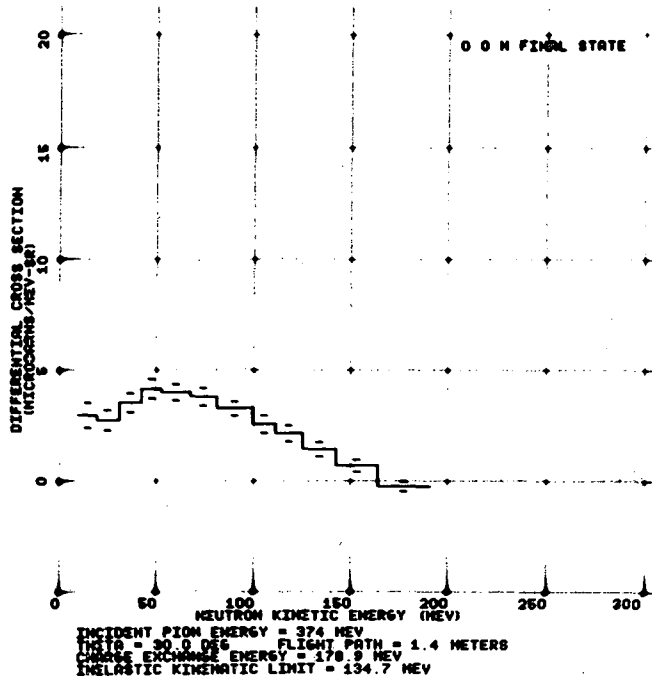INELASTIC KINEMATIC LIMIT = 130.2 MEV



INCIDENT PION ENERGY = 374 MEV
THETA = 30.0 DEG    FLIGHT PATH = 1.4 METERS
CHARGE EXCHANGE ENERGY = 178.9 MEV
INELASTIC KINEMATIC LIMIT = 134.7 MEV

DIFFERENTIAL CROSS SECTION (MICROGRAMS/MEV-SR)
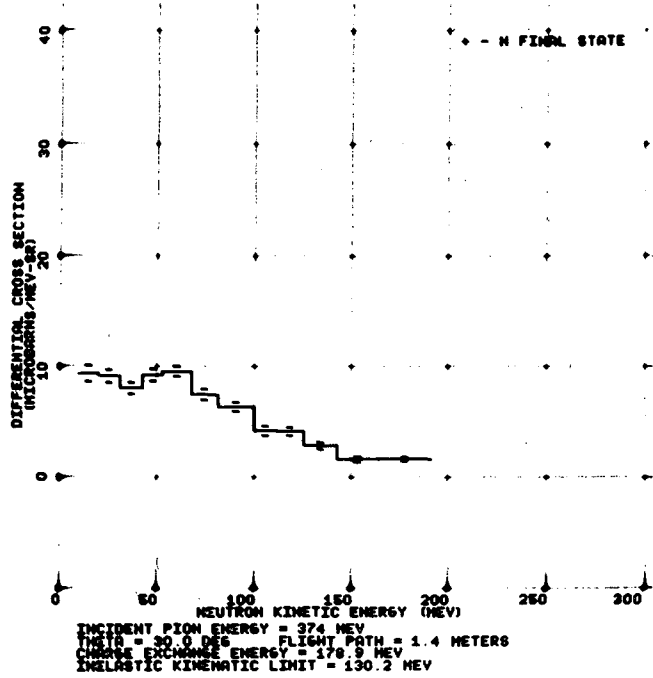
NEUTRON KINETIC ENERGY (MEV)

INCIDENT PION ENERGY = 374 MEV
THETA = 30.0 DEG        FLIGHT PATH = 2.0 METERS
CHARGE EXCHANGE ENERGY = 178.9 MEV
INELASTIC KINEMATIC LIMIT = 130.2 MEV



DIFFERENTIAL CROSS SECTION (MICROGRAMS/MEV-SR)

NEUTRON KINETIC ENERGY (MEV)

INCIDENT PION ENERGY = 374 MEV
THETA = 30.0 DEG        FLIGHT PATH = 2.0 METERS
CHARGE EXCHANGE ENERGY = 178.9 MEV
INELASTIC KINEMATIC LIMIT = 134.7 MEV

N FINAL STATE

DIFFERENTIAL CROSS SECTION
(MICROGRAMS/MEV-SR)

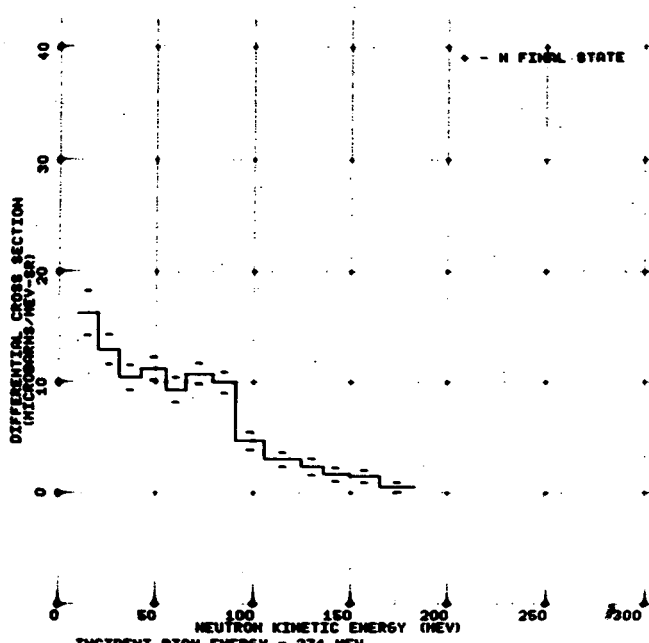NEUTRON KINETIC ENERGY (MEV)

INCIDENT PION ENERGY = 374 MEV
THETA = 35.0 DEG     FLIGHT PATH = 1.4 METERS
CHARGE EXCHANGE ENERGY = 150.4 MEV
INELASTIC KINEMATIC LIMIT = 109.6 MEV



O O N FINAL STATE

DIFFERENTIAL CROSS SECTION
(MICROGRAMS/MEV-SR)

NEUTRON KINETIC ENERGY (MEV)

INCIDENT PION ENERGY = 374 MEV
THETA = 35.0 DEG     FLIGHT PATH = 1.4 METERS
CHARGE EXCHANGE ENERGY = 150.4 MEV
INELASTIC KINEMATIC LIMIT = 114.2 MEV

N FINAL STATE

DIFFERENTIAL CROSS SECTION
(MICROBARNS/MEV-SR)

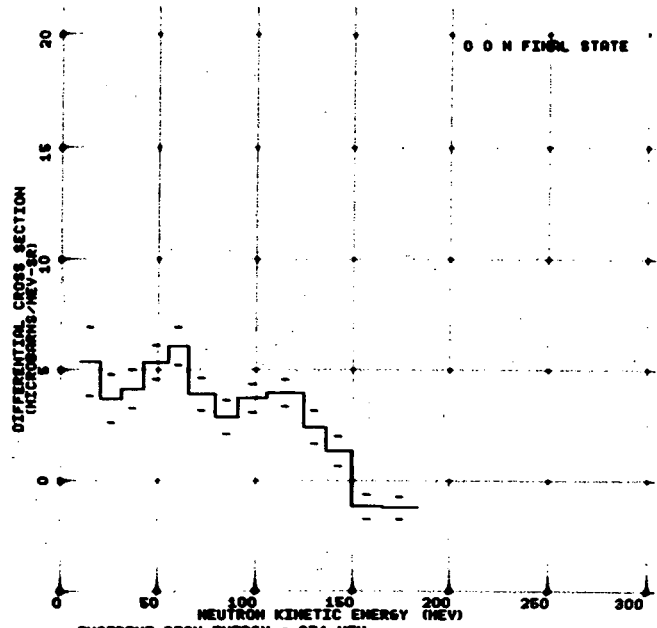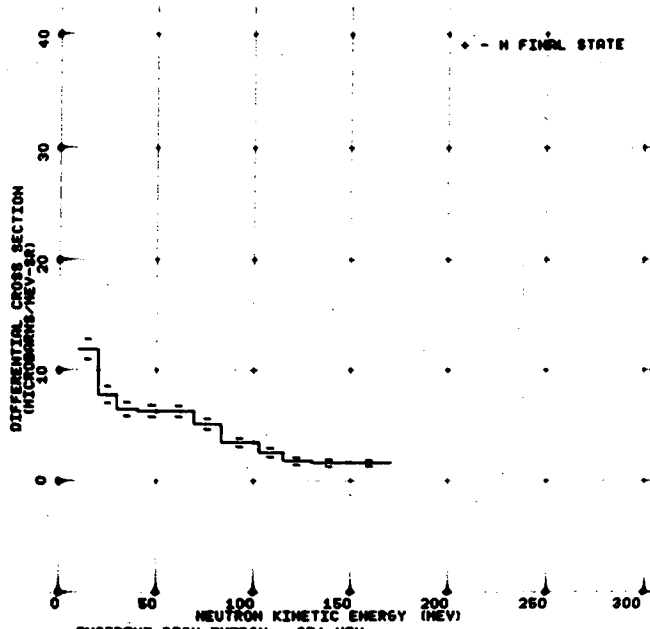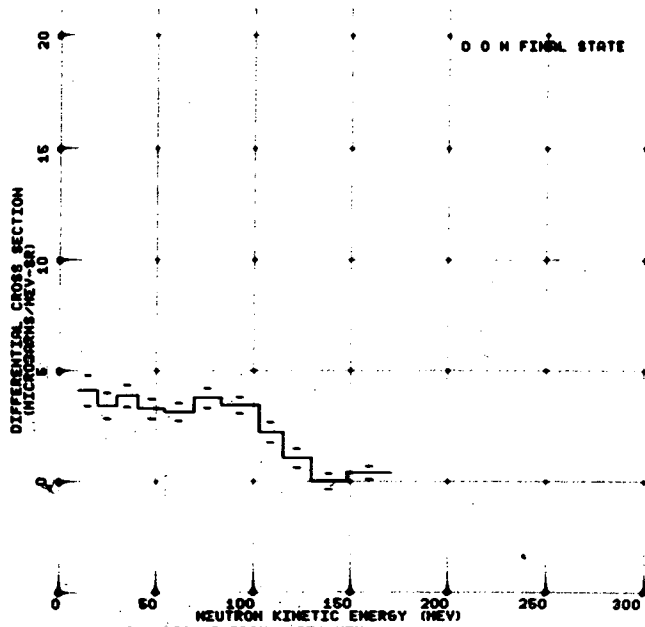NEUTRON KINETIC ENERGY (MEV)

INCIDENT PION ENERGY = 374 MEV
THETA = 35.0 DEG       FLIGHT PATH = 2.0 METERS
CHARGE EXCHANGE ENERGY = 160.4 MEV
INELASTIC KINEMATIC LIMIT = 109.6 MEV



O O N FINAL STATE

DIFFERENTIAL CROSS SECTION
(MICROBARNS/MEV-SR)

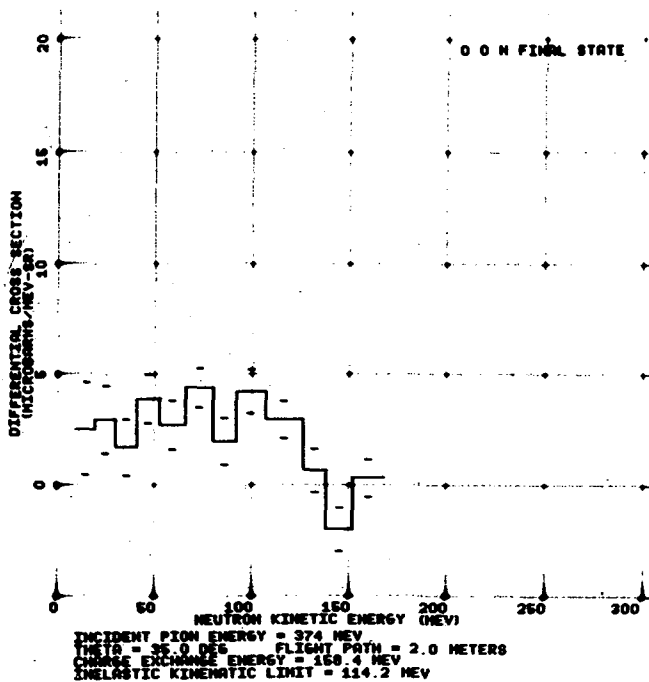NEUTRON KINETIC ENERGY (MEV)

INCIDENT PION ENERGY = 374 MEV
THETA = 35.0 DEG       FLIGHT PATH = 2.0 METERS
CHARGE EXCHANGE ENERGY = 160.4 MEV
INELASTIC KINEMATIC LIMIT = 114.2 MEV

DIFFERENTIAL CROSS SECTION (MICROGRAMS/MEV-SR)
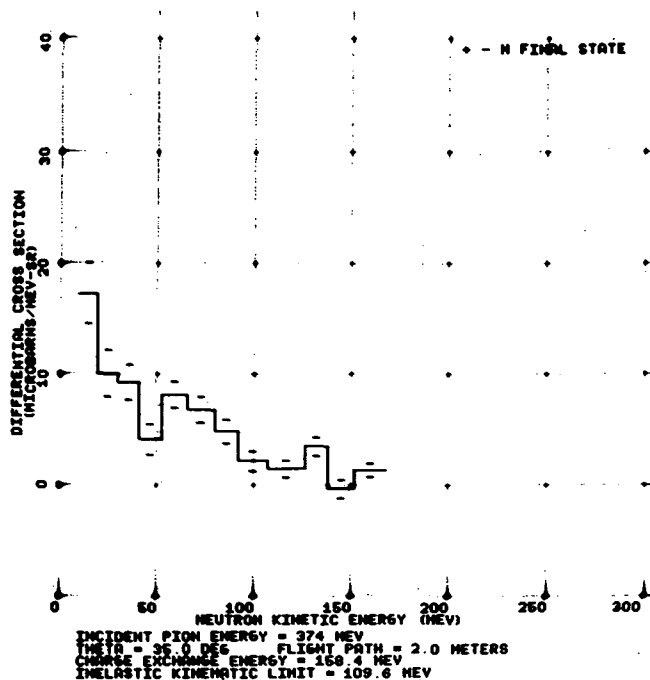
NEUTRON KINETIC ENERGY (MEV)

INCIDENT PION ENERGY = 374 MEV
THETA = 40.0 DEG      FLIGHT PATH = 1.4 METERS
CHARGE EXCHANGE ENERGY = 137.1 MEV
INELASTIC KINEMATIC LIMIT =  87.7 MEV



DIFFERENTIAL CROSS SECTION (MICROGRAMS/MEV-SR)
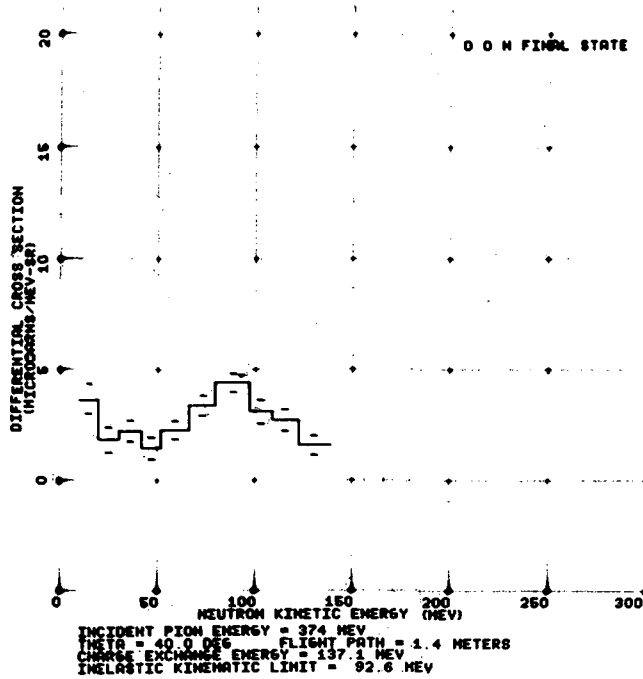
NEUTRON KINETIC ENERGY (MEV)

INCIDENT PION ENERGY = 374 MEV
THETA = 40.0 DEG      FLIGHT PATH = 1.4 METERS
CHARGE EXCHANGE ENERGY = 137.1 MEV
INELASTIC KINEMATIC LIMIT =  92.6 MEV

DIFFERENTIAL CROSS SECTION
(MICROBARNS/MEV-SR)

◆ - N FINAL STATE

NEUTRON KINETIC ENERGY (MEV)

INCIDENT PION ENERGY = 374 MEV
THETA = 40.0 DEG        FLIGHT PATH = 2.0 METERS
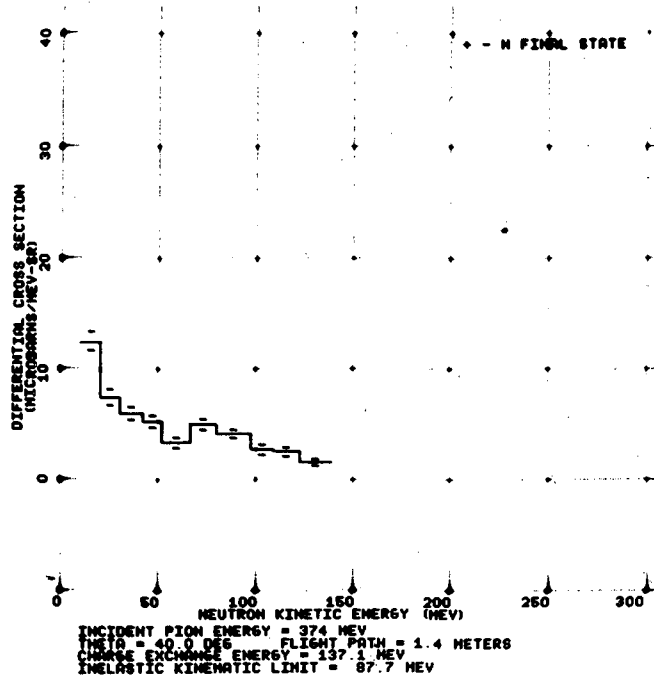CHARGE EXCHANGE ENERGY = 137.1 MEV
INELASTIC KINEMATIC LIMIT =  87.7 MEV



DIFFERENTIAL CROSS SECTION
(MICROBARNS/MEV-SR)

0 0 N FINAL STATE

NEUTRON KINETIC ENERGY (MEV)

INCIDENT PION ENERGY = 374 MEV
THETA = 40.0 DEG        FLIGHT PATH = 2.0 METERS
CHARGE EXCHANGE ENERGY = 137.1 MEV
INELASTIC KINEMATIC LIMIT =  92.6 MEV
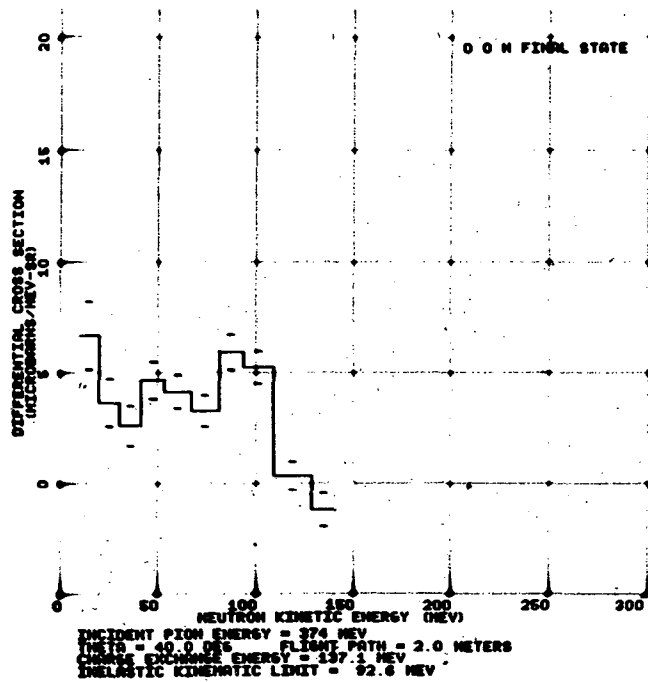
INCIDENT PION ENERGY = 374 MEV
THETA = 45.0 DEG        FLIGHT PATH = 1.4 METERS
CHARGE EXCHANGE ENERGY = 116.6 MEV
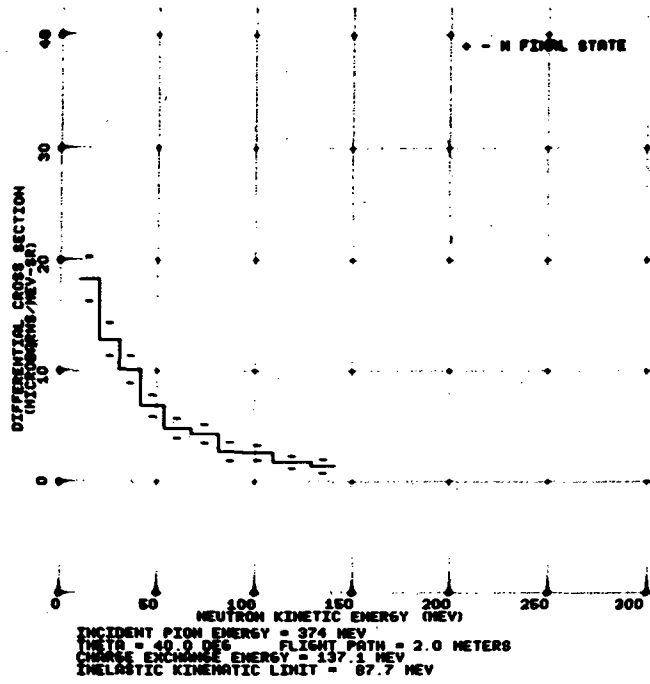INELASTIC KINEMATIC LIMIT = 64.9 MEV



INCIDENT PION ENERGY = 374 MEV
THETA = 45.0 DEG        FLIGHT PATH = 1.4 METERS
CHARGE EXCHANGE ENERGY = 116.6 MEV
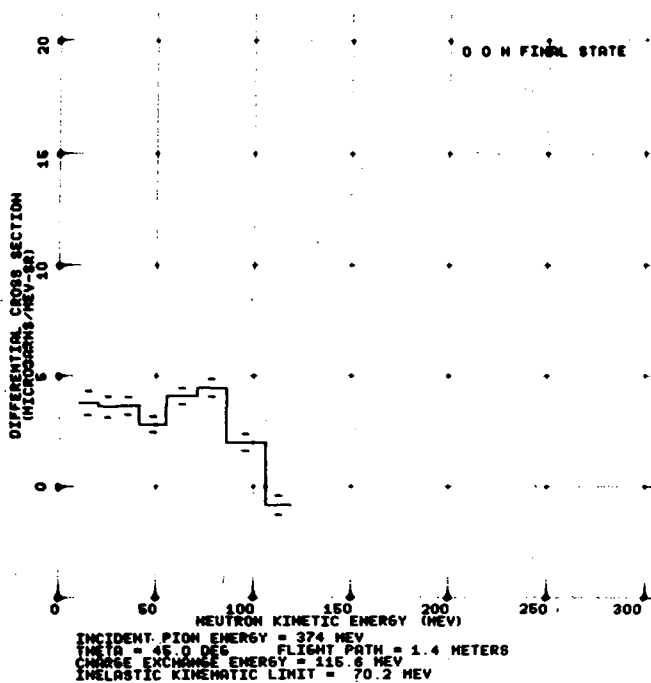INELASTIC KINEMATIC LIMIT = 70.2 MEV

INCIDENT PION ENERGY = 374 MEV
THETA = 45.0 DEG     FLIGHT PATH = 2.0 METERS
CHARGE EXCHANGE ENERGY = 116.6 MEV
INELASTIC KINEMATIC LIMIT =  64.9 MEV



INCIDENT PION ENERGY = 374 MEV
THETA = 45.0 DEG     FLIGHT PATH = 2.0 METERS
CHARGE EXCHANGE ENERGY = 116.6 MEV
INELASTIC KINEMATIC LIMIT =  70.2 MEV

INCIDENT PION ENERGY = 374 MEV
THETA = 50.0 DEG     FLIGHT PATH = 1.4 METERS
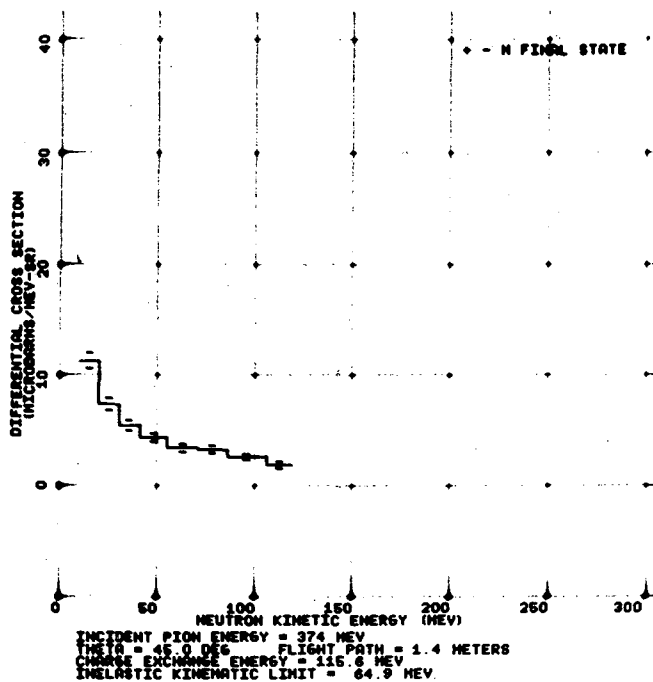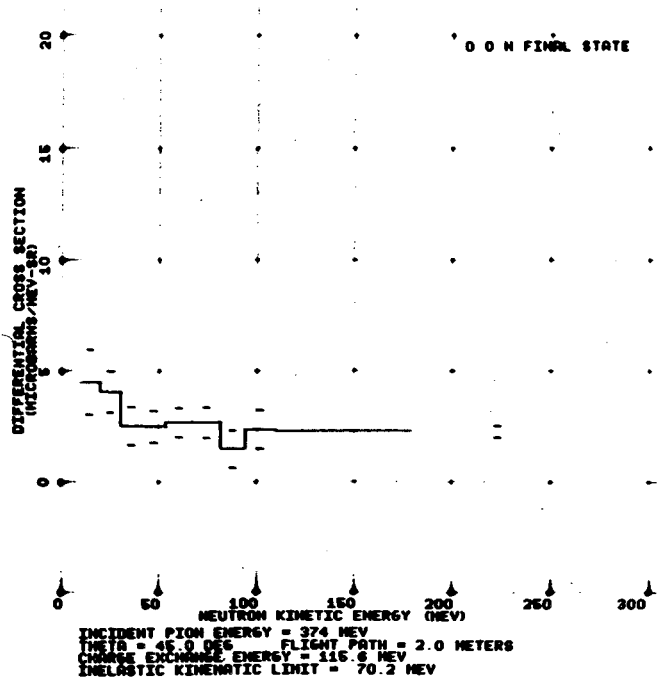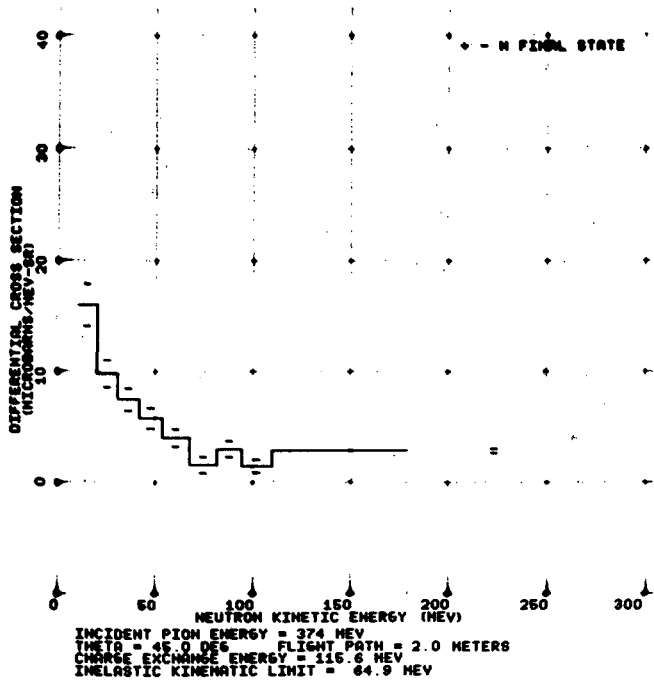CHARGE EXCHANGE ENERGY = 94.5 MEV
INELASTIC KINEMATIC LIMIT = 40.1 MEV



INCIDENT PION ENERGY = 374 MEV
THETA = 50.0 DEG     FLIGHT PATH = 1.4 METERS
CHARGE EXCHANGE ENERGY = 94.5 MEV
INELASTIC KINEMATIC LIMIT = 47.0 MEV

N FINAL STATE

DIFFERENTIAL CROSS SECTION
(MICROBARNS/MEV-SR)

NEUTRON KINETIC ENERGY (MEV)

INCIDENT PION ENERGY = 374 MEV
THETA = 50.0 DEG     FLIGHT PATH = 2.0 METERS
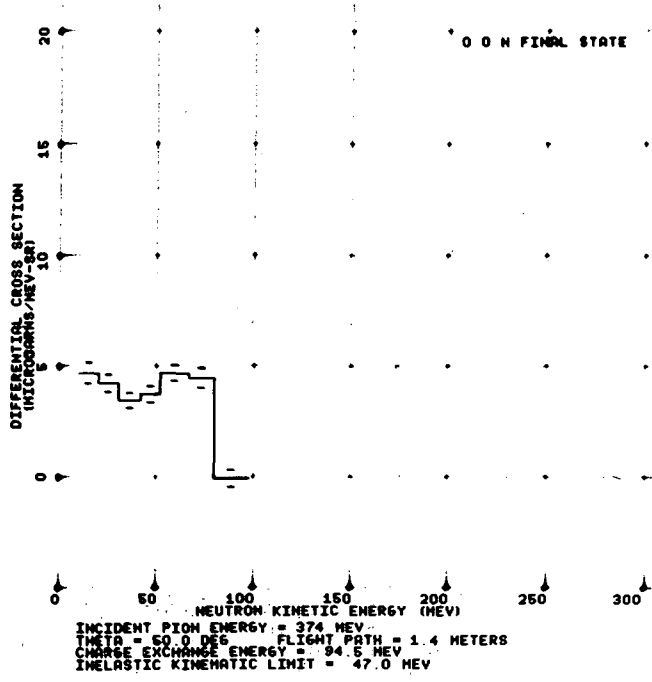CHARGE EXCHANGE ENERGY = 94.6 MEV
INELASTIC KINEMATIC LIMIT = 40.1 MEV



0 0 N FINAL STATE

DIFFERENTIAL CROSS SECTION
(MICROBARNS/MEV-SR)

NEUTRON KINETIC ENERGY (MEV)

INCIDENT PION ENERGY = 374 MEV
THETA = 50.0 DEG     FLIGHT PATH = 2.0 METERS
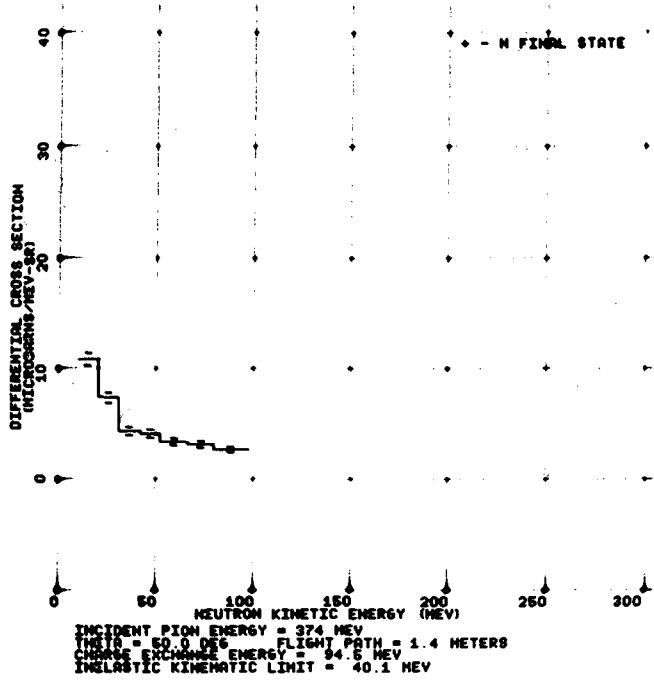CHARGE EXCHANGE ENERGY = 94.6 MEV
INELASTIC KINEMATIC LIMIT = 47.0 MEV

DIFFERENTIAL CROSS SECTION
(MICROGRAMS/MEV-SR)

- N FINAL STATE

NEUTRON KINETIC ENERGY (MEV)

INCIDENT PION ENERGY = 374 MEV
THETA = 55.0 DEG        FLIGHT PATH = 1.4 METERS
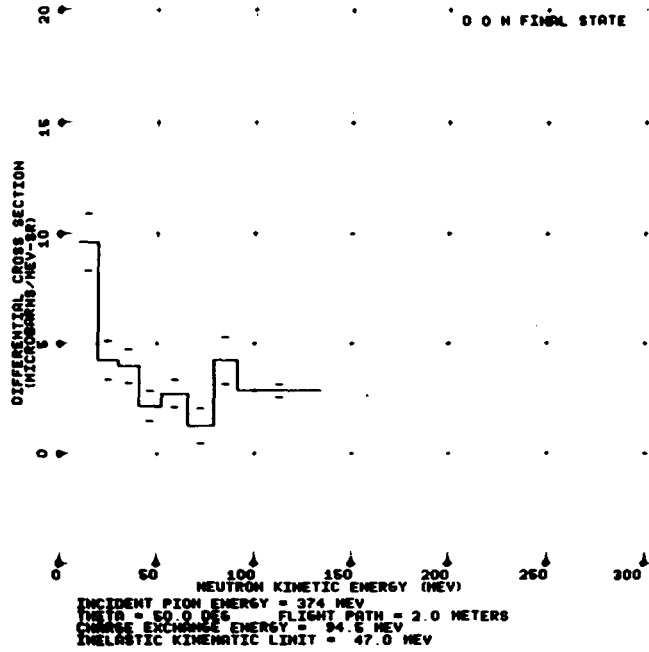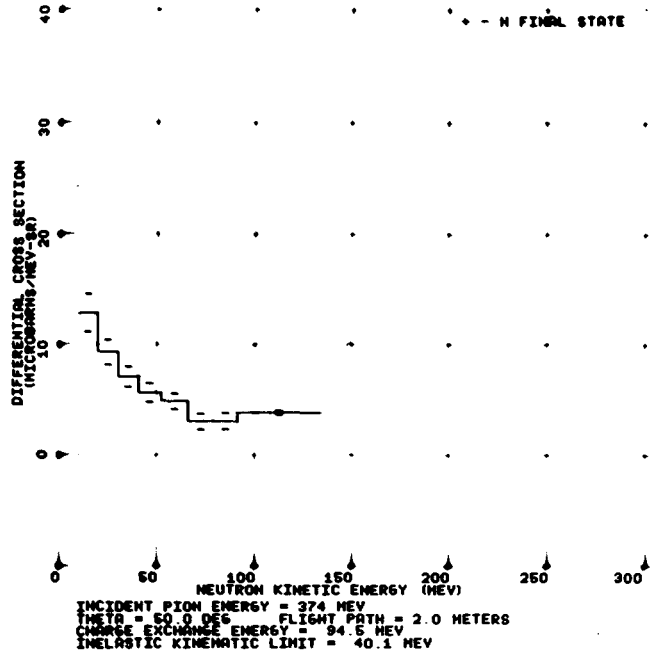CHARGE EXCHANGE ENERGY = 74.6 MEV
INELASTIC KINEMATIC LIMIT =    0.0 MEV



DIFFERENTIAL CROSS SECTION
(MICROGRAMS/MEV-SR)

0 0 N FINAL STATE

NEUTRON KINETIC ENERGY (MEV)

INCIDENT PION ENERGY = 374 MEV
THETA = 55.0 DEG        FLIGHT PATH = 1.4 METERS
CHARGE EXCHANGE ENERGY = 74.6 MEV
INELASTIC KINEMATIC LIMIT =    0.0 MEV

INCIDENT PION ENERGY = 374 MEV
THETA = 55.0 DEG      FLIGHT PATH = 2.0 METERS
CHARGE EXCHANGE ENERGY = 74.6 MEV
INELASTIC KINEMATIC LIMIT = 0.0 MEV



INCIDENT PION ENERGY = 374 MEV
THETA = 55.0 DEG      FLIGHT PATH = 2.0 METERS
CHARGE EXCHANGE ENERGY = 74.6 MEV
INELASTIC KINEMATIC LIMIT = 0.0 MEV

DIFFERENTIAL CROSS SECTION (MICROBARNS/MEV-SR)

+ - N FINAL STATE

NEUTRON KINETIC ENERGY (MEV)

INCIDENT PION ENERGY = 374 MEV
THETA = 60.0 DEG      FLIGHT PATH = 1.4 METERS
CHARGE EXCHANGE ENERGY =  56.0 MEV
INELASTIC KINEMATIC LIMIT =   0.0 MEV



DIFFERENTIAL CROSS SECTION (MICROBARNS/MEV-SR)
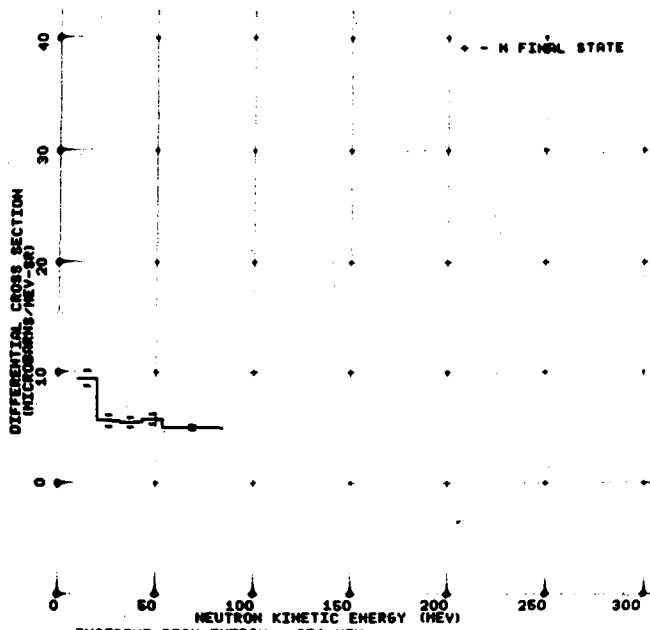
O O N FINAL STATE

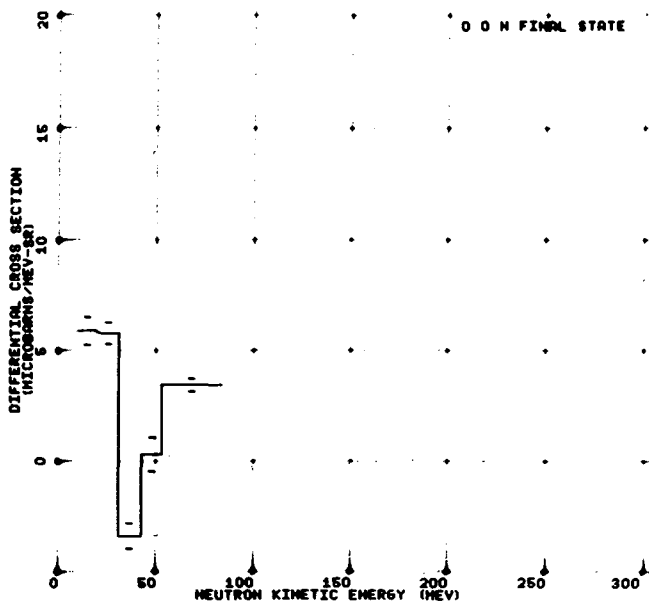NEUTRON KINETIC ENERGY (MEV)

INCIDENT PION ENERGY = 374 MEV
THETA = 60.0 DEG      FLIGHT PATH = 1.4 METERS
CHARGE EXCHANGE ENERGY =  56.0 MEV
INELASTIC KINEMATIC LIMIT =   0.0 MEV

N FINAL STATE

DIFFERENTIAL CROSS SECTION
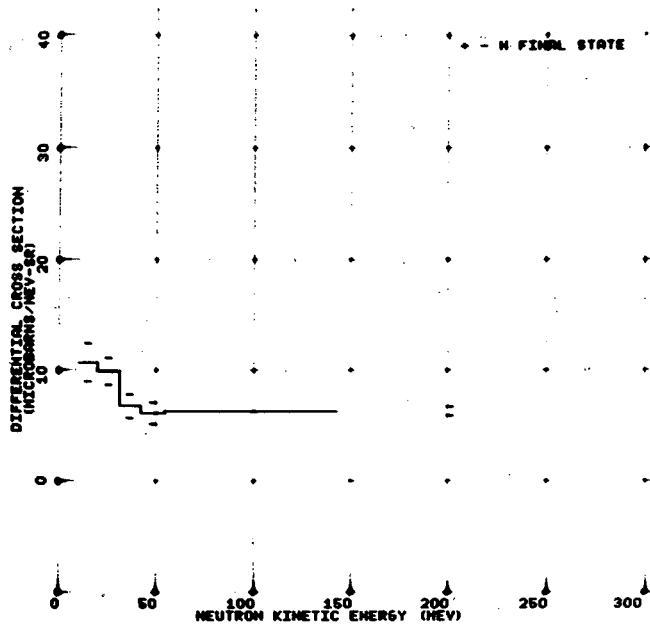(MICROBARNS/MEV-SR)

NEUTRON KINETIC ENERGY (MEV)
INCIDENT PION ENERGY = 374 MEV
THETA = 60.0 DEG      FLIGHT PATH = 2.0 METERS
CHARGE EXCHANGE ENERGY =  56.0 MEV
INELASTIC KINEMATIC LIMIT =   0.0 MEV



O O N FINAL STATE

DIFFERENTIAL CROSS SECTION
(MICROBARNS/MEV-SR)

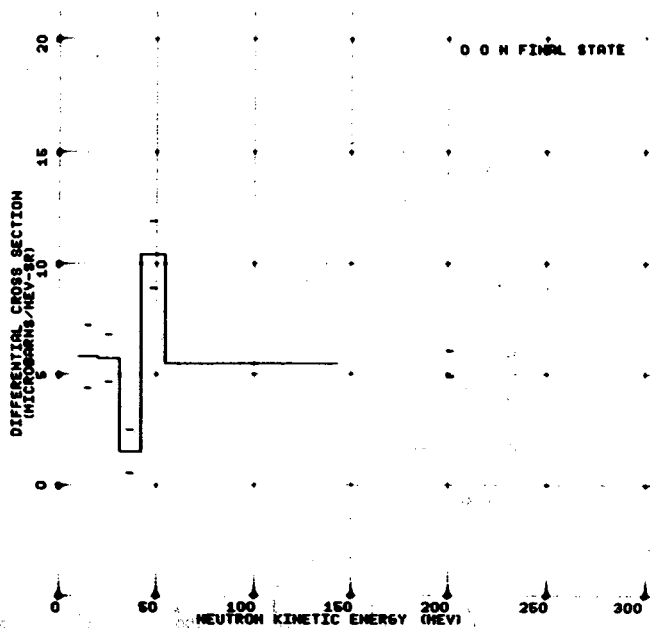NEUTRON KINETIC ENERGY (MEV)
INCIDENT PION ENERGY = 374 MEV
THETA = 60.0 DEG      FLIGHT PATH = 2.0 METERS
CHARGE EXCHANGE ENERGY =  56.0 MEV
INELASTIC KINEMATIC LIMIT =   0.0 MEV

INCIDENT PION ENERGY = 374 MEV
THETA = 65.0 DEG      FLIGHT PATH = 2.0 METERS
CHARGE EXCHANGE ENERGY = 39.7 MEV
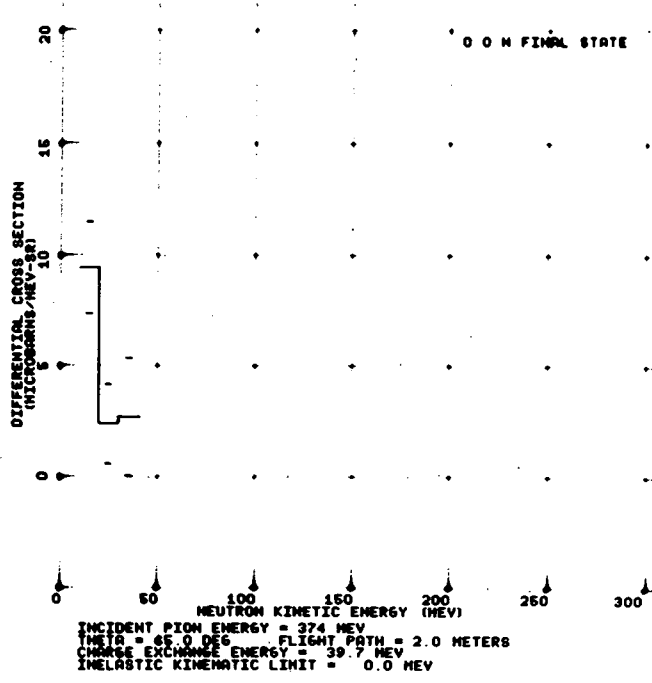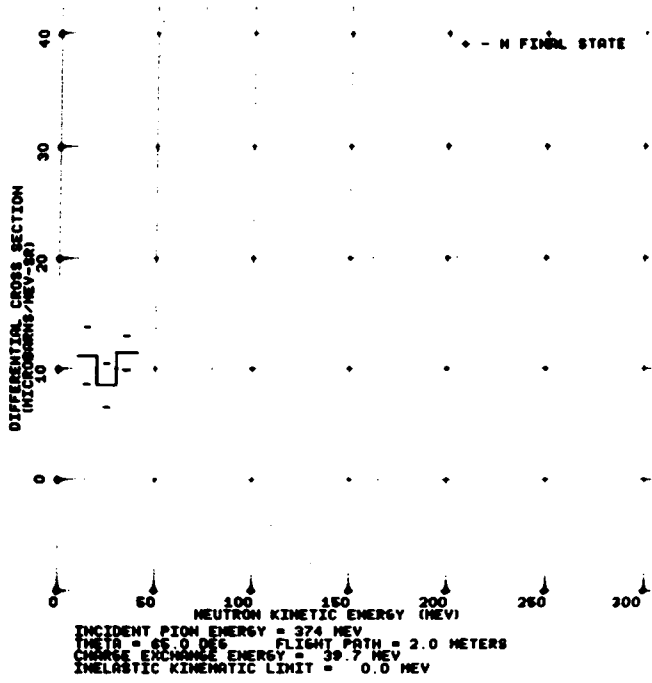INELASTIC KINEMATIC LIMIT =   0.0 MEV



INCIDENT PION ENERGY = 374 MEV
THETA = 65.0 DEG      FLIGHT PATH = 2.0 METERS
CHARGE EXCHANGE ENERGY = 39.7 MEV
INELASTIC KINEMATIC LIMIT =   0.0 MEV

INCIDENT PION ENERGY = 417 MEV
THETA = 10.0 DEG       FLIGHT PATH = 1.4 METERS
CHARGE EXCHANGE ENERGY = 270.8 MEV
INELASTIC KINEMATIC LIMIT = 223.0 MEV



INCIDENT PION ENERGY = 417 MEV
THETA = 10.0 DEG       FLIGHT PATH = 1.4 METERS
CHARGE EXCHANGE ENERGY = 270.8 MEV
INELASTIC KINEMATIC LIMIT = 227.2 MEV

DIFFERENTIAL CROSS SECTION (MICROGRAMS/MEV-SR)
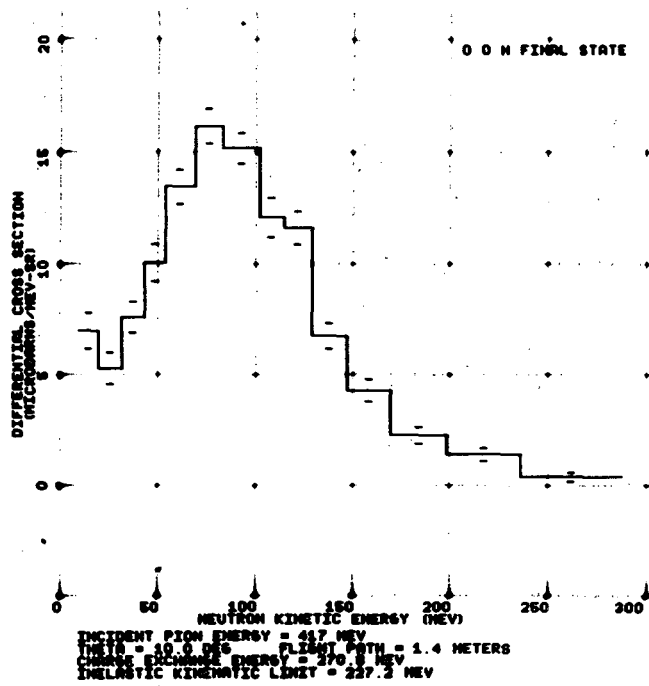
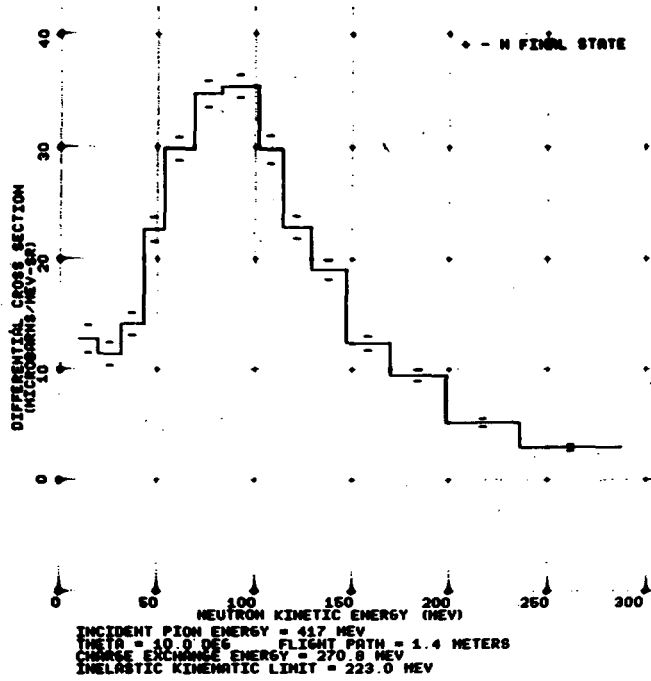NEUTRON KINETIC ENERGY (MEV)

N FINAL STATE

INCIDENT PION ENERGY = 417 MEV
THETA = 10.0 DEG     FLIGHT PATH = 2.0 METERS
CHARGE EXCHANGE ENERGY = 270.8 MEV
INELASTIC KINEMATIC LIMIT = 223.0 MEV



DIFFERENTIAL CROSS SECTION (MICROGRAMS/MEV-SR)
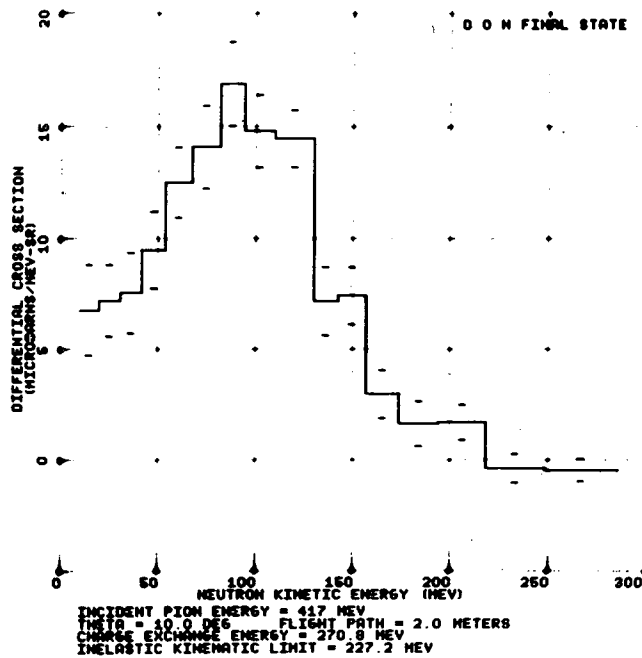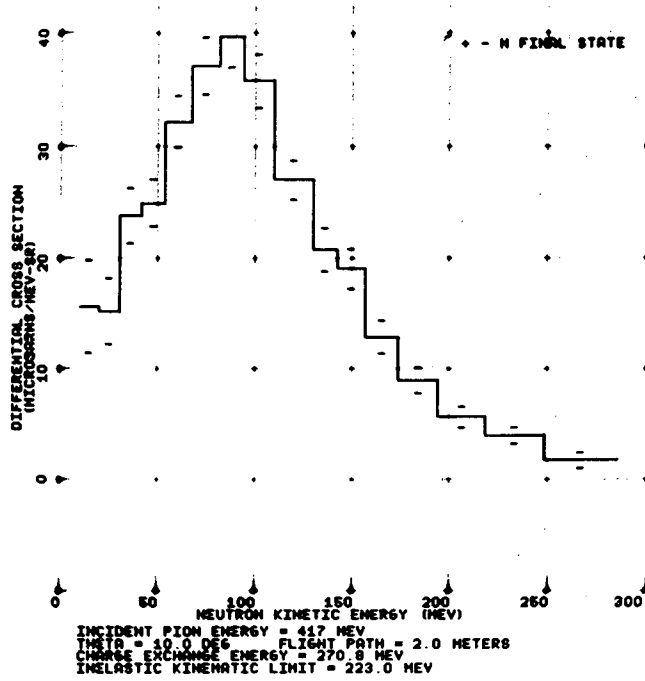
NEUTRON KINETIC ENERGY (MEV)

O O N FINAL STATE

INCIDENT PION ENERGY = 417 MEV
THETA = 10.0 DEG     FLIGHT PATH = 2.0 METERS
CHARGE EXCHANGE ENERGY = 270.8 MEV
INELASTIC KINEMATIC LIMIT = 227.2 MEV

DIFFERENTIAL CROSS SECTION (MICROGRAMS/MEV-SR)

NEUTRON KINETIC ENERGY (MEV)

INCIDENT PION ENERGY = 417 MEV
THETA = 15.0 DEG     FLIGHT PATH = 1.4 METERS
CHARGE EXCHANGE ENERGY = 269.1 MEV
INELASTIC KINEMATIC LIMIT = 211.4 MEV



DIFFERENTIAL CROSS SECTION (MICROGRAMS/MEV-SR)

NEUTRON KINETIC ENERGY (MEV)

INCIDENT PION ENERGY = 417 MEV
THETA = 15.0 DEG     FLIGHT PATH = 1.4 METERS
CHARGE EXCHANGE ENERGY = 269.1 MEV
INELASTIC KINEMATIC LIMIT = 216.7 MEV

N FINAL STATE

DIFFERENTIAL CROSS SECTION
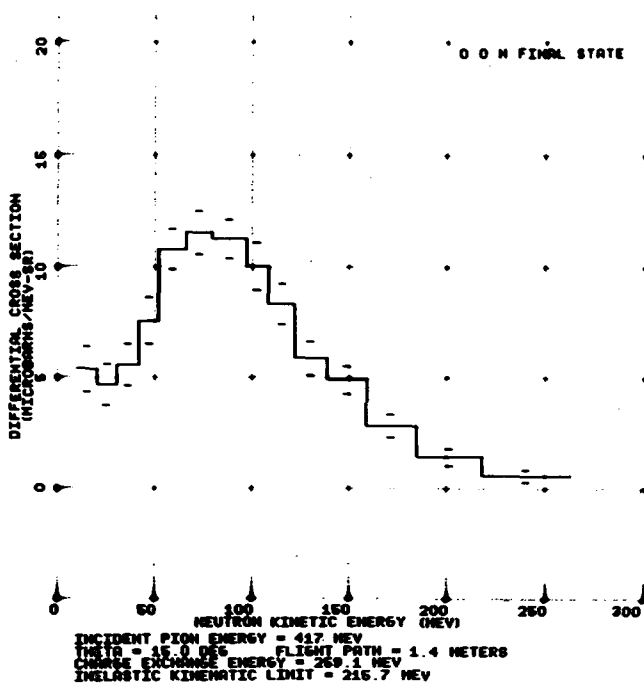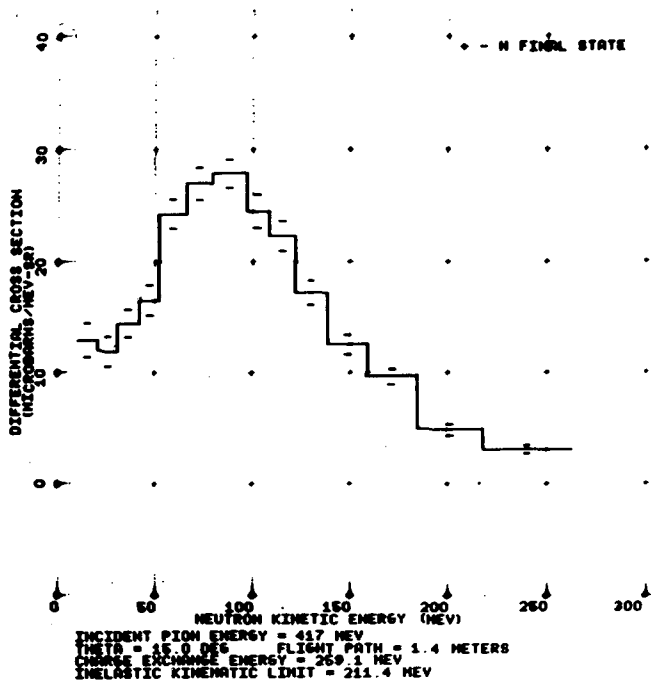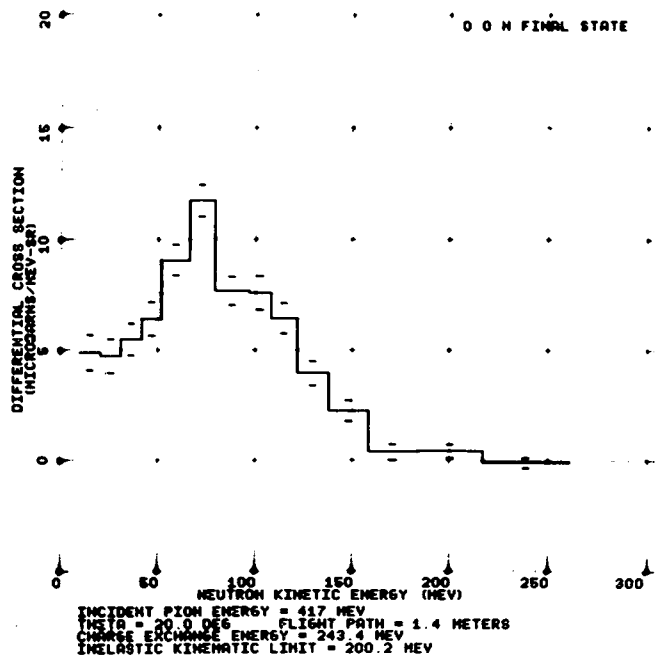(MICROGRAMS/MEV-SR)

NEUTRON KINETIC ENERGY (MEV)

INCIDENT PION ENERGY = 417 MEV
THETA = 20.0 DEG        FLIGHT PATH = 1.4 METERS
CHARGE EXCHANGE ENERGY = 243.4 MEV
INELASTIC KINEMATIC LIMIT = 195.9 MEV



O O N FINAL STATE

DIFFERENTIAL CROSS SECTION
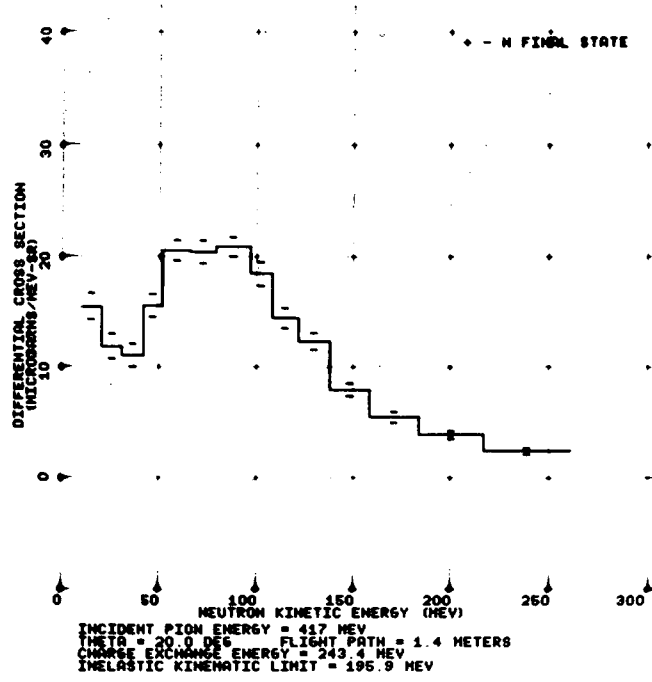(MICROGRAMS/MEV-SR)

NEUTRON KINETIC ENERGY (MEV)

INCIDENT PION ENERGY = 417 MEV
THETA = 20.0 DEG        FLIGHT PATH = 1.4 METERS
CHARGE EXCHANGE ENERGY = 243.4 MEV
INELASTIC KINEMATIC LIMIT = 200.2 MEV

DIFFERENTIAL CROSS SECTION
(MICROGRAMS/MEV-SR)

- N FINAL STATE

NEUTRON KINETIC ENERGY (MEV)

INCIDENT PION ENERGY = 417 MEV
THETA = 20.0 DEG      FLIGHT PATH = 2.0 METERS
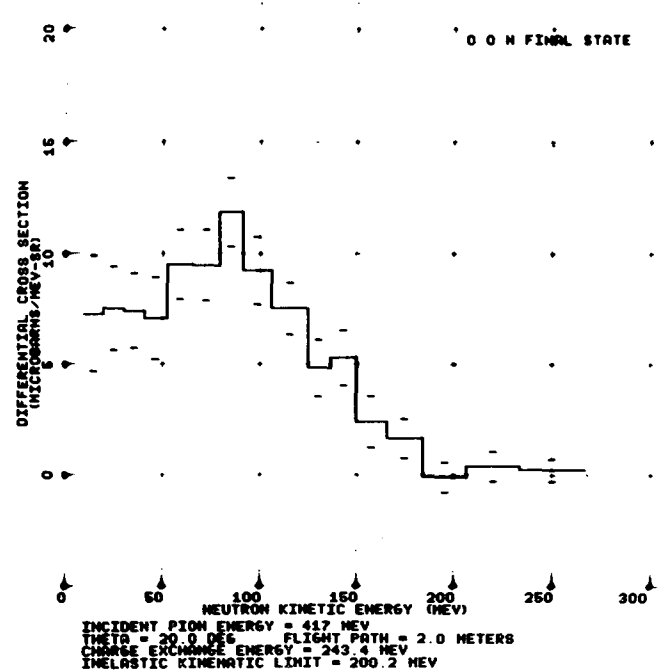CHARGE EXCHANGE ENERGY = 243.4 MEV
INELASTIC KINEMATIC LIMIT = 196.9 MEV



DIFFERENTIAL CROSS SECTION
(MICROGRAMS/MEV-SR)

O O N FINAL STATE

NEUTRON KINETIC ENERGY (MEV)

INCIDENT PION ENERGY = 417 MEV
THETA = 20.0 DEG      FLIGHT PATH = 2.0 METERS
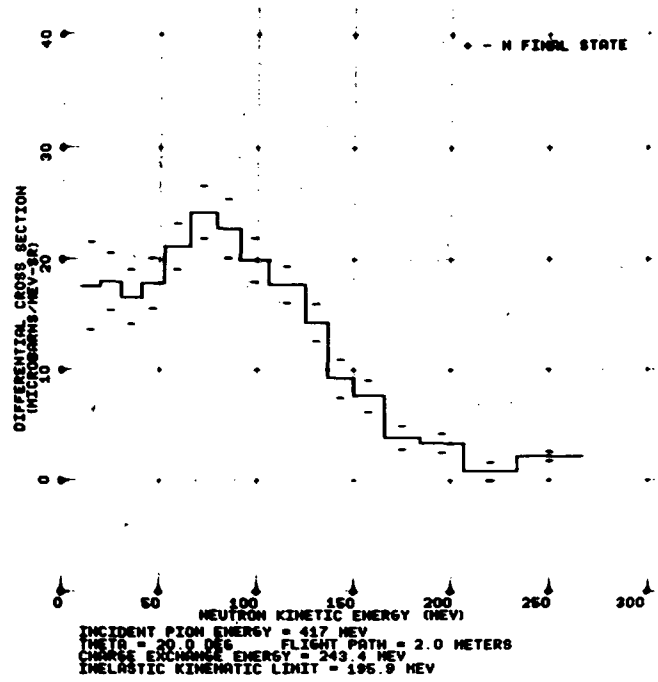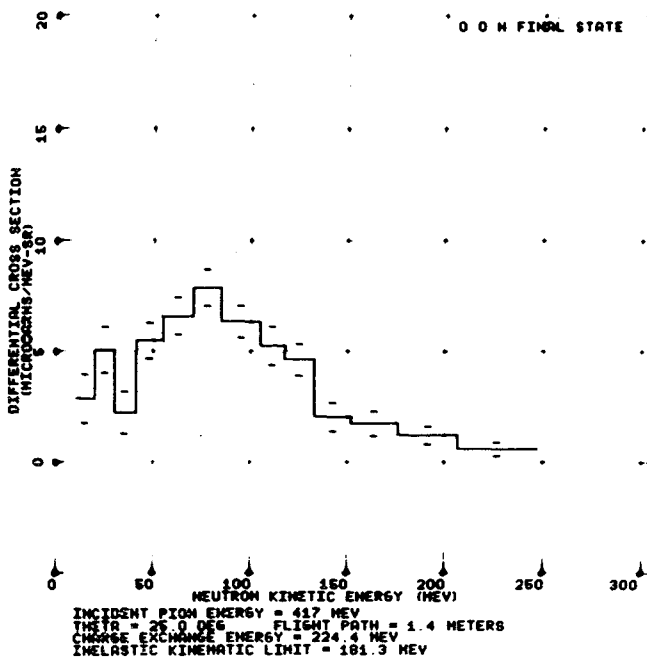CHARGE EXCHANGE ENERGY = 243.4 MEV
INELASTIC KINEMATIC LIMIT = 200.2 MEV

DIFFERENTIAL CROSS SECTION
(MICROGRAMS/MEV-SR)

NEUTRON KINETIC ENERGY (MEV)

N FINAL STATE

INCIDENT PION ENERGY = 417 MEV
THETA = 25.0 DEG     FLIGHT PATH = 1.4 METERS
CHARGE EXCHANGE ENERGY = 224.4 MEV
INELASTIC KINEMATIC LIMIT = 177.1 MEV
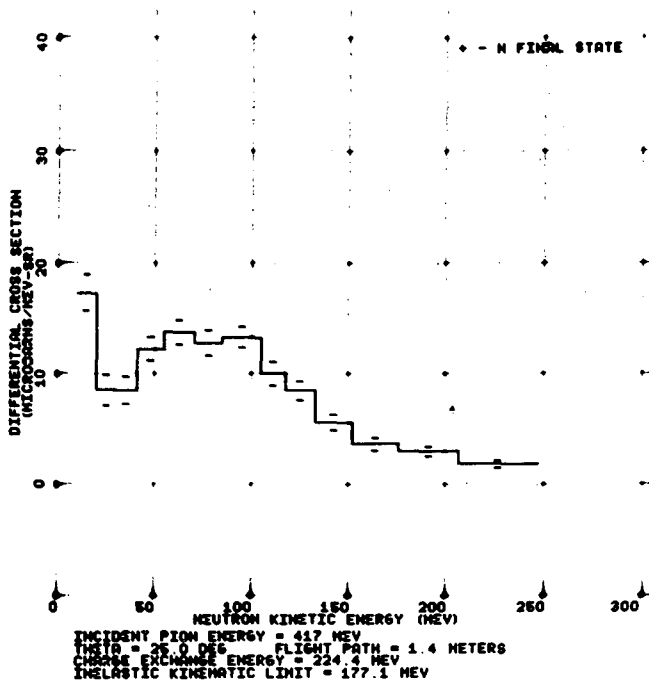


DIFFERENTIAL CROSS SECTION
(MICROGRAMS/MEV-SR)

NEUTRON KINETIC ENERGY (MEV)

O O N FINAL STATE

INCIDENT PION ENERGY = 417 MEV
THETA = 25.0 DEG     FLIGHT PATH = 1.4 METERS
CHARGE EXCHANGE ENERGY = 224.4 MEV
INELASTIC KINEMATIC LIMIT = 181.3 MEV

N FINAL STATE

NEUTRON KINETIC ENERGY (MEV)
INCIDENT PION ENERGY = 417 MEV
THETA = 30.0 DEG    FLIGHT PATH = 1.4 METERS
CHARGE EXCHANGE ENERGY = 202.8 MEV
INELASTIC KINEMATIC LIMIT = 166.6 MEV



0 0 N FINAL STATE

NEUTRON KINETIC ENERGY (MEV)
INCIDENT PION ENERGY = 417 MEV
THETA = 30.0 DEG    FLIGHT PATH = 1.4 METERS
CHARGE EXCHANGE ENERGY = 202.8 MEV
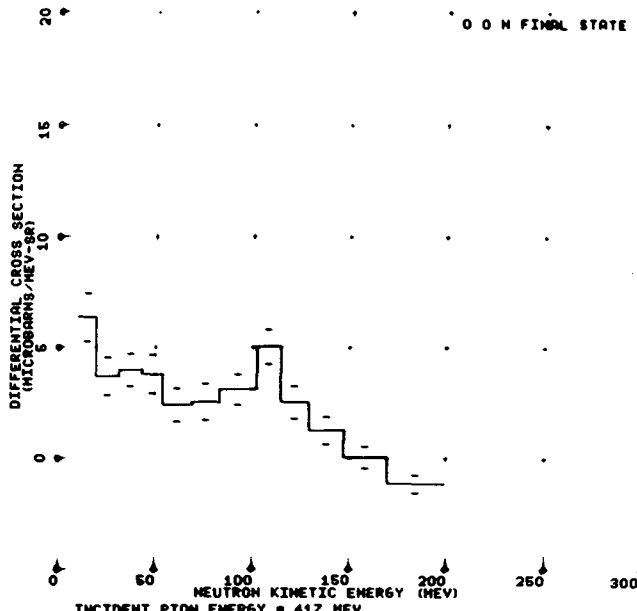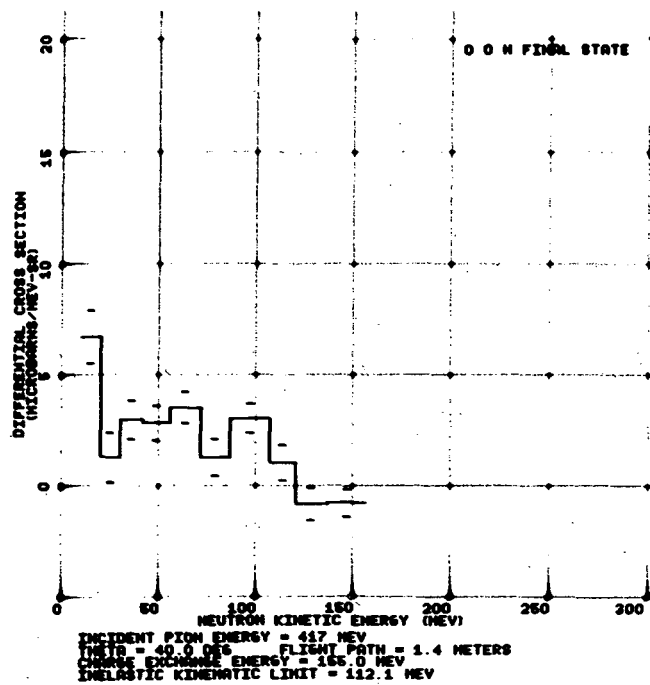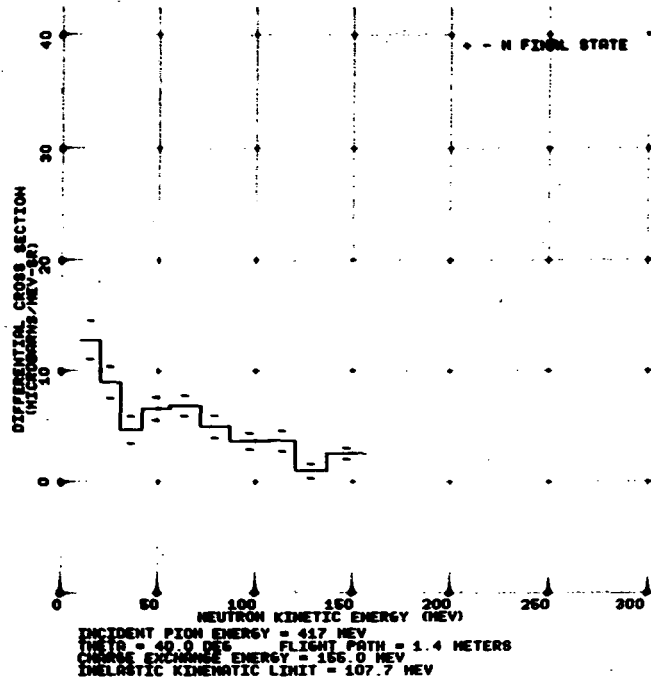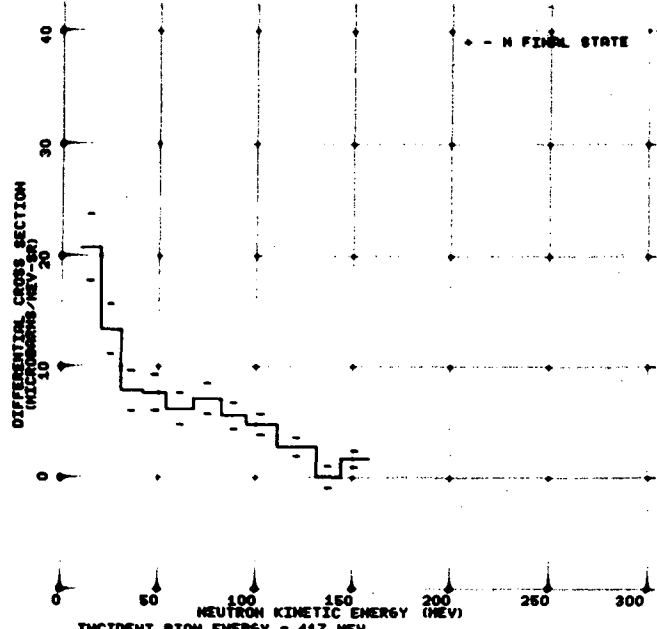INELASTIC KINEMATIC LIMIT = 159.9 MEV

INCIDENT PION ENERGY = 417 MEV
THETA = 35.0 DEG     FLIGHT PATH = 1.4 METERS
CHARGE EXCHANGE ENERGY = 179.3 MEV
INELASTIC KINEMATIC LIMIT = 132.2 MEV



INCIDENT PION ENERGY = 417 MEV
THETA = 35.0 DEG     FLIGHT PATH = 1.4 METERS
CHARGE EXCHANGE ENERGY = 179.3 MEV
INELASTIC KINEMATIC LIMIT = 136.6 MEV

-123-



INCIDENT PION ENERGY = 417 MEV
THETA = 40.0 DEG     FLIGHT PATH = 1.4 METERS
CHARGE EXCHANGE ENERGY = 166.0 MEV
INELASTIC KINEMATIC LIMIT = 107.7 MEV



INCIDENT PION ENERGY = 417 MEV
THETA = 40.0 DEG     FLIGHT PATH = 1.4 METERS
CHARGE EXCHANGE ENERGY = 166.0 MEV
INELASTIC KINEMATIC LIMIT = 112.1 MEV

N FINAL STATE

DIFFERENTIAL CROSS SECTION
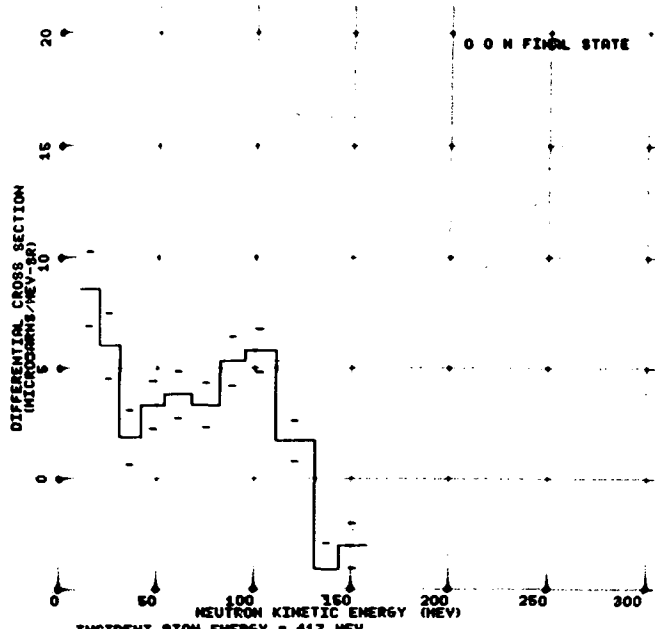(MICROBARNS/MEV-SR)

NEUTRON KINETIC ENERGY (MEV)

INCIDENT PION ENERGY = 417 MEV
THETA = 40.0 DEG       FLIGHT PATH = 2.0 METERS
CHARGE EXCHANGE ENERGY = 166.0 MEV
INELASTIC KINEMATIC LIMIT = 107.7 MEV



O O N FINAL STATE

DIFFERENTIAL CROSS SECTION
(MICROBARNS/MEV-SR)

NEUTRON KINETIC ENERGY (MEV)

INCIDENT PION ENERGY = 417 MEV
THETA = 40.0 DEG       FLIGHT PATH = 2.0 METERS
CHARGE EXCHANGE ENERGY = 166.0 MEV
INELASTIC KINEMATIC LIMIT = 112.1 MEV

INCIDENT PION ENERGY = 417 MEV
THETA = 45.0 DEG        FLIGHT PATH = 1.4 METERS
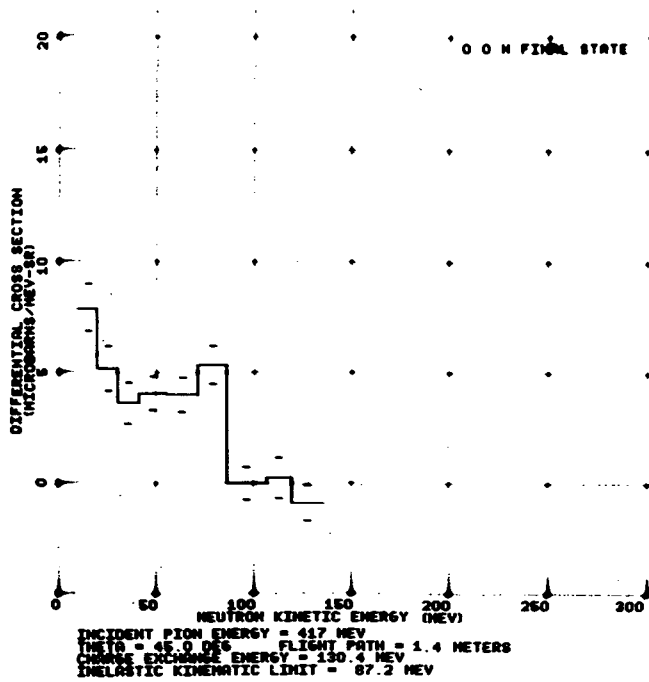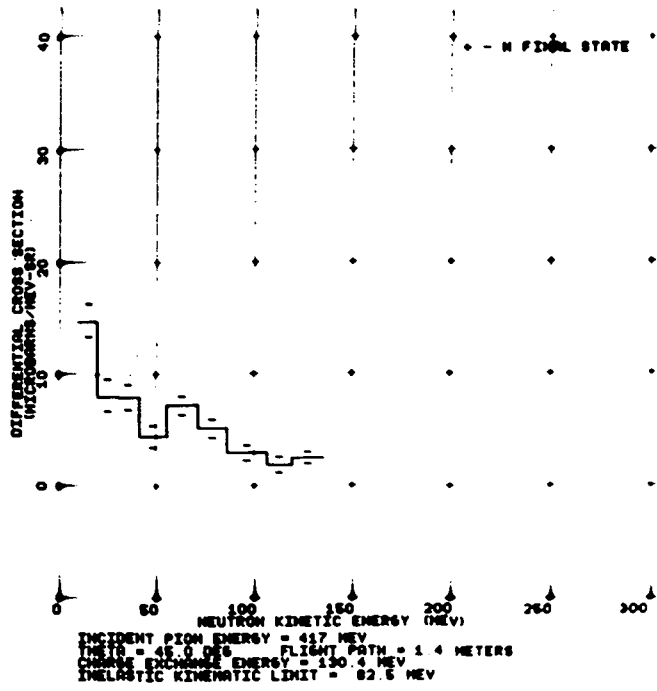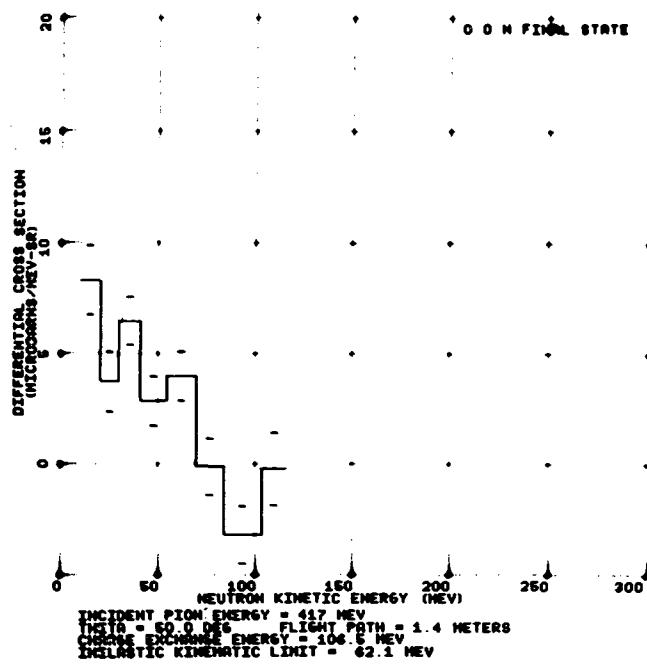CHARGE EXCHANGE ENERGY = 130.4 MEV
INELASTIC KINEMATIC LIMIT = 82.5 MEV



INCIDENT PION ENERGY = 417 MEV
THETA = 45.0 DEG        FLIGHT PATH = 1.4 METERS
CHARGE EXCHANGE ENERGY = 130.4 MEV
INELASTIC KINEMATIC LIMIT = 87.2 MEV

INCIDENT PION ENERGY = 417 MEV
THETA = 50.0 DEG      FLIGHT PATH = 1.4 METERS
CHARGE EXCHANGE ENERGY = 106.6 MEV
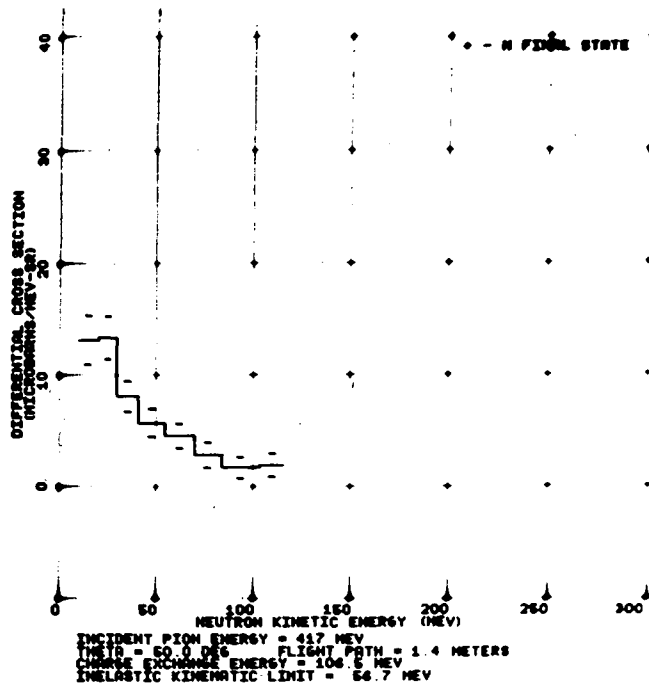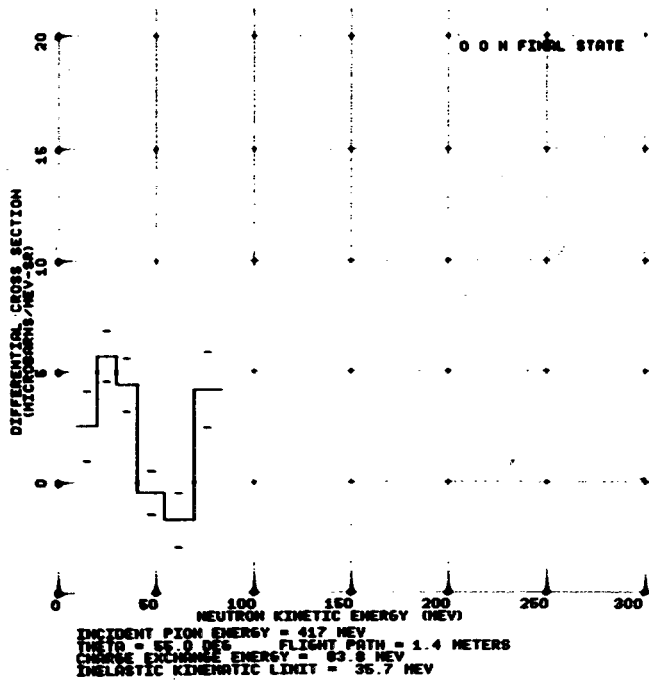INELASTIC KINEMATIC LIMIT = 56.7 MEV



INCIDENT PION ENERGY = 417 MEV
THETA = 50.0 DEG      FLIGHT PATH = 1.4 METERS
CHARGE EXCHANGE ENERGY = 106.6 MEV
INELASTIC KINEMATIC LIMIT = 62.1 MEV

DIFFERENTIAL CROSS SECTION (MICROBARNS/MEV-SR)
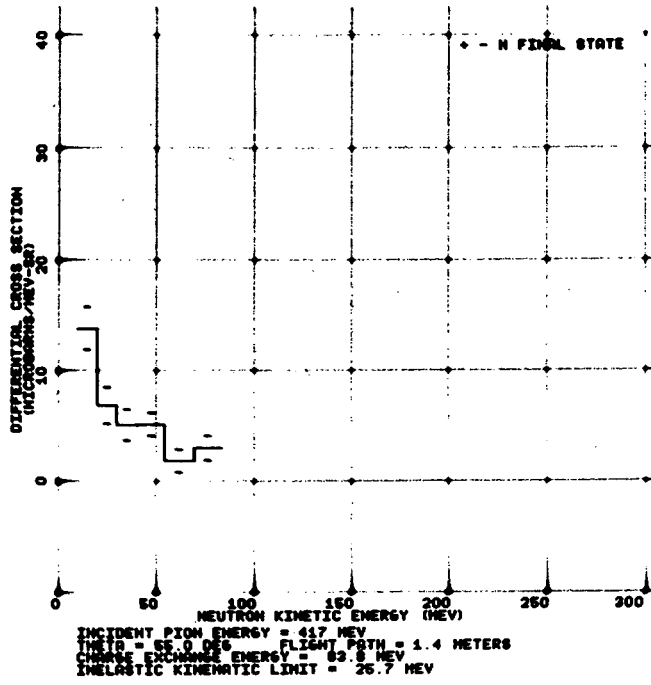
NEUTRON KINETIC ENERGY (MEV)

N FINAL STATE

INCIDENT PION ENERGY = 417 MEV
THETA = 55.0 DEG        FLIGHT PATH = 1.4 METERS
CHARGE EXCHANGE ENERGY = 63.8 MEV
INELASTIC KINEMATIC LIMIT = 26.7 MEV



DIFFERENTIAL CROSS SECTION (MICROBARNS/MEV-SR)
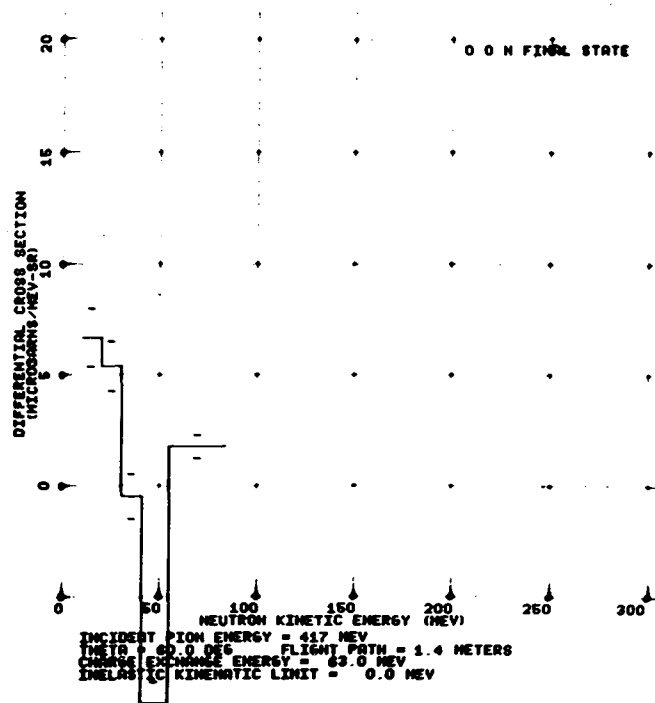
NEUTRON KINETIC ENERGY (MEV)

0 0 N FINAL STATE

INCIDENT PION ENERGY = 417 MEV
THETA = 55.0 DEG        FLIGHT PATH = 1.4 METERS
CHARGE EXCHANGE ENERGY = 63.8 MEV
INELASTIC KINEMATIC LIMIT = 36.7 MEV

DIFFERENTIAL CROSS SECTION (MICROGRAMS/MEV-SR)
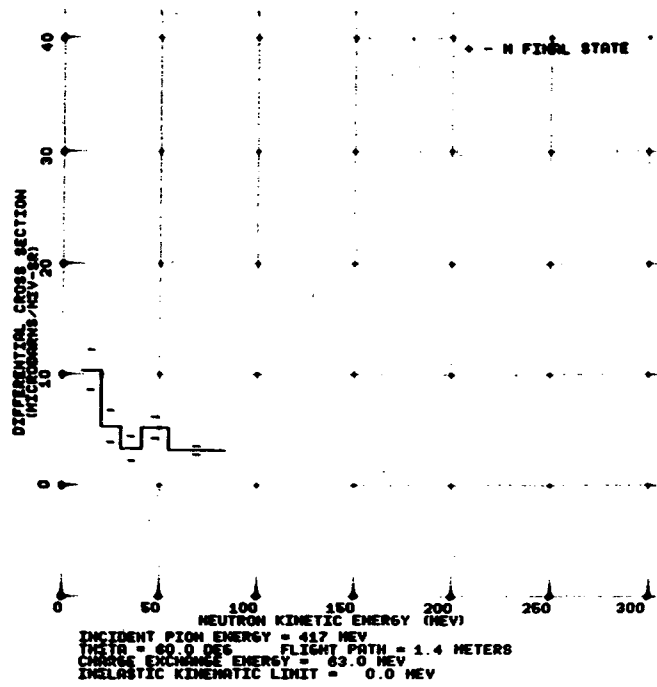
- - N FINAL STATE

NEUTRON KINETIC ENERGY (MEV)
INCIDENT PION ENERGY = 417 MEV
THETA = 60.0 DEG     FLIGHT PATH = 1.4 METERS
CHARGE EXCHANGE ENERGY =  63.0 MEV
INELASTIC KINEMATIC LIMIT =    0.0 MEV



DIFFERENTIAL CROSS SECTION (MICROGRAMS/MEV-SR)
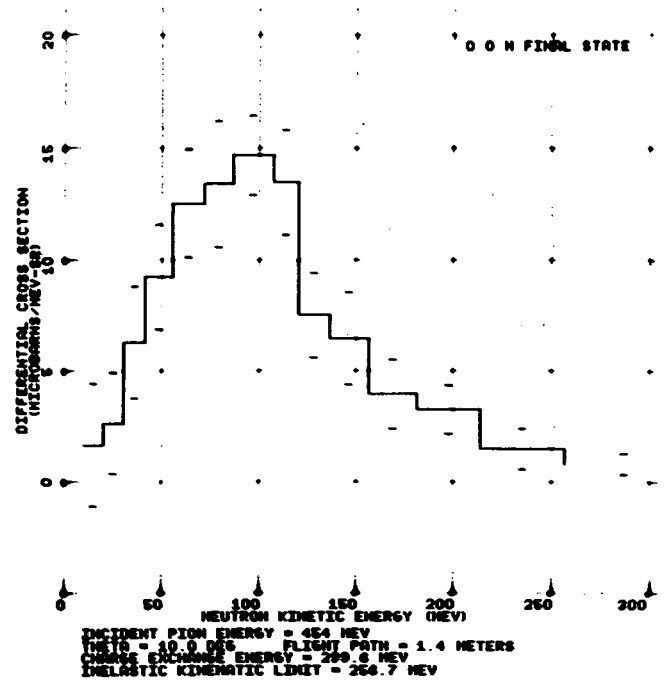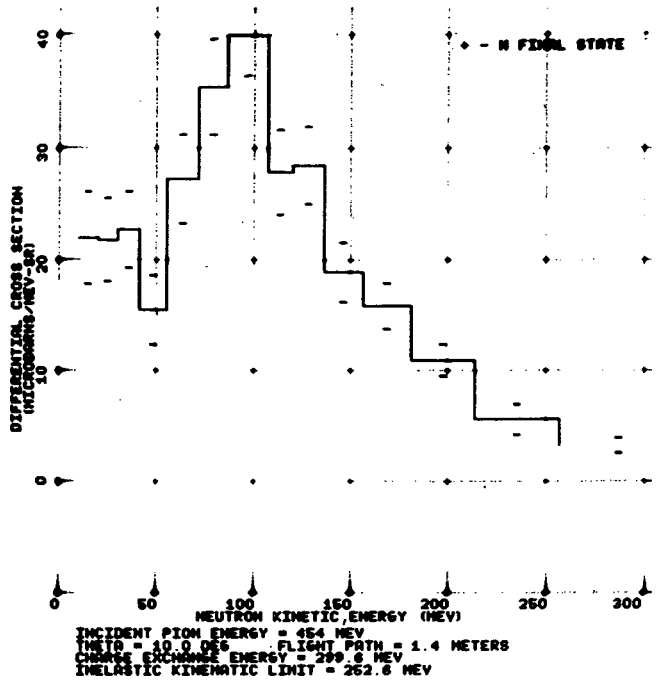
0 0 N FINAL STATE

NEUTRON KINETIC ENERGY (MEV)
INCIDENT PION ENERGY = 417 MEV
THETA = 60.0 DEG     FLIGHT PATH = 1.4 METERS
CHARGE EXCHANGE ENERGY =  63.0 MEV
INELASTIC KINEMATIC LIMIT =    0.0 MEV

DIFFERENTIAL CROSS SECTION
(MICROBARNS/MEV-SR)

NEUTRON KINETIC ENERGY (MEV)

N FINAL STATE

INCIDENT PION ENERGY = 454 MEV
THETA = 10.0 DEG      FLIGHT PATH = 1.4 METERS
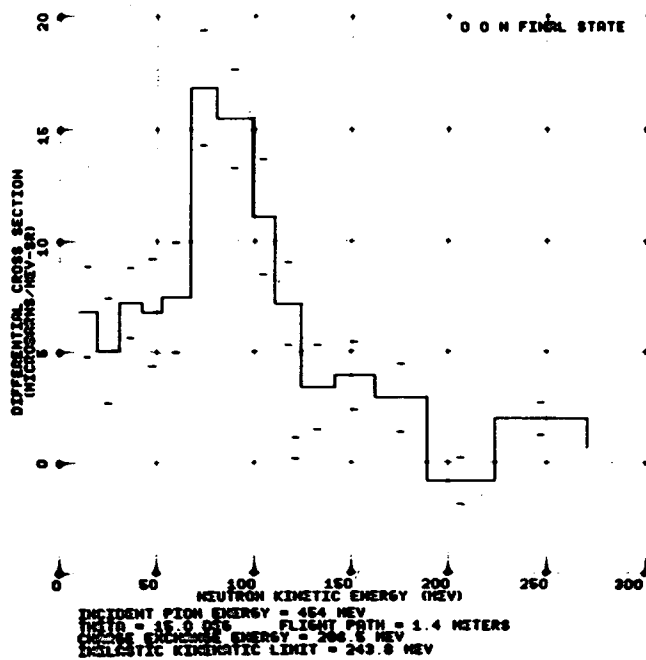CHARGE EXCHANGE ENERGY = 299.6 MEV
INELASTIC KINEMATIC LIMIT = 262.6 MEV



DIFFERENTIAL CROSS SECTION
(MICROBARNS/MEV-SR)

NEUTRON KINETIC ENERGY (MEV)

O O N FINAL STATE

INCIDENT PION ENERGY = 454 MEV
THETA = 10.0 DEG      FLIGHT PATH = 1.4 METERS
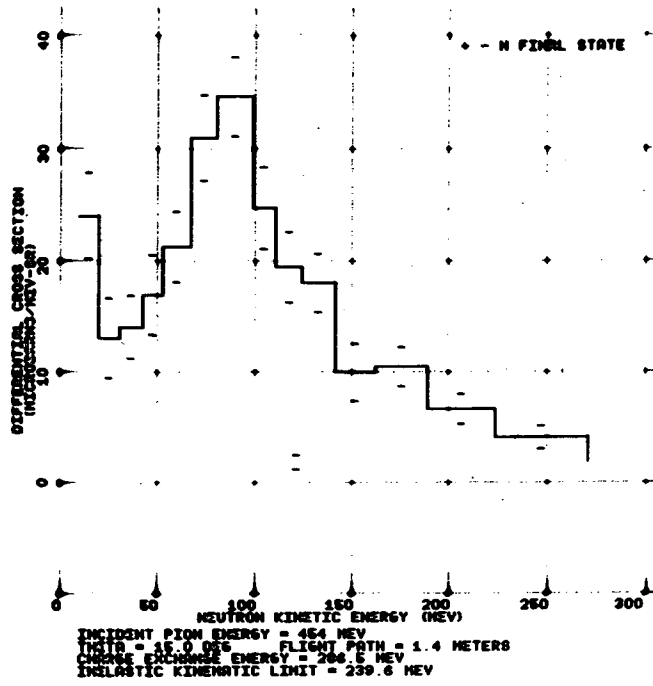CHARGE EXCHANGE ENERGY = 299.6 MEV
INELASTIC KINEMATIC LIMIT = 256.7 MEV

DIFFERENTIAL CROSS SECTION (MICROBARNS/MEV-SR)

N FINAL STATE

NEUTRON KINETIC ENERGY (MEV)

INCIDENT PION ENERGY = 464 MEV
THETA = 15.0 DEG        FLIGHT PATH = 1.4 METERS
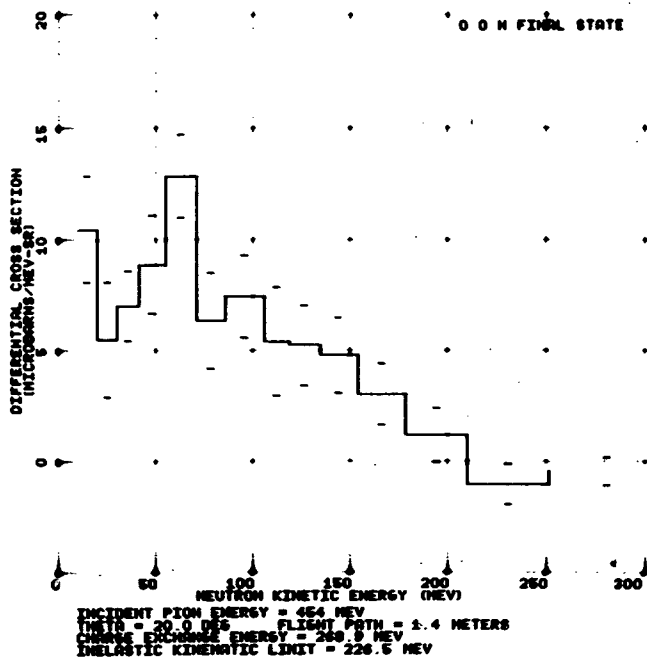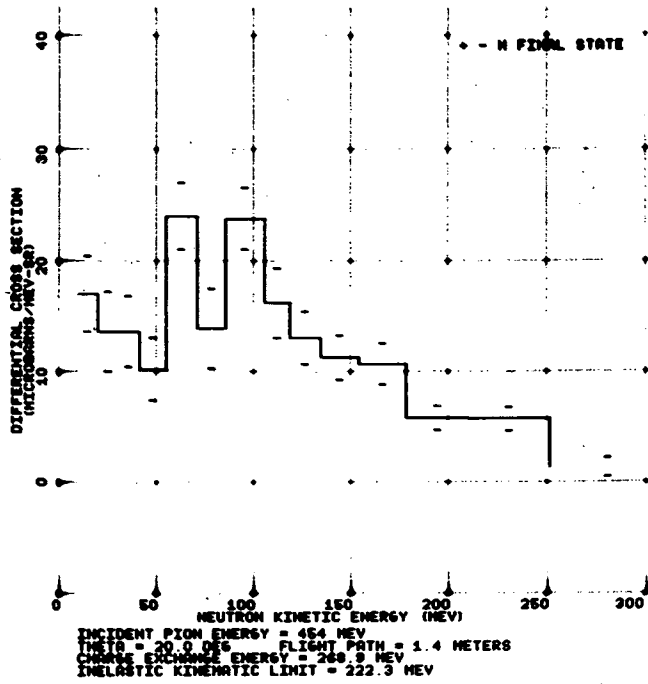CHARGE EXCHANGE ENERGY = 266.5 MEV
INELASTIC KINEMATIC LIMIT = 239.6 MEV



DIFFERENTIAL CROSS SECTION (MICROBARNS/MEV-SR)

0 0 N FINAL STATE

NEUTRON KINETIC ENERGY (MEV)

INCIDENT PION ENERGY = 464 MEV
THETA = 15.0 DEG        FLIGHT PATH = 1.4 METERS
CHARGE EXCHANGE ENERGY = 266.5 MEV
INELASTIC KINEMATIC LIMIT = 243.6 MEV

INCIDENT PION ENERGY = 454 MEV
THETA = 20.0 DEG        FLIGHT PATH = 1.4 METERS
CHARGE EXCHANGE ENERGY = 268.9 MEV
INELASTIC KINEMATIC LIMIT = 222.3 MEV



INCIDENT PION ENERGY = 454 MEV
THETA = 20.0 DEG        FLIGHT PATH = 1.4 METERS
CHARGE EXCHANGE ENERGY = 268.9 MEV
INELASTIC KINEMATIC LIMIT = 226.5 MEV

DIFFERENTIAL CROSS SECTION (MICROBARNS/MEV-SR)

NEUTRON KINETIC ENERGY (MEV)

INCIDENT PION ENERGY = 454 MEV
THETA = 25.0 DEG     FLIGHT PATH = 1.4 METERS
CHARGE EXCHANGE ENERGY = 247.6 MEV
INELASTIC KINEMATIC LIMIT = 201.3 MEV

N FINAL STATE



DIFFERENTIAL CROSS SECTION (MICROBARNS/MEV-SR)

NEUTRON KINETIC ENERGY (MEV)

INCIDENT PION ENERGY = 454 MEV
THETA = 25.0 DEG     FLIGHT PATH = 1.4 METERS
CHARGE EXCHANGE ENERGY = 247.6 MEV
INELASTIC KINEMATIC LIMIT = 206.5 MEV

O O N FINAL STATE

# REFERENCES

1. G. F. Chew and F. E. Low, Phys. Rev. 101, 1570 (1956).

2. L. F. Cook, Jr., and B. W. Lee, Phys. Rev. 127, 297 (1962);
   J. S. Ball, W. R. Frazer, and M. Nauenberg, Phys. Rev. 128, 478 (1962);
   S. Mandelstam, J. E. Paton, R. F. Peierls, and A. Q. Sarker, Ann. Phys. (New York) 18, 198 (1962).

3. Geoffrey F. Chew, S-Matrix Theory of Strong Interactions (W. A. Benjamin, Inc. New York, 1961), p. 8.

4. Walton A. Perkins, III, John C. Caris, Robert W. Kenney, Victor Perez-Mendez, Phys. Rev. 118, 1364 (1960).

5. Emil Kazes, Phys. Rev. 107, 1131 (1957);
   Jerrold Franklin, Phys. Rev. 105, 1101 (1957).

6. Leonard S. Rodberg, Phys. Rev. Letters 3, 58 (1959).

7. V. V. Anisovich, Soviet Physics JETP English Transl. 12, 71 (1961);
   V. V. Anisovich, Soviet Physics JETP Engl. Transl. 12, 946 (1961).

8. Barry C. Barish, Richard J. Kurz, Paul G. McManigal, Victor Perez-Mendez, and Julius Solomon, Phys. Rev. Letters 6, 297 (1961).

9. Charles J. Goebel and Howard J. Schnitzer, Phys. Rev. 123, 1021 (1961).

10. Howard J. Schnitzer, Phys. Rev. 125, 1059 (1962).

11. M. E. Blevins, M. M. Block, and J. Leitner, Phys. Rev. 112, 1287 (1958).

12. Barry C. Barish, A Study of the Reaction $\pi^- + p \to \pi^- + \pi^0 + p$ at 310 and 377 MeV (thesis), Lawrence Radiation Laboratory UCRL-10470, Sept. 1962 (unpublished).

13. Alexander Abashian, Norman E. Booth, and Kenneth M. Crowe, Phys. Rev. Letters 5, 258 (1960);
    Alexander Abashian, Norman E. Booth, and Kenneth M. Crowe, Phys. Rev. Letters 7, 35 (1961).

14. Janos Kirz, Joseph Schwartz, and Robert D. Tripp, Phys. Rev. 126, 763 (1962).

15. Thomas J. Devlin, OPTIK: An IBM 709 Computing Program for the Optics of High-Energy Particle Beams, Lawrence Radiation Laboratory Report UCRL-9727, Sept. 1961 (unpublished).

16. Bruno Rossi, High Energy Particles (Prentice-Hall, Inc. New York, 1952), p. 37.

17. Hugo R. Rugge, Scattering of Negative Pions on Protons at 310 MeV; Differential and Total Cross-Section and Phase-Shift Analysis (thesis), Lawrence Radiation Laboratory Report UCRL-10252, May 1962 (unpublished).

18. Dudley B. Chelton and Douglas B. Mann, Cryogenic Data Book, University of California Radiation Laboratory Report UCRL-3421, May 1956 (unpublished).

19. Lawrence Radiation Laboratory Counting Handbook, Lawrence Radiation Laboratory Report UCRL-3307 Rev. Jan. 1959 (unpublished).

20. Donald L. Wieber, Time-to-Height Converter 4X6422A, Lawrence Radiation Laboratory Engineering Note EE-835, March 1962 (unpublished).

21. Arthur E. Bjerke, Quentin A. Kerns, and Thomas A. Nunamaker, Pulse Shaping and Standardizing of Photomultiplier Signals for Optimum Timing Information Using Tunnel Diodes, Lawrence Radiation Laboratory Report UCRL-9838, Aug. 1961 (unpublished).

22. Harald Cramer, Mathematical Methods of Statistics (Princeton University Press, Princeton, 1946), p. 416.

23. John C. Caris, Robert W. Kenney, Victor Perez-Mendez, and Walton A. Perkins, III, Phys. Rev. 121, 893 (1961).

24. D. W. Josephs, Nuovo Cimento 16, 997 (1960).

25. T. D. Blokhintseva, V. G. Grebinnik, V. A. Zhukov, G. Libman, L. L. Nemenov, G. I. Selivanov, and Y. Jung-Fang, Soviet Physics JETP English Transl. 15, 629 (1962).

26. Donald J. Hughes and Robert B. Schwartz, Neutron Cross Sections, Brookhaven National Laboratory Report BNL-325, July 1958 (unpublished).

27. Yu. A. Batusov, S. Abunyatov, V. M. Sidorov, and V. A. Yarba, in Proceedings of the 1960 Annual International Conference on High-Energy Physics at Rochester (Interscience Publishers, New York, 1960), pp. 74 and 76.

28. René Turley, Contribution a l'Etude des Réactions $\pi^- + p \rightarrow \pi^0 + n$ et $\pi^- + p \rightarrow \pi^0 + \pi^0 + n$ aux Energies des Maxima de la Section Efficace, Totale de l'Interaction $\pi^-$ Nucléon dans l'Etat de Spin Isobarique T = 1/2 (thèse), Commissariat a L'Energie Atomique Rapport, C. E. A. -2136, 1962 (unpublished).

29. Janos Kirz, Joseph Schwartz, and Robert D. Tripp, Bull. Am. Phys. Soc. 7, 282 (1962);
Janos Kirz, Joseph Schwartz, and Robert D. Tripp, A Preliminary Study of the Reaction $\pi^- p \rightarrow \pi^+ \pi^- n$, Lawrence Radiation Laboratory Physics Note UCID-407, June 1962 (unpublished).

30. V. G. Zinov and S. M. Korenchenko, Soviet Physics JETP English Transl. 11, 1010 (1960).

31. G. F. Chew and F. E. Low, Phys. Rev. 113, 1640 (1959).

32. Gyo Takeda (Tohoku University, Sendai, Japan), private communication.

33. Wilmot N. Hess, Rev. Mod. Phys. 30, 368 (1958).

34. H. Grassler and K. Tesch, Nucl. Instr. Methods 10, 353 (1961);
James E. Hardy, Rev. Sci. Instr., 29, 705 (1958);
Lawrence Cranberg and Jules S. Levin, Phys. Rev., 103, 343 (1956);
R. Batchelor, W. B. Gilboy, J. B. Parker, and J. H. Towle, Nucl. Instr. Methods 13, 70 (1961).

35. Malcolm H. MacGregor, William P. Ball, and Rex Booth, Phys. Rev. 111, 1155 (1958);
G. L. Salmon, Nucl. Phys. 21, 15 (1960);
A. Ashmore, R. G. Jarvis, D. S. Mather, and S. K. Sen, Proc. Phys. Soc. (London) 70A, 745 (1957);
A. Ashmore, D. S. Mather, and S. K. Sen, Proc. Phys. Soc. (London) 71, 552 (1957);

P. H. Bowen, J. P. Scanlon, G. H. Stafford, J. J. Thresher, and P. E. Hodgson, Nucl. Phys. 22, 640 (1961);

C. P. van Zyl, R. G. P. Voss, and R. Wilson, Phil. Mag. 1, 1003 (1956);

A. E. Taylor, T. G. Pickavance, J. M. Cassels, and T. C. Randle, Phil. Mag. 42, 328 (1951);

A. E. Taylor and E. Wood, Phil. Mag. 44, 95 (1952);

R. Fox, C. Leith, L. Wouters, and K. R. MacKenzie, Phys. Rev. 80, 23 (1950);

James DeJuren, Phys. Rev. 80, 27 (1950);

J. DeJuren and B. J. Moyer, Phys. Rev. 81, 919 (1950);

George R. Mott, Gordon L. Guernsey, and Bruce K. Nelson, Phys. Rev. 88, 9 (1952);

A. E. Taylor, Phys. Rev. 92, 1071 (1953);

V. Alexander Nedzel, Phys. Rev. 94, 174 (1954).

36. M. P. Nakada, J. D. Anderson, C. C. Gardner, and C. Wong, Phys. Rev. 110, 1439 (1958);

J. D. Anderson, C. C. Gardner, J. W. McClure, M. P. Nakada, and C. Wong, Phys. Rev. 111, 572 (1958).

37. G. M. Frye, Jr., L. Rosen, and L. Stewart, Phys. Rev. 99, 1375 (1955).

38. D. A. Kellogg, Phys. Rev. 90, 224 (1953).

39. Thomas P. Clements and Lester Winsberg, Polynomial Fits of Nucleon-Nucleon Scattering Data, Lawrence Radiation Laboratory Report UCRL-9043, Feb. 1960 (unpublished).

40. T. J. Gooding and H. G. Pugh, Nucl. Instr. Methods 7, 189 (1960).

41. F. Ajzenberg-Selove and T. Lauritsen, Energy Levels of Light Nuclei, Ann. Rev. Nucl. Sci. 10, 416 (1960).

42. Hans A. Bethe and Julius Ashkin, Passage of Radiation Through Matter, in Experimental Nuclear Physics, (John Wiley & Sons, Inc., New York, 1953), pp. 317-325.

43. Clyde E. Wiegand, Tom Elioff, William B. Johnson, Leonard B. Auerbach, Joseph Lach, and Thomas Ypsilantis, Detection Efficiency of Plastic Scintillator for Neutron Energies 4 to 76 MeV, Lawrence Radiation Laboratory Report UCRL-9986, Dec. 1961 (unpublished).

44. G. Gatti, P. Hillman, W. C. Middlekoop, T. Yamagata, and E. Zavattini, Phys. Rev. Letters $\underline{6}$, 706 (1961).

45. Robert Squire, Characteristics of the Production of Neutral Mesons Near Threshold in p-p Collision (thesis), University of California Radiation Laboratory Report UCRL-3137, Sept. 1955 (unpublished).

46. John H. Atkinson, Jr., and Beverly H. Willis, High-Energy Particle Data, University of California Radiation Laboratory Report UCRL-2426 Rev., June 1957 (unpublished).